



Technische Universität München  
TUM School of Natural Sciences

**Development of Pd-labile prodrugs for the  
prevention of biofilms**

**&**

**Investigation of the anti-proliferative target of  
Neocarzilin A**

Dissertation zur Erlangung des akademischen Grades  
eines Doktors der Naturwissenschaften (Dr. rer. nat.)

**Josef Braun**

München 2024





Technische Universität München  
TUM School of Natural Sciences

**Development of Pd-labile prodrugs for the  
prevention of biofilms**

**&**

**Investigation of the anti-proliferative target of  
Neocarzilin A**

Josef Braun

Vollständiger Abdruck der von der TUM School of Natural Sciences der  
Technischen Universität München zur Erlangung des akademischen

Grades eines

**Doktors der Naturwissenschaften (Dr. rer. nat.)**

genehmigten Dissertation.

Vorsitz: Prof. Dr. Martin Zacharias

Prüfende der Dissertation: 1. Prof. Dr. Stephan A. Sieber

2. Prof. Dr. Michael Groll

Die Dissertation wurde am 10.04.2024 bei der Technischen Universität München  
eingereicht und durch die TUM School of Natural Sciences am 24.04.2024  
angenommen.



Für alle Pflegekräfte, Therapeuten und Ärzte,  
die diese Arbeit erst möglich gemacht haben



## **Abstract**

Cancer and bacterial infections are two significant health challenges faced by modern society. This thesis focuses on the development of novel methods to tackle these challenges.

Bacterial biofilms are aggregates of bacteria that attach to surfaces and envelope themselves in an extracellular matrix. In this state, bacteria are more tolerant to environmental stressors like desiccation or antibiotics. When they form on orthopaedic implants, biofilms pose a severe health challenge. Current strategies to prevent the formation of biofilms on implants suffer from various drawbacks. In this work, a novel prodrug strategy has been developed to improve on current methods to prevent biofilm formation. Pd-labile derivatives of the fluoroquinolone antibiotics ciprofloxacin and moxifloxacin were used as prodrugs, and collaboration partners provided two differently sized Pd-nanosheets. Both nanosheets were equally effective in activating a Pd-labile pro-dye and could also activate the prodrugs. When nanosheets were embedded in agarose hydrogels, they could, in combination with a prodrug, prevent the formation of biofilms.

Besides infectious diseases, cancer is one of the leading health challenges faced by modern society. Cancer is defined as the uncontrolled growth and spread of abnormal cells mainly caused by genetic mutations. Drugs against cancer often target the excessive cell growth, but cancer cells can develop resistance. Therefore, novel treatment options are urgently needed. Neocarzilin A is a natural product with strong anti-migratory and anti-proliferative activity. The synaptic vesicle membrane protein VAT-1 was previously identified as the target protein responsible for the anti-migratory effect of neocarzilin A. This work used a new probe to identify the target responsible for the anti-proliferative effect. Activity-based protein profiling revealed bone marrow stromal antigen (BST-2) as a potential target. A knockout of BST-2 proved that BST-2 is responsible for the anti-proliferative activity. Furthermore, neocarzilin led to a decrease in cellular BST-2 levels by lysosomal degradation.

Overall, in this thesis, a new strategy to prevent bacterial infections on implants was developed. Identifying the target of neocarzilin showed that EGFR-dependent proliferation of cancer cells could be downregulated by small molecules targeting BST-2.

## Zusammenfassung

Krebs und bakterielle Infektionen sind zwei der größten Herausforderungen der modernen Gesellschaft. Diese Arbeit hat sich auf die Entwicklung neuer Ansätze zur Bewältigung dieser Herausforderungen fokussiert.

Bakterielle Biofilme sind Zusammenschlüsse von Bakterien, die sich an Oberflächen anhaften und sich in einer Matrix einschließen. In Biofilmen sind Bakterien toleranter gegenüber Umweltsteinflüssen wie Austrocknung oder Antibiotika im Vergleich zu planktonisch lebenden Bakterien. Wenn sich bakterielle Biofilme auf orthopädischen Implantaten bilden, stellen diese wegen ihrer erhöhten Toleranz gegen Antibiotika, eine besondere Herausforderung dar. Aktuelle Strategien zur Prävention von Biofilmen haben verschiedene Nachteile. Aus diesem Grund wurde in dieser Arbeit eine neuartige Prodrug-Strategie auf der Basis von Pd-labilen Prodrugs zur Prävention von Biofilmen entwickelt. Pd-labile Derivate der Fluorchinolon-Antibiotika Ciprofloxacin und Moxifloxacin wurden als Prodrugs verwendet. Zwei unterschiedlich große Pd-Nanopartikel wurden von Kooperationspartnern zur Verfügung gestellt. Beide Nanopartikel waren gleichermaßen aktiv bei der Aktivierung eines Pd-labilen Farbstoffderivates und konnten beide die Pd-labilen Derivate der Antibiotika aktivieren. In ein Agarose-Hydrogel eingebettete Nanopartikel konnten in Kombination mit dem Prodrug die Bildung von Biofilmen verhindern.

Neben Infektionskrankheiten ist Krebs eine der größten gesundheitlichen Herausforderungen der modernen Gesellschaft. Krebs wird durch das unkontrollierte Wachstum und die Ausbreitung abnormer Zellen definiert. Die Krankheit wird hauptsächlich durch genetische Mutationen verursacht. Medikamente gegen Krebs sind oft gegen das übermäßige Wachstum von Krebszellen gerichtet. Krebszellen können jedoch Resistenzen gegen diese Medikamente entwickeln. Aus diesem Grund sind dringend neue Behandlungsoptionen erforderlich. Neocarzin A ist ein Naturstoff mit starker anti-migratorischer und anti-proliferativer Aktivität. Das synaptische Vesikelmembranprotein VAT-1 wurde zuvor als das Zielprotein identifiziert, das für den anti-migratorischen Effekt von Neocarzin A verantwortlich ist. In dieser Arbeit wurde eine neue Sonde verwendet, um das Zielprotein für den anti-proliferativen Effekt zu identifizieren. Chemische Proteomik mit der neuen Sonde identifizierte das Protein BST-2 als potenzielles Zielprotein. Wurde BST-2 genetisch aus den Zellen entfernt, waren diese weniger sensitiv gegenüber Neocarzin. Darüber hinaus führte Neocarzin zu einer Reduktion des zellulären BST-2-Spiegels durch lysosomalen Abbau.

Insgesamt wurde eine neue Strategie zur Verhinderung bakterieller Infektionen auf Implantaten entwickelt, und es wurde gezeigt, dass die EGFR-abhängige Proliferation von

Krebszellen durch kleine Moleküle, die auf BST-2 abzielen, herunterreguliert werden kann, indem das Zielprotein von Neocarzinolol entschlüsselt wurde.

Parts of this thesis have been published in peer-reviewed journals as listed below:

**A Pd-labile fluoroquinolone prodrug efficiently prevents biofilm formation on coated surfaces**

**Josef Braun**, M. Carmen Ortega-Liebana, Asier Unciti-Broceta, Stephan A. Sieber

*Org. Biomol. Chem.*, **2024**, 22, 1998–2002

<https://doi.org/10.1039/D4OB00014E>

---

**Neocarzinil inhibits cancer cell proliferation via BST-2 degradation resulting in lipid raft trapped EGFR.**

**Josef Braun\***, Yudong Hu\*, Adrian T. Jauch\*, Thomas F. Gronauer, Julia Mergner, Nina C. Bach, Franziska R. Traube, Stefan Zahler and Stephan A. Sieber

just accepted in *JACS Au*, **2024**.

\* These authors contributed equally to this work.

<https://pubs.acs.org/doi/10.1021/jacsau.4c00039>

Parts of this thesis have been presented at conferences:

**EFMC-ISCB 2023**

16<sup>th</sup> – 18<sup>th</sup> November 2023, Basel, Switzerland  
*poster presentation*

---

**Frontiers in Medicinal Chemistry 2023**

3<sup>rd</sup> – 5<sup>th</sup> April 2023, Vienna, Austria  
*poster presentation*

---

**EFMC-ISMC 2022**

4<sup>th</sup> – 8<sup>th</sup> September 2022, Nice, France  
*poster presentation*

## Content

### Part I - Background

<b>1. Introduction</b> .....	16
1.1 Natural products.....	16
1.2 Natural products in drug discovery .....	16
<b>2. Natural products and cancer</b> .....	18
2.1 Cancer .....	18
2.2 Natural products to treat cancer .....	21
<b>3. Natural products and bacterial infections</b> .....	24
3.1 Bacterial infections .....	24
3.2 Natural products as antibiotics .....	26
<b>4. Target identification</b> .....	29
4.1 Affinity-based target identification .....	29
4.1.1 Affinity-based pull-downs.....	29
4.1.2 Affinity-based protein profiling (AfBPP).....	31
4.2 Activity-based protein profiling (ABPP) .....	32
4.3 Tag-free target identification .....	32
4.3.1 Thermal protein profiling (TPP) .....	33
4.3.2 Solvent-induced protein precipitation (SIP) .....	34
4.3.3 Drug affinity responsive target stability (DARTS) .....	35
4.4 Other methods.....	36
4.4.1 Genetic methods.....	36
4.4.2 Computational methods.....	39
<b>5. References</b> .....	41

### Part II - Research

<b>6. A Pd-labile fluoroquinolone prodrug efficiently prevents biofilm formation on coated surfaces</b> .....	49
6.1 Metal-labile prodrugs.....	50
6.2 Aim and significance of the project .....	52
6.3 Results and Discussion .....	52
6.3.1 Design and synthesis of the prodrugs .....	52
6.3.2 Biological characterization of the prodrugs.....	53
6.3.3 Antibacterial activity of the nanosheets.....	54
6.3.4 Cell-free prodrug-into-drug conversion.....	54
6.3.5 Prevention of biofilms.....	55
6.4 Summary and conclusion .....	56

6.5	Supplementary Information .....	57
6.5.1	Supplementary Figures S1-S7.....	57
6.5.2	Supplementary Tables .....	63
6.5.3	Methods.....	64
6.6	References .....	82
<b>7.</b>	<b>Neocarzilin inhibits cancer cell proliferation via BST-2 degradation resulting in lipid raft trapped EGFR.</b> .....	<b>85</b>
7.1	Neocarzilin .....	85
7.2	Aim and significance of the project .....	85
7.3	Results and Discussion .....	85
7.3.1	Probe labeling in cancer cells .....	85
7.3.2	BST-2 mediates the anti-proliferative effects of NCA .....	88
7.3.3	NCA treatment reduces BST-2 levels via lysosomal degradation .....	88
7.4	Summary and Conclusion .....	90
7.5	Supplementary Information .....	91
7.5.1	Supplementary Figures S8-12.....	91
7.5.2	Methods.....	96
7.5.3	Supplementary Tables .....	100
7.6	References .....	104
<b>Part III - Appendix</b>		
<b>8</b>	<b>Abbreviations .....</b>	<b>107</b>



# **Part I**

## Background

# 1. Introduction

## 1.1 Natural products

Natural products are small molecules produced by living organisms such as bacteria, fungi, or plants. They are also known as secondary metabolites, as they are not essential for survival but give the producing organism a fitness advantage over competitors. Natural products have been the foundation for many medicine-, biology-, and chemistry-related discoveries. Their structural complexity makes their total synthesis one of the most dynamic and exciting fields of chemistry. The total synthesis of challenging natural products leads to the discovery of novel methodologies, reagents, and catalysts.<sup>[1]</sup> These, in turn, can be applied to problems in the pharmaceutical, agrochemical, and materials industries. Natural products have been optimized by evolution to serve different biological functions and interact with other biomolecules.<sup>[2]</sup> Therefore, natural products are a rich source of biologically active small molecules. If enough material is available from synthesis or isolation from their natural source, their interaction with biological systems can be studied. This can lead to discoveries in biology, like disease-relevant pathways or even new drugs. For these reasons, natural products are a valuable resource in drug discovery.

## 1.2 Natural products in drug discovery

Humans have used nature-based remedies such as plant extracts for millennia, but the active principles of these remedies were unknown. In 1817, a German pharmacist's apprentice, Friedrich Sertuner, managed to isolate the active principle from crude opium, a substance he would later call morphine (Figure 1A).<sup>[3]</sup> This was the first isolated active principal, but many more followed. Since then, natural products for different therapeutic areas have been isolated. Examples are penicillin, an antibacterial from mold (Figure 1B), paclitaxel, an antitumor agent from yew trees (Figure 1C), and artemisinin, an antimalarial from sweet wormwood (Figure 1D).<sup>[4]</sup> For her work on artemisinin, Prof. Youyou Tu was awarded with the Nobel Prize in Medicine.<sup>[5]</sup> Around one-third of all small molecule drugs approved between Jan. 1981 and Sept. 2019 are natural products or natural product-derived molecules.<sup>[6]</sup> Various factors make natural products so successful. They cover a highly diverse chemical space.<sup>[7]</sup> On average, they contain fewer nitrogen, halogen, and sulphur atoms than synthetic compounds but more oxygen atoms. Furthermore, they have a higher relative fraction of  $sp^3$ -hybridized bridgehead atoms, an average number of rings, and more chiral centers per molecule, making them sterically more complex compared to synthetic compounds.<sup>[8],[9]</sup> Their high fraction of  $sp^3$ -hybridized carbon atoms ( $F_{sp^3}$ ) is further evidence of the steric complexity of natural products.<sup>[10]</sup> A high  $F_{sp^3}$  and an increasing number of chiral centers have been linked to increased success in the clinic.<sup>[11]</sup>

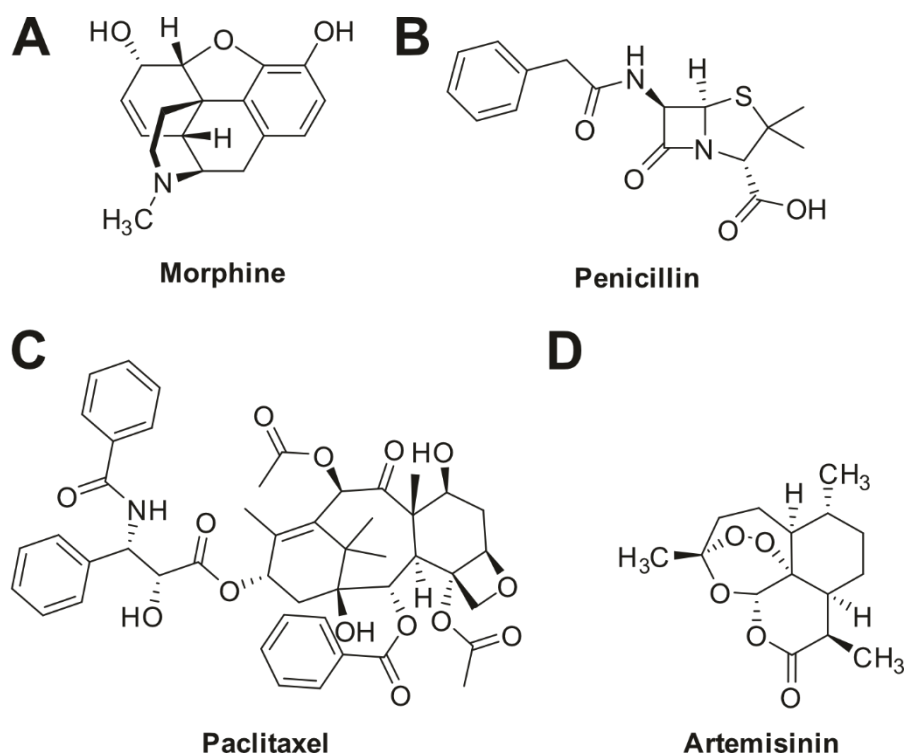


**Figure 1.** Structures of isolated natural products. (A) morphine, (B) penicillin, (C) paclitaxel, (D) artemisinin.

Furthermore, natural products are more hydrophilic than synthetic molecules from a combinatorial library.<sup>[8b]</sup> A lower LogP (higher hydrophilicity) correlates with a lower target promiscuity of a compound.<sup>[12]</sup> The same was shown for an increasing number of chiral centers and an increasing Fsp<sup>3</sup>.<sup>[13]</sup> Target promiscuity of a compound has been linked to toxicity, the primary reason for failure in the clinic.<sup>[13-14]</sup> This might contribute to natural products being so successful as drugs. The number of newly discovered natural products has risen steadily since the 1940s. Despite the increasing number of discovered natural products, the number of structurally unique natural products discovered yearly decreases.<sup>[15]</sup> The decreasing number of novel structures from natural products and their importance for drug discovery has led to research in artificial natural product-like structures to harness the favourable properties of natural products. The concept of pseudo-natural products was wildly successful. Pseudo-natural products are the *de novo* combination of natural product-based fragments in a way that is not found in nature. The new structures retain the chemical and biological properties of natural products but are not accessible by known biosynthetic pathways, giving access to novel natural product-like chemical space.<sup>[16]</sup> Due to their advantageous properties, natural products have been approved in many different therapeutic areas. However, most natural products or natural product-derived molecules have been approved for the treatment of bacterial infections and cancer.<sup>[6]</sup>

## 2. Natural products and cancer

### 2.1 Cancer

Cancer is a collection of diseases characterized by uncontrolled growth and spread of abnormal cells mainly caused by genetic mutations.<sup>[17]</sup> For the year 2020, it was estimated that 19.3 million new cancer cases were diagnosed, and 10.0 million deaths were caused by cancer worldwide. The three most often diagnosed cancers were female breast cancer (11.7 %), lung cancer (11.4 %) and colorectal cancer (10.0 %).<sup>[18]</sup> The incidence of cancer in the United States during the period 2014-2018 was 457.5 per 100 000.<sup>[19]</sup> For 2023, it was expected that 2 million new cancer cases and 609 820 cancer deaths will occur in the United States.<sup>[20]</sup> Cancer results from changes in the genome. These mutations occur naturally in all normal cells during cell division but also can be caused by external factors like toxins or radiation. Each mutation can be classified according to its consequences for cancer development. So-called “Driver” mutations facilitate a growth advantage and occur in the subset of genes called “cancer genes.” Mutations that do not provide their cells with a growth advantage are known as “passenger” mutations and usually make up the majority of mutations a cell acquires. The driver mutations lead to a positive selection, as they give the cancer cells an advantage compared to the normal cells surrounding them.<sup>[17b, 17c]</sup> Driver genes are classified as oncogenes or tumor suppressor genes. Tumor suppressor genes play a crucial role in regular cell growth and differentiation and block cancer growth. Loss or inactivation of tumor suppressor genes leads to cancer. A prime example of a frequently mutated tumor suppressor gene is P53. Mutations in this gene were reported in almost every type of cancer, with rates between 10 % and 100 %.<sup>[21]</sup> On the other hand, pro-oncogenes are regulators of key biological processes like cell differentiation and proliferation. Changes in these genes can lead to the formation of oncogenes that promote cancer development. The formation of oncogenes drives proliferation and other cancer characteristics.<sup>[22]</sup> c-Myc is an example of a pro-oncogene that is estimated to be aberrantly expressed in over 70 % of human cancers and regulates key processes, including proliferation and apoptosis.<sup>[23]</sup> Cancer pathogenesis has a striking resemblance to evolution. Both rely on the continuous acquisition of genetic variation and a natural selection of the resulting mutants.<sup>[17b]</sup> The functional abilities cells need to develop to form malignant tumors have been termed “Hallmarks of Cancer.” Originally, Hanahan and Weinberg proposed six distinct hallmark capabilities (evading apoptosis, self-sufficiency in growth signals, insensitivity to anti-growth signals, tissue invasion and metastasis, limitless replicative potential, and sustained angiogenesis). Over time, they included in total of 14 hallmarks and enabling characteristics (unlocking phenotypic plasticity, nonmutational epigenetic reprogramming, polymorphic microbiomes, senescent cells, sustaining proliferative signalling, evading growth suppressors, resisting cell death, enabling

replicative immortality, inducing/accessing vasculature, activating invasion and metastasis, deregulating cellular metabolism, avoiding immune destruction, genome instability & mutation and tumor-promoting inflammation) (Figure 2).<sup>[24]</sup>

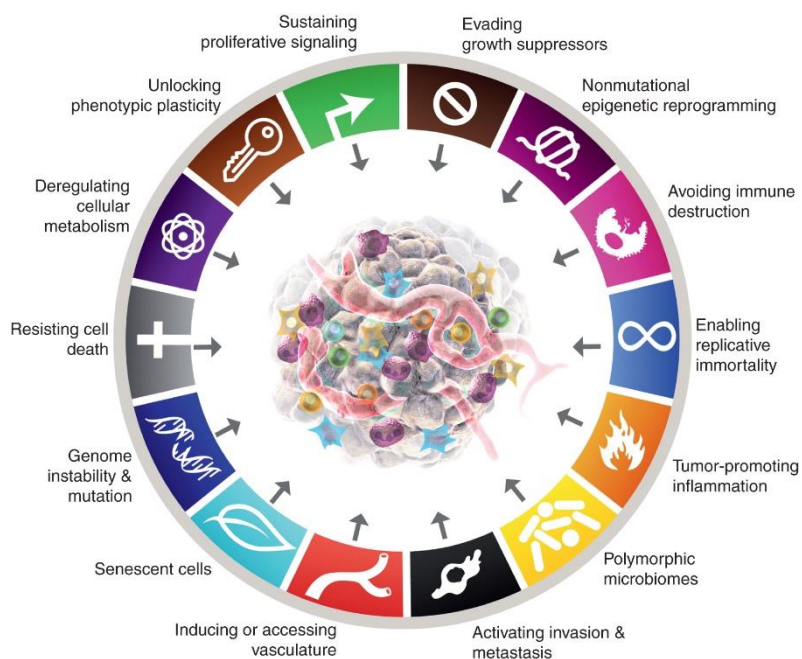


**Figure 2.** Hallmarks of cancer. Used with permission.<sup>[24b, 24c]</sup>

Since the hallmarks are, per definition, characteristic of the formation of malignant tumors, they present opportunities for cancer drug development. Many approved cancer drugs can be attributed to one of the hallmarks. For example, the tyrosine kinase epidermal growth factor receptor (EGFR) is a regulator of cell proliferation. Overexpression of EGFR or mutations increases the kinase activity and enhances cell proliferation, which is a driver of many cancers.<sup>[25]</sup> Due to the importance of EGFR activity in many cancers, several generations of inhibitors for the kinase activity of EGFR have been brought to market, e.g., erlotinib, afatinib, and osimertinib (Figure 3), and they clearly can be attributed to the hallmark of “Sustaining proliferative signaling.”<sup>[24c, 26]</sup>

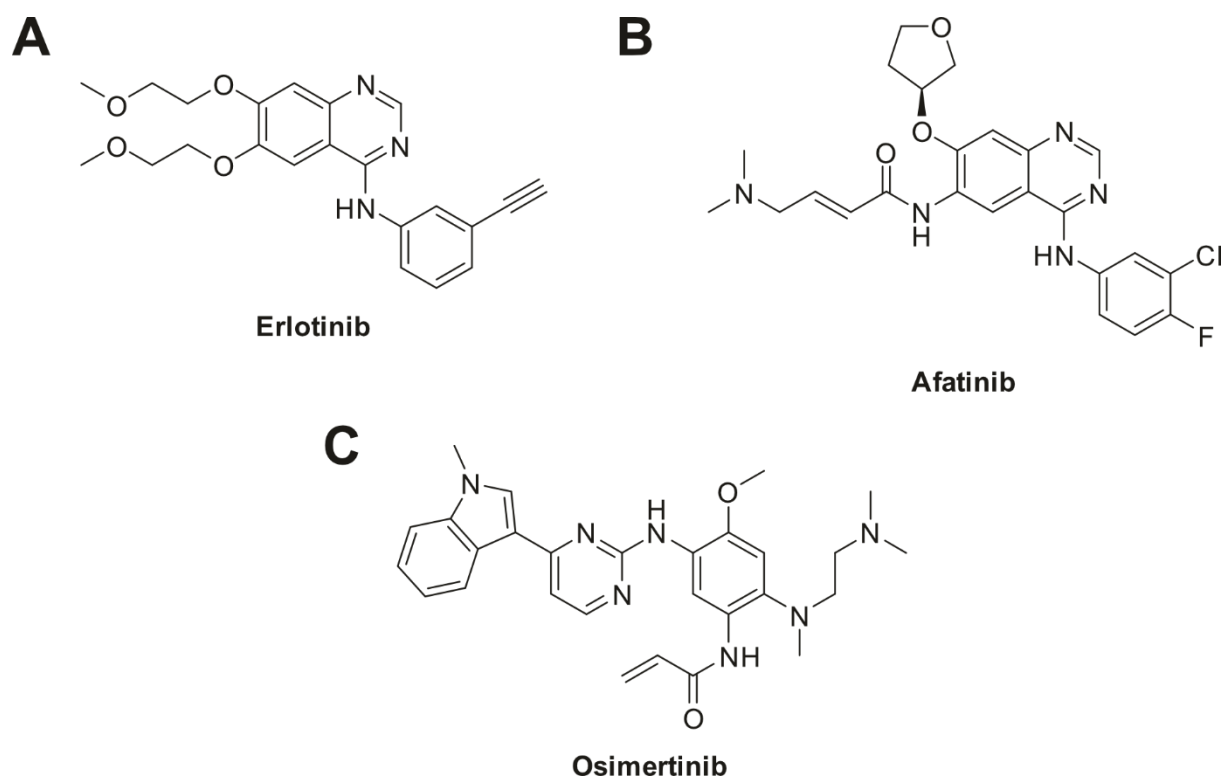


**Figure 3.** FDA-approved EGFR inhibitors. (A) erlotinib, (B) afatinib, (C) osimertinib.

Invasion is the process where cancer cells expand into the surrounding environment. Invasive cell growth is a characteristic that differentiates benign and malignant tumors.<sup>[27]</sup> During metastasis, tumor cells break away from the primary tumor, migrate to a new, distant location, and form a secondary tumor. Metastases are responsible for the majority of deaths associated with cancer.<sup>[28]</sup> It has been found that the overexpression of hepatocyte growth factor (HGF) and its receptor tyrosine kinase c-Met is associated with invasion and metastasis in many cancers.<sup>[29]</sup> Crizotinib (Figure 4), an FDA-approved inhibitor of the kinase activity of c-Met, inhibits cell migration and invasion, another hallmark.<sup>[30]</sup>

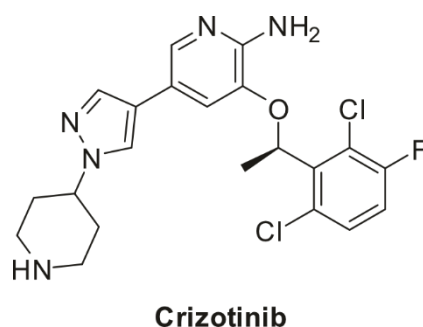


**Figure 4.** Structure of crizotinib.

The development of drugs for the treatment of cancer remains a very active field, steadily improving the lives of cancer patients. The age-adjusted US mortality for all cancer sites decreased from 206 per 100 000 in the period 1995 – 1999 to 155.5 per 100 000 in 2014 – 2018. From 2016 to 2017, overall cancer mortality dropped by 2.2 %. There were 56 new FDA

approvals of cancer drugs between November 2017 and October 2022.<sup>[31]</sup> Nonetheless, the death toll of cancer remains high, and new treatment options are urgently needed.<sup>[18]</sup>

## 2.2 Natural products to treat cancer

From January 1981 to September 2019, 247 new chemical entities (NCEs) were approved as treatments for cancer. 185 (75%) of these were non-biologics and vaccines. Eighteen NCEs were natural products, and 43 were natural product-derived molecules.<sup>[6]</sup> Paclitaxel and its derivatives are examples of a natural product and natural product-derived molecules that are highly successful as anticancer drugs (Figure 5A). Paclitaxel was isolated from the Pacific yew tree (*Taxus brevifolia*). Paclitaxel and its derivatives bind to  $\beta$ -tubulin and thereby stabilize microtubules. This suppresses their dynamic behavior and leads to mitotic arrest and cell death.<sup>[32]</sup> Camptothecin is a Topoisomerase I inhibitor isolated from the happy tree's bark and wood (*Camptotheca acuminata*).<sup>[33]</sup> Due to unfavorable physicochemical properties and unwanted side effects, camptothecin is not actively used as a drug. However, its derivatives with more favorable properties, such as topotecan and irinotecan, are in use (Figure 5B).<sup>[34]</sup> Another mechanism of antitumor natural products is the binding and alkylation of DNA. An example of an alkylating agent is the natural product duocarmycin A, isolated from *Streptomyces* (Figure 5C).<sup>[35]</sup>

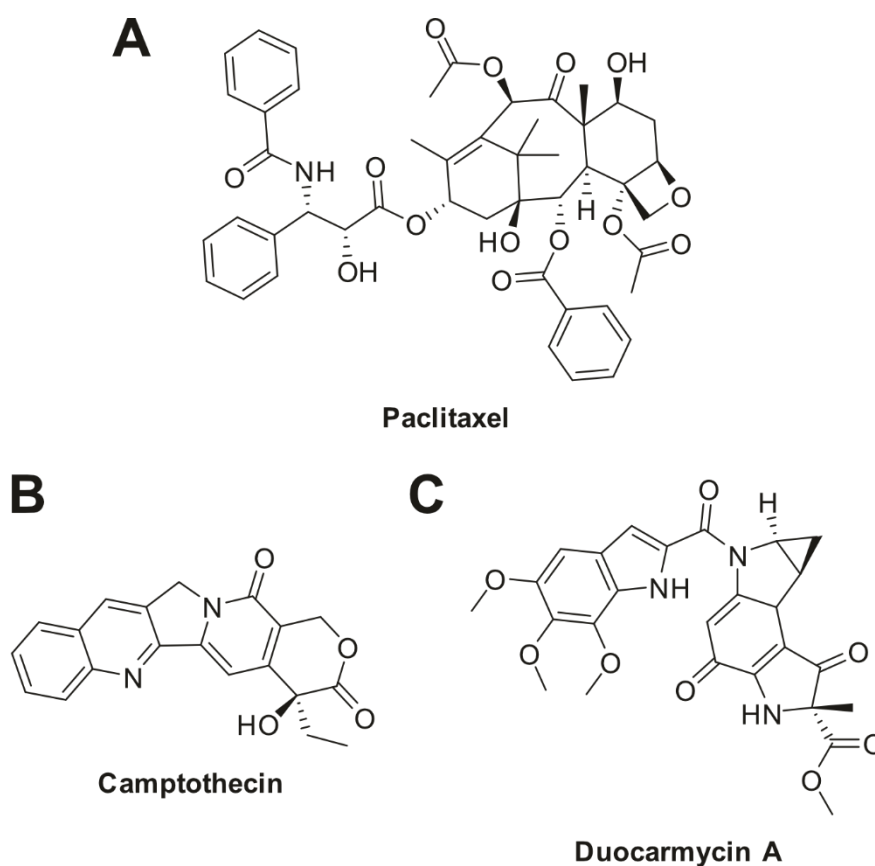


**Figure 5.** Natural products with anticancer activity. (A) paclitaxel, (B) camptothecin, (C) duocarmycin A.

Natural products can help to find new strategies to fight cancer. One promising example is molecular glues. Molecular glues induce novel or stabilize natural protein-protein interactions (PPIs) by forming a ternary complex with the target proteins. Molecular glues gained much interest mainly because they can target proteins previously thought to be undruggable due to their lack of a canonical ligand binding site.<sup>[36]</sup> Novel molecular glues are mostly discovered fortuitously, for example, from phenotypic screens of natural products, since the rational chemical design of molecular glues is still in its infancy.<sup>[37]</sup> The molecular glues can have different effects depending on their target proteins by inducing new or stabilizing existing PPIs. Molecular glue degraders, for example, are small molecules that interact with the protein surface of an E3 ligase and a target protein to induce or enhance the affinity of these proteins for each other and thereby cause the formation of a ternary complex. The proximity of the target protein and the E3 ligase can lead to ubiquitination of the target protein by the E3 ligase and its subsequent degradation by the proteasome.<sup>[36]</sup> Auxine, a natural product from plants, is an example of a natural product, molecular glue (Figure 6A). Auxine binds to TIR1, a part of the SCF<sup>TIR1</sup> E3 ligase complex, stabilizes the interaction of TIR1 and Aux/IAA, and leads to Aux/IAA degradation.<sup>[38]</sup> Asukamycin, a manumycin family polyketide, is another example of a natural product that has been shown to act as a molecular glue (Figure 6B). Asukamycin binds covalently to the putative E3 ligase UBR7 and binds to the neosubstrate TP53, a tumor suppressor. This leads to p53 transcriptional activation and to cell death.<sup>[39]</sup>

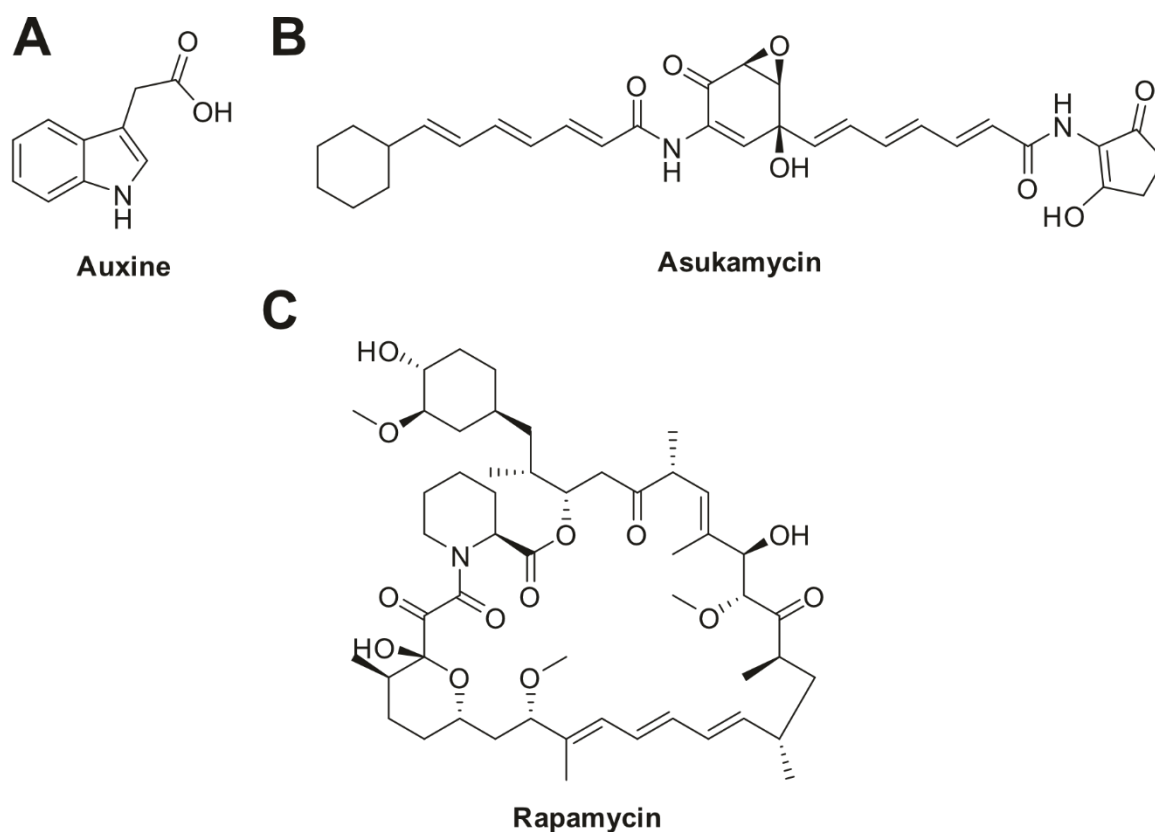


**Figure 6.** Natural products acting as a molecular glue. (A) auxine, (B) asukamycin, (C) rapamycin.

Rapamycin, another natural product molecular glue, reduces cancer cell growth by inhibiting mTor, another signaling kinase (Figure 6C).<sup>[40]</sup> The interaction of rapamycin with FKBP12 and the FRB domain of mTOR causes these effects.<sup>[41]</sup>

Another interesting mechanism is mediated by lasonolide A. Lasonolide A is a polyketide natural product isolated from *Forcepia*, a marine sponge from the Gulf of Mexico (Figure 7A).<sup>[42]</sup> It is highly cytotoxic and kills cancer cells at low nanomolar concentrations.<sup>[42a]</sup> Dubey *et al.* used a genetic screen in a haploid human cell line (Hap1) to unravel the target of lasonolide A. They found that inactivation of LDAH (lipid droplet associated hydrolase), a metabolite serine hydrolase, made cells resistant to lasonolide A. LDAH activity was required for lasonolide cytotoxicity, but LDAH deficient mice were still viable, suggesting that LDAH is not the target responsible for the cytotoxic effect of lasonolide A. Dubey *et al.* discovered that lasonolide A is a prodrug and LDAH cleaves the sidechain ester. The cleavage of the ester yields lasonolide F (Figure 7B). The more hydrophobic lasonolide A is more cell-permeable compared to lasonolide F. Lasonolide F has mostly been found in the cytoplasm, suggesting that the target can be found there.<sup>[43]</sup> However, the target responsible for the cytotoxic effect of lasonolide A is still unknown.

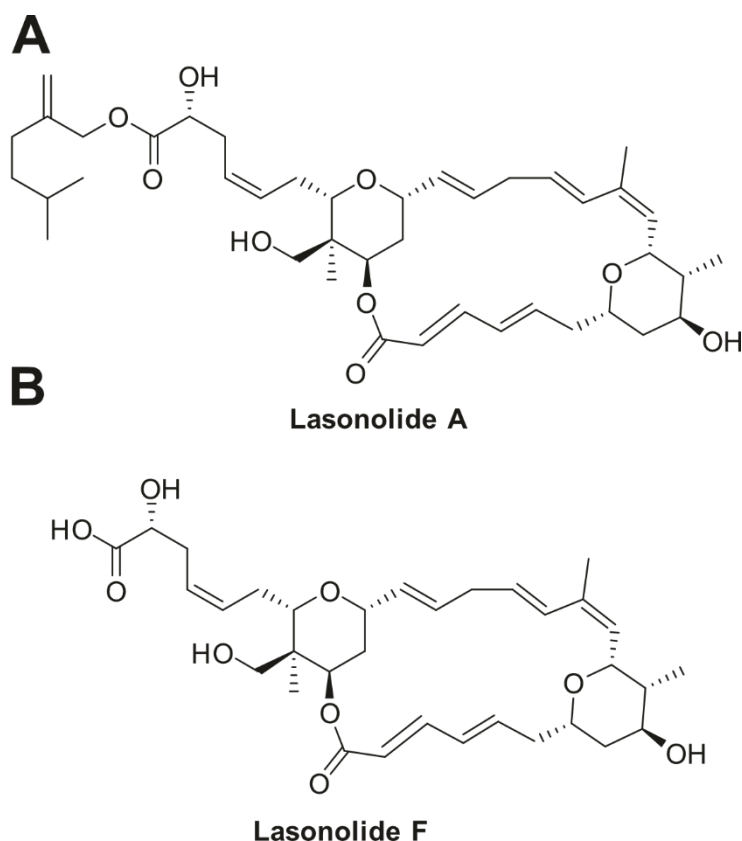


**Figure 7.** Structure of Lasonolides. (A) Structure of lasonolide A. (B) Structure of lasonolide F.

### 3. Natural products and bacterial infections

#### 3.1 Bacterial infections

A study found that there were 13.7 million deaths related to infections in 2019. On average, 99.6 deaths per 100 000 are associated with these pathogens. *Staphylococcus aureus* alone was responsible for over 1 million deaths, and *Escherichia coli*, *Staphylococcus pneumoniae*, *Klebsiella pneumoniae*, and *Pseudomonas aeruginosa* were responsible for more than 500,000 deaths.<sup>[44]</sup> These numbers will likely further increase in the future due to the emergence of antimicrobial resistance (AMR). The evolution of the bacterial genome causes bacterial resistance to antibiotics under selective pressure by antibiotics.<sup>[45]</sup> The bacteria can evolve to incorporate one or more mechanisms of resistance. Mechanisms by which bacteria acquire resistance to antibiotics can be reduced permeability of their outer membrane, increased efflux, changes in the antibiotic's target, or inactivation of the antibiotic.<sup>[46]</sup> A study estimates that 4.95 million deaths were associated with bacterial AMR in 2019. *Escherichia coli*, *Staphylococcus aureus*, *Klebsiella pneumoniae*, *Staphylococcus pneumoniae*, *Acinetobacter baumannii*, and *Pseudomonas aeruginosa* were responsible for the most fatalities in.<sup>[47]</sup> The death toll of antimicrobial resistance could reach 10 million per year by 2050, surpassing even that of cancer. There are estimates that AMR could reduce the gross

domestic product by 2 to 3.5 % by 2050.<sup>[48]</sup> Antibiotics not only cure infections but also enable life-extending medical procedures by making it possible to manage infections.<sup>[49]</sup> Many advances in medicine, like surgery, cancer chemotherapy, or organ transplantation, rely heavily on working antimicrobials, and increasing antimicrobial resistance threatens these advances. A study calculated in 2015 that 26.8 % of pathogens causing infections after chemotherapy and between 38 % and 50 % of bacteria causing surgical site infections are already resistant to standard prophylactic antibiotics in the United States.<sup>[50]</sup> Another medical condition where antimicrobials increase the chance of survival is sepsis. Sepsis is a potentially deadly organ dysfunction caused by a dysregulated host response to an infection.<sup>[51]</sup> There were a total of 11 million sepsis-related deaths and 48.9 million cases of sepsis worldwide in 2017.<sup>[52]</sup> Sepsis can be caused by bacteria reaching the bloodstream from a local site of infection.<sup>[51, 53]</sup> The treatment of sepsis includes an adequate antibiotic to control the infection.<sup>[54]</sup> A potential cause for sepsis can be infected implants. These implants can be the site of chronic infections and thus serve as a source of bacterial inoculation into the bloodstream.<sup>[55]</sup> Most chronic infections are associated with bacterial biofilms.<sup>[56]</sup> Bacterial biofilms are aggregates of bacteria where the cells are embedded in an extracellular polymeric substance (EPS). These communities of bacteria can either attach to a surface or exist as free-floating flocs.<sup>[57]</sup> The EPS mainly consists of polysaccharides, proteins, nucleic acids, and lipids and has several functions. It provides mechanical stability to biofilms, mediates their adhesion to surfaces, serves as an external digestive system, and protects them from desiccation.<sup>[57-58]</sup> Furthermore, it contributes to the increased tolerance to antibiotics of bacteria in biofilms compared to planktonic bacteria, as the EPS restricts the penetration of some antibiotics into the biofilm. Due to the limited penetration of oxygen and nutrients into the biofilm, bacteria in the biofilm tend to have lower metabolic activity, making them less susceptible to antibiotics that target metabolic processes (e.g., replication or cell wall synthesis). Furthermore, a subpopulation of bacteria in the biofilm forms so-called persister cells that divide slowly or not at all, making them less susceptible to antibiotics.<sup>[59]</sup> These three factors make biofilms less susceptible to antibiotics compared to planktonic bacteria. This is especially problematic if the biofilms form on medical implants (e.g., artificial joints or catheters). The formation of these bacterial communities on a medical implant can lead to chronic and/or relapsing infection, frequently leading to device failure and the need for implant removal/replacement, thereby creating additional healthcare costs and patient suffering.<sup>[60]</sup> Since established biofilms are difficult to treat due to their increased antibiotic tolerance, the goal is to prevent their formation. Sterile surgery techniques and perioperative antibiotic treatment are the current standards to prevent surgical site infection.<sup>[61]</sup> The prevention and treatment of bacterial infections in the form of planktonic bacteria and bacterial biofilms require potent antibiotic compounds.

Antimicrobial resistance renders established antibiotics ineffective, and new antibiotics are urgently needed.

### 3.2 Natural products as antibiotics

Since the discovery of penicillin by Alexander Fleming, natural products have been the foundation for the development of new antibiotics, and today, natural products represent a significant portion of all antibiotics. Most of the classes of antibiotics that are in use today are based on natural products (e.g., lactams, macrolides, and glycopeptides), and only a minority is of purely synthetic origin (e.g., sulfonamides, fluoroquinolones, and oxazolidinones).<sup>[62]</sup> Of the 162 new chemical entities approved as antibacterial drugs between January 1981 and September 2019, 11 were natural products, and 78 were natural product derived.<sup>[6]</sup> 3 % of FDA-approved antibiotic natural products are of plant origin, 46 % are from fungi, and 51 % are from bacteria (Figure 8).<sup>[63]</sup>

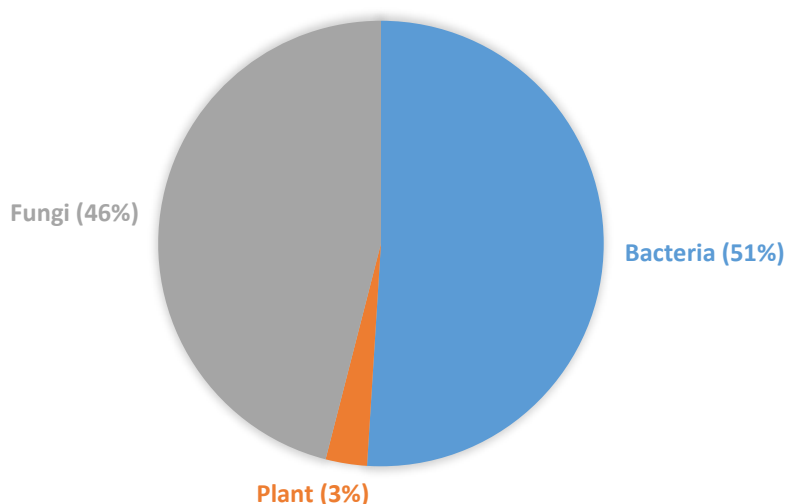


**Figure 8.** Origin of FDA-approved antibacterial natural products. Figure adapted from Patridge *et al.*<sup>[63]</sup>

Soil bacteria produce many antibiotic natural products. From 1955 to 1962, 80% of antibiotics originated from actinomycetes, and *Streptomyces* are known to be the largest antibiotic-producing genus.<sup>[64]</sup> Through these secondary metabolites, *Streptomyces* gain a competitive advantage over other microorganisms in their surroundings.<sup>[65]</sup> Streptomycin is an example of an antibacterial produced by a strain of *Streptomyces* (*Streptomyces griseus*) and was already isolated in 1944 (Figure 9A).<sup>[66]</sup> Streptomycin inhibits protein synthesis by binding to the 30S-subunit of the ribosome.<sup>[67]</sup> Another example of an antibiotic isolated from *Streptomyces* is vancomycin (Figure 9B). Vancomycin inhibits bacterial cell wall synthesis by binding to cell wall precursors.<sup>[68]</sup> Vancomycin was isolated from *Streptomyces orientalis* found in a soil sample from the jungle of Borneo.<sup>[69]</sup>

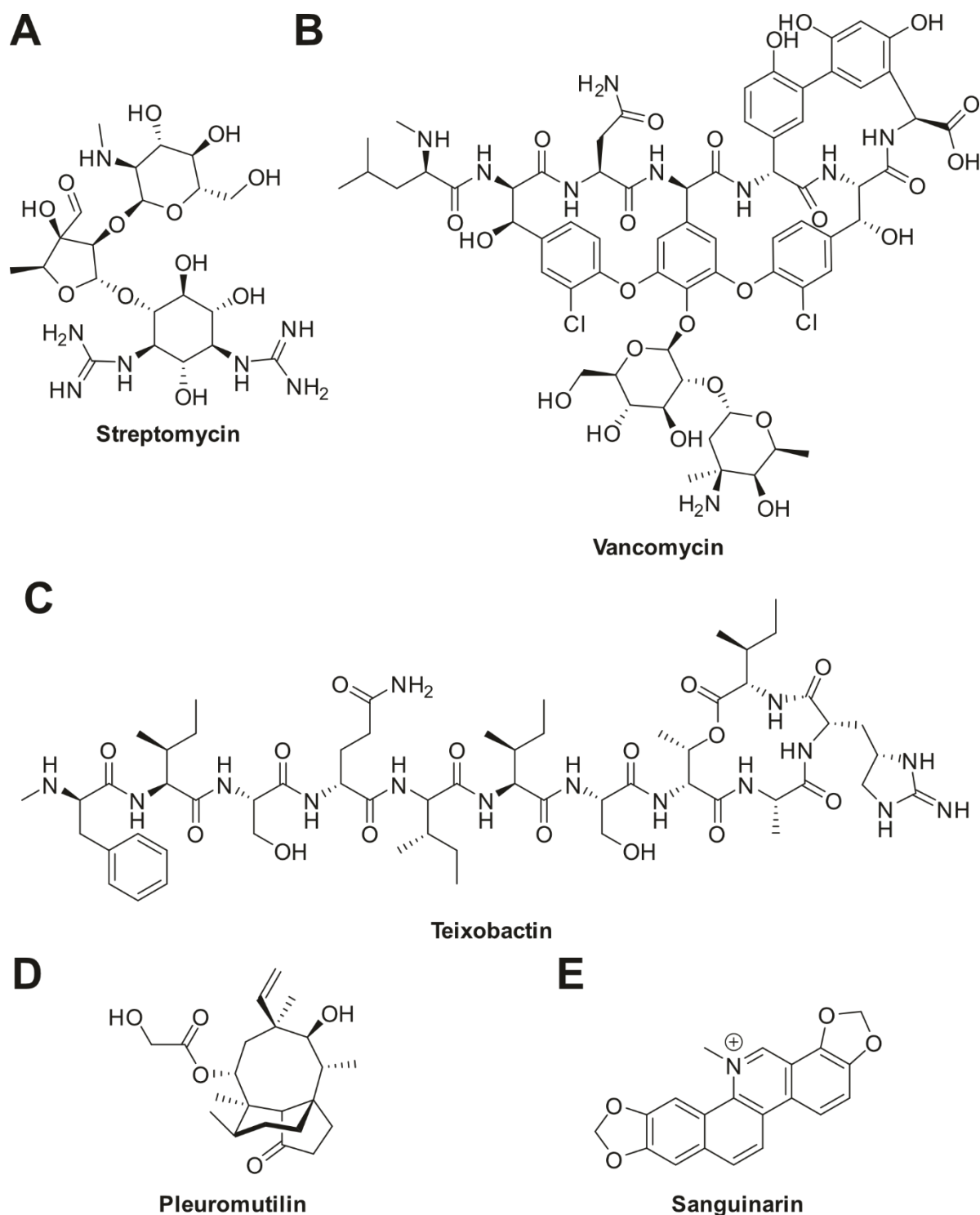


**Figure 9.** Structure of antibiotic natural products. (A) streptomycin, (B) vancomycin, (C) teixobactin, (D) pleuromutilin, (E) sanguinarin.

An estimated 99 % of bacteria can't be cultured under laboratory conditions; therefore, these bacteria might represent an untapped source of novel natural products. Alternative methods have been developed to grow these bacteria to access this unexploited source. The application of a diffusion chamber, for example, led to the discovery of teixobactin from a soil bacterium named *Eleftheria terrae* (Figure 9C). Teixobactin binds to cell wall precursors and thereby inhibits cell wall synthesis.<sup>[70]</sup> But antibiotic natural products are also produced by organisms

other than bacteria. Penicillin was first discovered in a mold (Figure 1B), and so was pleuromutilin (Figure 9D). Pleuromutilin was isolated in 1951 from *Pleurotus mutilus* and inhibits protein synthesis by binding to the ribosome.<sup>[71]</sup> Sanguinarine is an example of a plant-derived, antibiotic natural product (Figure 9E). It can be isolated from plants like *Chelidonium majus* and *Macleaya cordata*.<sup>[72]</sup> These natural products are used to treat or prevent bacterial infections and are routinely used in modern medicine, e.g., surgery and cancer chemotherapy.<sup>[50]</sup> Antibiotic natural products have a vital role in the fight against antimicrobial resistance and there are still many unexploited natural products to be discovered.

## 4. Target identification

Identifying the target of a natural product can lead to new discoveries, and the usefulness of natural products as tool compounds and drugs increases immensely if their molecular targets are known. Target elucidation can reveal new disease-relevant targets and off-targets responsible for side effects. It can aid in improving the initial screening hit by enabling structural biology and structure-based drug design (SBDD). This has made identifying the molecular target an essential part and a bottleneck in drug discovery. For example, the target ID of MI-2 (Figure 10), a known menin inhibitor with anti-tumor activity in diffuse intrinsic pontine glioma (DIPG), revealed Lanosterol-synthase as the target responsible for the anti-tumor effect. DIPG is a disease lacking proven pharmaceutical agents, and this study could show that targeting Lanosterol-synthase and cholesterol biosynthesis, in general, can be therapeutically valuable for DIPG.<sup>[73]</sup>

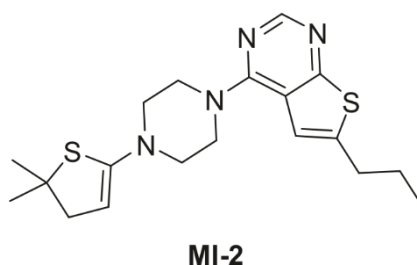


**Figure 10.** Structure of MI-2.

Due to the importance of target identification in drug discovery, various methods to tackle this problem have been developed over the years. A central point to consider here is if the molecule of interest binds covalently or non-covalently to its target. Based on this, different chemoproteomic methods have been developed.

### 4.1 Affinity-based target identification

Small molecules must be modified for target identification. Depending on their affinity for their target, they need functional groups, which allow immobilization on solid supports, an affinity handle, or a biorthogonal group to attach an affinity handle. This need for modification is the biggest drawback of label-based methods as these synthetic modifications can be synthetically challenging, for example, with complex natural products, and they can lead to a loss of on-target activity. Affinity-based methods are used to identify the targets of non-covalent compounds.

#### 4.1.1 Affinity-based pull-downs

The natural product or drug of interest is attached via a linker to a solid support for affinity-based pull-downs. The immobilized molecules are then incubated with cell lysate. The natural

product can additionally be modified with a photoreactive moiety to covalently capture the target proteins after irradiation. Alternatively, the lysate can be preincubated with the small molecule functionalized with a biotin moiety. In the next step, the pretreated lysate is incubated with avidin-coated beads.

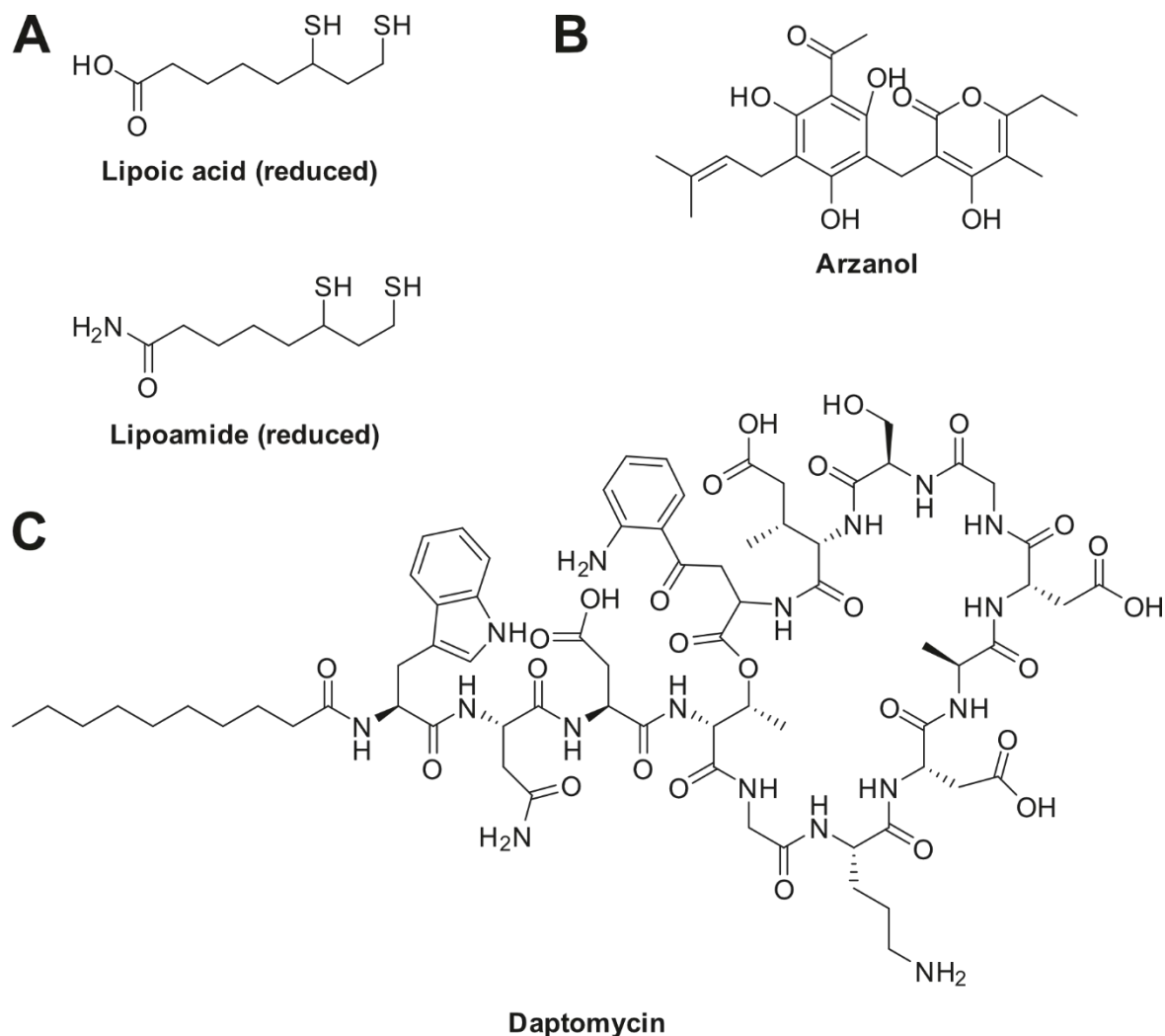


**Figure 11.** Structure of natural products whose target was identified by affinity-based pull-downs. (A) Lipoic acid & lipoamide, (B) arzanol, (C) daptomycin.

The unspecific binders are washed away, and the enriched binders are eluted and identified by mass spectrometry. The attachment of the linker is crucial for retaining the activity.<sup>[74]</sup> Lechner *et al.* used affinity-based pull-downs to identify several histone deacetylases as targets of the reduced form of lipoic acid and lipoamide (Figure 11A).<sup>[75]</sup> In this way, del Gaudio *et al.* identified brain glycogen phosphorylase as the target of the anti-inflammatory natural product arzanol (Figure 11B).<sup>[76]</sup> Biotinylated daptomycin was used by Gotsbacher *et al.* to identify the ribosomal protein S19 as the target of Daptomycin in MCF7 cells (Figure 11C).<sup>[77]</sup>

## 4.1.2 Affinity-based protein profiling (AfBPP)

If the molecule binds only non-covalently to its target, the interaction might be too weak to facilitate target identification. Affinity-based protein profiling (AfBPP) can be used to convert a transient, non-covalent binding event into a stable, covalent bond. For AfBPP, a small, photoreactive moiety, such as a diazirine, benzophenone, or an aryl azide, is attached to the small molecule of interest via a linker. Alternatively, depending on their structural similarity, the photoreactive moiety replaces a portion of the original molecule. A radical/carbene/nitrene is generated upon UV irradiation and crosslinks the probe molecule and the target protein.<sup>[78]</sup> Other functional handles have been included in photocrosslinkers to facilitate target protein enrichment. An alkyne is frequently used, and click chemistry can then be applied to attach a biotin handle to enrich the target proteins on avidin beads (Figure 12).<sup>[79]</sup> After digestion, the enriched proteins can be identified by mass spectrometry.<sup>[74b, 80]</sup>

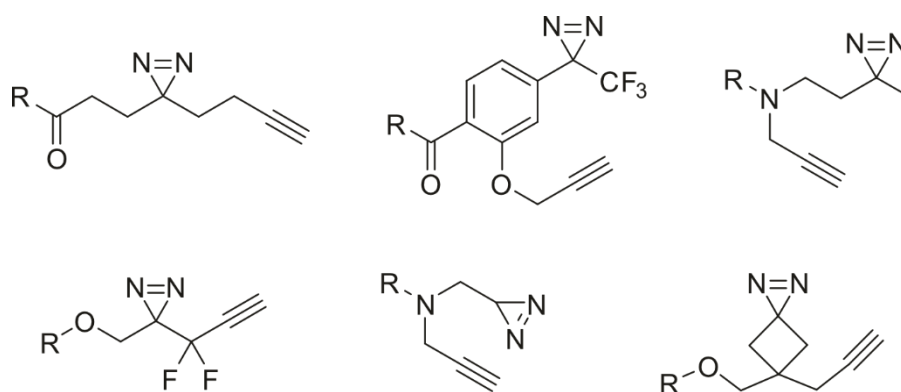


**Figure 12.** Examples of fully functionalized, diazirine-based photoaffinity tags.<sup>[79a, 79b, 81]</sup>

Le *et al.* modified a repurposed kinase inhibitor (Sorafenib, Figure 13A) with a minimalist photocrosslinker to unravel the targets responsible for the antibiotic activity. They identified the signal peptidase SpsB as the target.<sup>[82]</sup> Li *et al.* replaced a naphthalene moiety of LBL1, a pyrroloquinazoline with significant anti-cancer activity, with a diazirine and added an alkyne as a biorthogonal handle. They could show that LBL1 binds to nuclear lamins.<sup>[83]</sup> Tripeptidyl-peptidase 1 (TPP1) was identified by Chen *et al.* as one of the direct targets of nintedanib (BIBF1120), a triple angiokinase inhibitor (Figure 13B). They modified nintedanib with a minimalist photocrosslinker for target identification.<sup>[84]</sup>

AfBPP suffers from similar drawbacks as affinity-based pull-downs. The attachment of the photocrosslinker can lead to a loss of activity. Additionally, it has been shown that photoreactive moieties can lead to unspecific protein binding, and a common set of off-targets has been identified.<sup>[85]</sup>

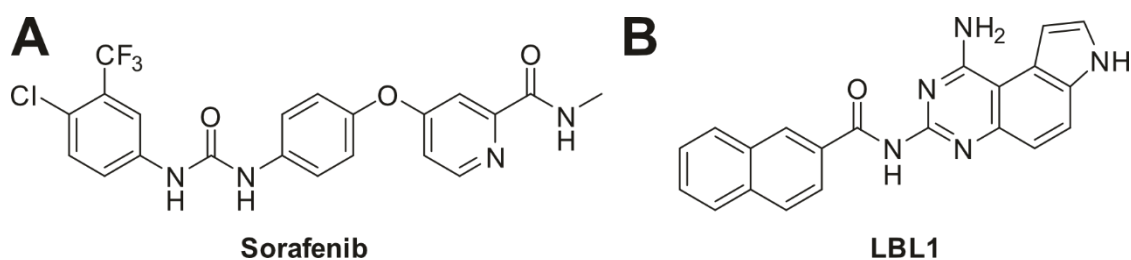


**Figure 13.** Structure of compounds whose target was identified by AfBPP. (A) sorafenib, (B) LBL1.

#### 4.2 Activity-based protein profiling (ABPP)

Many drugs and natural products, such as withaferin A and orlistat, bind their targets covalently. Molecules binding their target covalently usually contain electrophilic moieties that can react with nucleophilic amino acid residues like cysteine or lysine. Activity-based protein profiling (ABPP) is used to identify the targets of covalently binding small molecules.<sup>[86]</sup> The covalent mechanism makes the introduction of bulky linkers and photoreactive moieties unnecessary and, therefore, decreases the risk of activity loss. Only a comparably small biorthogonal handle, most frequently an alkyne due to its size, is required for target enrichment.<sup>[79c]</sup> Zerumbone is a cyclic sesquiterpene with anti-cancer, anti-inflammatory, and cellular detoxification activity (Figure 14A). Kalesh *et al.* used ABPP to profile the targets of zerumbone in HeLa cells.<sup>[87]</sup> Huang *et al.* used ABPP to show that BIA 10-2474, an inhibitor fatty acid amide hydrolase (FAAH) that shows, in contrast to other FAAH inhibitors, adverse neurological effects, additionally targets aldehyde dehydrogenases, including ALDH2 (Figure 14B). ALDH2 has been shown to protect the brain from oxidative stress-related damage.<sup>[88]</sup> Lehmann *et al.* could show by ABPP that the human lysosomal acid lipase inhibitor lalistat inhibits the growth of *Mycobacterium tuberculosis* by targeting bacterial hydrolases (Figure 14C).<sup>[89]</sup>

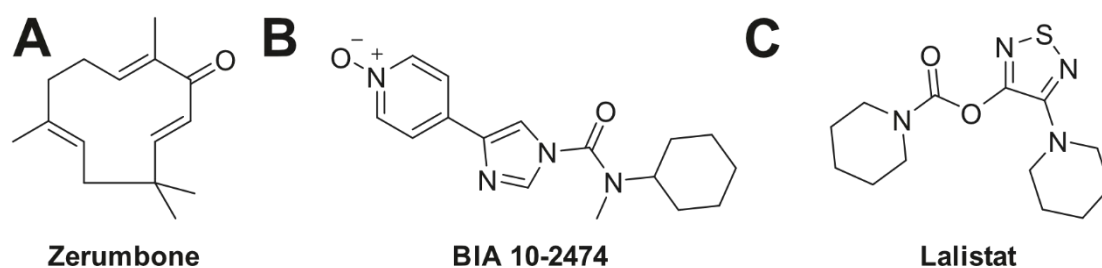


**Figure 14.** Structure of compounds whose target was identified by ABPP. (A) zerumbone, (B) BIA 10-2474, (C) lalistat.

#### 4.3 Tag-free target identification

Affinity- and activity-based methods have been widely applied for target identification. However, label-based methods require modifications of the molecule of interest, such as adding linkers, biorthogonal handles, or photoreactive groups. These modifications can lead to a loss of on-target activity and might be synthetically cumbersome, especially for complex

natural products. Because of this, label-free methods, also called energetics-based proteomics methods, for target identification have been developed. The methods are based on the shift in stability of the target protein to outside stressors upon compound binding. Examples of such stressors are increased temperatures, organic solvents, and proteolysis.

#### 4.3.1 Thermal protein profiling (TPP)

Proteins start to denature and then aggregate and precipitate when they are heated.<sup>[90]</sup> The temperature at which half of the protein is denatured is termed the melting temperature ( $T_m$ ). The melting temperature is intrinsic to a protein. The binding of a ligand to the protein causes changes in the thermal stability and protein flexibility.<sup>[91]</sup> This shift in thermal stability can be used to monitor compound binding.<sup>[92]</sup> The change of thermal stability upon ligand binding can be exploited to monitor target binding in cells or tissue. This method is called cellular thermal shift assay (CETSA).<sup>[93]</sup> Experimentally, tissue, cells, or lysates are treated with the potential ligand or vehicle before being heated to various temperatures. The proteins denature and precipitate depending on their stabilization by the ligand. The residual soluble protein is quantified by western blot and denaturation curves, and differences in melting temperatures ( $\Delta T_m$ ) are determined to confirm drug target engagement. As CETSA relies on Western blotting, it suffers from several drawbacks. The target has to be known, and a suitable antibody has to be available. Thermal protein profiling (TPP) was developed to circumvent these drawbacks. TPP uses mass-spectrometry for detection; hence, it is target-agnostic and does not rely on antibodies.<sup>[94]</sup> TPP samples can either be treated with the same ligand concentration and be heated to a range of different temperatures, or the ligand concentration is varied, and the samples are all heated to the same temperature. The soluble proteins are digested, and the peptides are labeled with 10-plex tandem mass tags (TMTs). The melting curves and melting points are determined, and the target proteins are selected if the compound treatment causes a significant  $\Delta T_m$ .<sup>[95]</sup> The downsides of TPP are the high cost of TMT reagents and the high demand on mass-spectrometry.<sup>[80]</sup> Kirsch *et al.* used TPP to show that vioprolide A, a natural product with prominent potency against human acute lymphoblastic leukemia, targets the nucleolar protein NOP14, a protein essential for ribosomal biogenesis, in Jurkat cells (Figure 15A).<sup>[96]</sup> Calcium-dependent protein kinase 1 was identified as the target of ENH1, a modulator of calcium signaling, by Herneisen *et al.* by TPP in *Toxoplasma* (Figure 15B).<sup>[97]</sup> Dehghan *et al.* used TPP to unravel the target of hydralazine, which is responsible for promoting lifespan in *C. elegans* (Figure 15C). They could show that hydralazine binds to cAMP-dependent protein kinase PKA, leading to an improved mitochondrial function and metabolic homeostasis via the SIRT1/SIRT5 axis.<sup>[98]</sup>

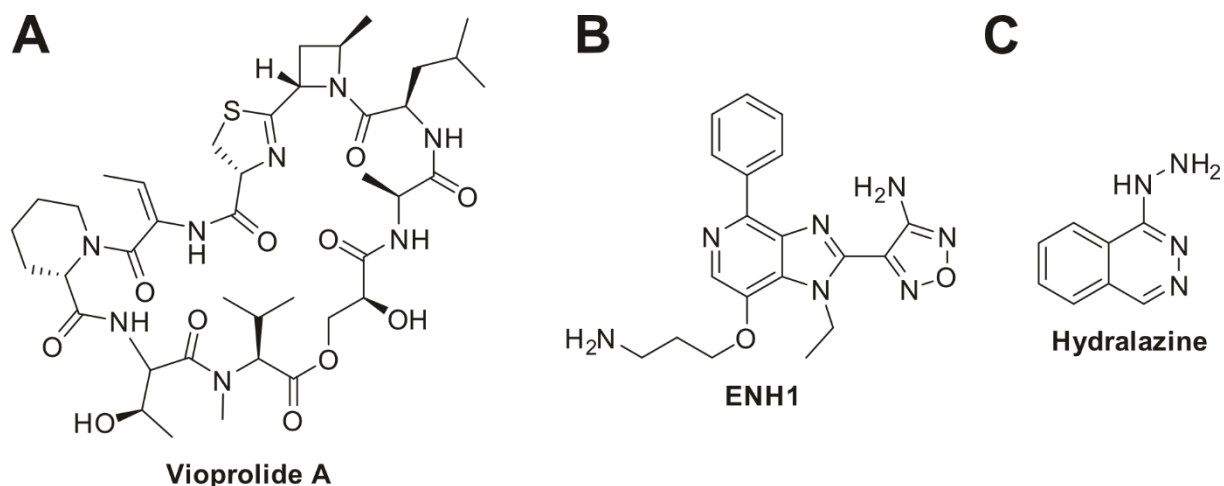


**Figure 15.** Structure of compounds whose target was identified by TPP. (A) vioprolide A, (B) ENH1, (C) hydralazine.

#### 4.3.2 Solvent-induced protein precipitation (SIP)

Zhang *et al.* developed a novel energetics-based proteomics method based on the principle of protein precipitation by organic solvents termed solvent-induced protein precipitation. This precipitation mode differs from thermal denaturation as the organic solvent causes precipitation by decreasing the dielectric constant and competing for hydration. They precipitated proteins by adding a mixture of solvents (acetone/ethanol/acetic acid = 50/50/0.1) to a final percentage of 9% to 19%. Using this technique, they could identify the known targets of methotrexate, SNS-032, and staurosporine (Figure 16A-C).

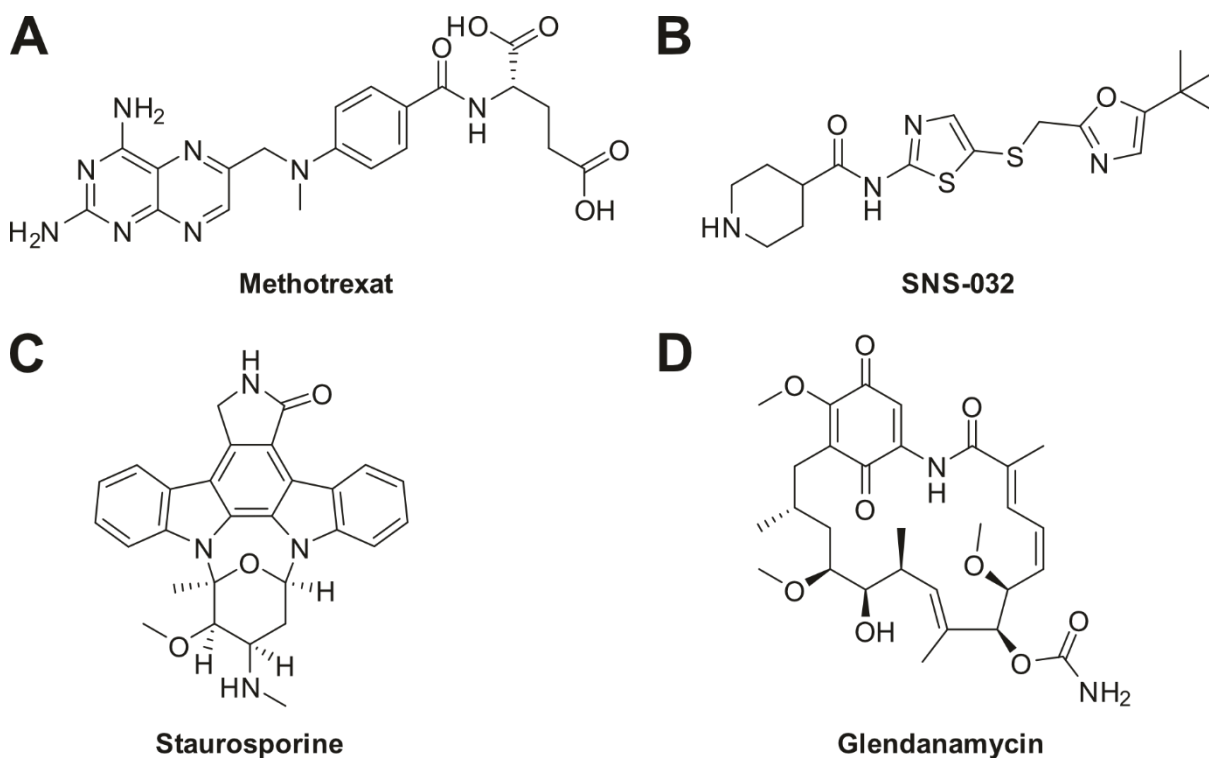


**Figure 16.** Structure of compounds whose target was identified by SIP. (A) methotrexat, (B) SNS-32, (C) staurosporine, (D) glendanamycin.

For glendanamycin, they rediscovered the known targets of the HSP90 family and identified potential off-targets like the NADH dehydrogenase subunits NDUFV1 and NDUFAB1 (Figure 16D).<sup>[99]</sup> Zhang *et al.* did not apply sample multiplexing to quantify complete melting curves on a proteome-wide scale. Independently, Yu *et al.* and van Vranken *et al.* introduced TMT-based multiplexing to improve the analytical depth of SIP. They termed their methods solvent-induced proteome profiling (SIPP) and solvent proteome profiling (SPP), respectively.<sup>[100]</sup>

#### 4.3.3 Drug affinity responsive target stability (DARTS)

It has been demonstrated that proteins are less sensitive to proteases when a ligand is bound.<sup>[101]</sup> On this principle, Lomenick *et al.* developed drug affinity responsive target stability (DARTS). For DARTS, cells or lysate are treated with different concentrations of the ligand of interest or vehicle. Cells are lysed, and the lysate is treated with a non-specific protease, e.g., thermolysin, for a defined period. If a small molecule is bound to the target, its stability to proteolysis increases, and more undigested protein will remain after protease treatment. Similar to CETSA and TPP, this change in stability can be detected by western blotting and mass spectrometry. DARTS can be used to validate target engagement and for unbiased target identification.<sup>[101c, 102]</sup>

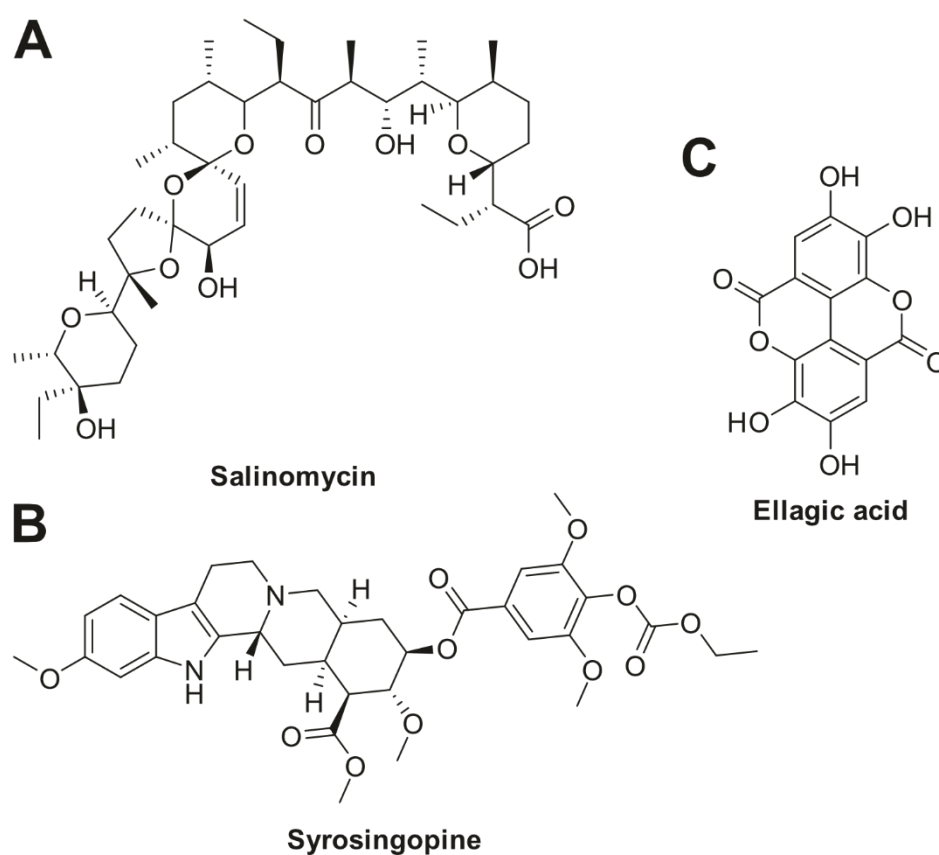


**Figure 17.** Structure of compounds whose target was identified by DARTS. (A) salinomycin, (B) syrosingopine, (C) ellagic acid.

Wang *et al.* used DARTS in SH-SY5Y cells to show that salinomycin, a natural product isolated from *Streptomyces albus* and cancer stem cell killer, binds to the protein nucleolin and suppresses CD34 expression by disrupting the interaction of nucleolin and CD34 promotor (Figure 17A).<sup>[103]</sup> Benjamin *et al.* reported that the anticancer activity of metformin, a widely used antidiabetic, is strongly potentiated by the antihypertensive syrosingopine (Figure 17B). They used DARTS to show that syrosingopine binds to the glycolytic enzyme  $\alpha$ -enolase.<sup>[104]</sup> Ellagic acid is a polyphenol widely found in vegetables and fruit that inhibits breast cancer growth and metastasis (Figure 17C). Applying DARTS, Wang *et al.* could show that ellagic acid binds to ACTN4.<sup>[105]</sup>

#### 4.4 Other methods

Besides the above-described proteomic methods, like activity-based proteome profiling and thermal proteome profiling, computational and genetic techniques have been developed to help with target identification.

##### 4.4.1 Genetic methods

Target ID by genetic methods uses the relative ease of manipulating RNA or DNA and continually improving sequencing techniques. The formation of resistance can render drugs ineffective. However, chemotype-specific resistance also can aid in target identification. As mentioned above, resistance to a drug can emerge by different mechanisms. One mechanism of resistance development is a mutation in the drug's target. If the organism of interest has a high enough rate of mutations, this can be applied for target identification. This strategy has frequently been used in bacteria. Hübner *et al.*, for example, generated mutants of *A. baumannii* resistant to the isonitrile antibiotic xanthocillin (Figure 18).

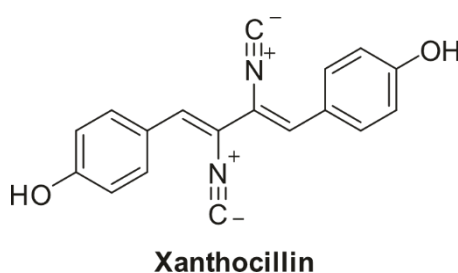


**Figure 18.** The structure of xanthocillin.

Genome sequencing of the resistant mutants showed a single common mutation in the gene *hemB* in the mutants. *hemB* codes for the enzyme porphobilinogen synthase and the mutation caused the amino acid change P241S. Porphobilinogen synthase is involved in tetrapyrrole synthesis, and the mutations result in a reduced rate of tetrapyrrole synthesis. In further studies, Hübner *et al.* could show that xanthocillin stimulates heme biosynthesis, leading to a deficiency in building blocks and increased production in reactive oxygen species, ultimately killing the bacteria.<sup>[106]</sup> The same strategy has been more complicated to realize in human cells.

Kapoor *et al.* give three reasons for that. They state that, although resistance-causing mutants can be generated in human cells, separating them from bystander mutations is difficult. Another reason is the size of the human genome; it is much larger and more complex than, for example, a bacterial genome. As a third reason, they mention the lack of knowledge about the frequently chemo-type specific resistant mutants that arise in the direct protein target of the molecule of interest.<sup>[107]</sup> Recent technological advances have made using resistance mutants for target ID more feasible. Wacker *et al.* could show that they can identify the target of cancer drugs in human cells by transcriptome sequencing. They generated clones of HCT-116 cells with decreased sensitivity to bortezomib, an inhibitor of the proteasomal subunit PSMB5 used to treat multiple myeloma and mantle cell lymphoma, or BI-2536 under investigation as an inhibitor of polo-like kinase (PLK1) (Figure 19A). They chose HCT-116 cells, a human colon cancer cell line, because they have low expression of multidrug-resistant pumps and are deficient in mismatch repair, therefore being more prone to mutations.<sup>[108]</sup> After transcriptome sequencing and bioinformatics analysis, they found five genes mutated in the bortezomib-resistant group, and PSMB5 was the only mutated gene with two distinct mutations. For BI-2536, they identified PLK1 as the only gene mutated in more than one group of resistant clones. They could demonstrate that this approach is viable for target ID of cancer drugs in human cells.<sup>[109]</sup>

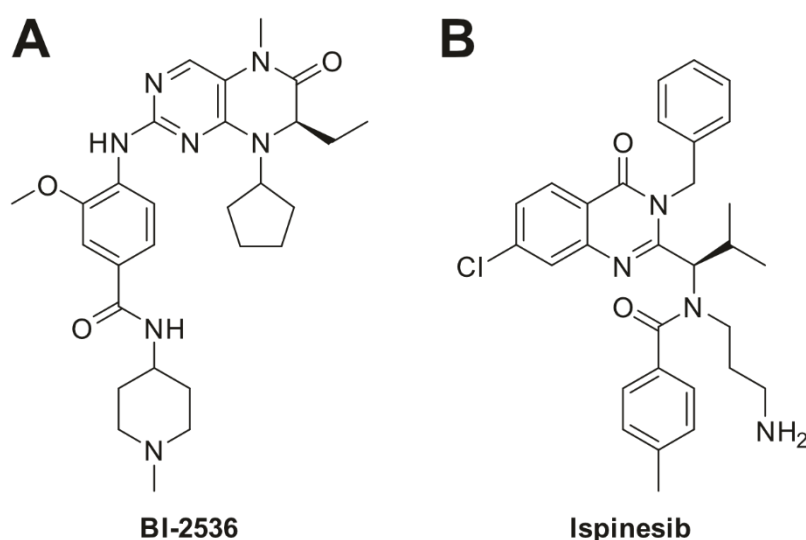
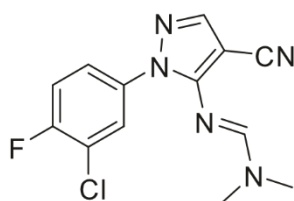


**Figure 19.** Structures of BI-2536 (A) und ispinesib (B).

The same group tested this technique by studying the target of ispinesib, an inhibitor of kinesin-5 (Figure 19B). The isolated 12 clones were 70-300 fold less sensitive than their parent clone. 4 of these 12 clones displayed resistance to known efflux pump substrates, indicating that their ispinesib resistance is not chemotype specific but caused by drug efflux. They sequenced the transcriptome of the remaining 8 clones and conducted bioinformatics analysis. Only one gene was commonly mutated in more than two clones, kinesin-5. Kinesin-5 was mutated in all 8 clones, and they found a total of three different mutations in kinesin-5.

CRISPR-CAS9 was used to study the importance of these mutations in more detail. They called this technique DrugTargetSeqR.<sup>[110]</sup> RNA interference (RNAi) is a prominent genetic method to identify and validate target proteins. RNAi is an RNA-silencing mechanism that works in four steps. First, RNase III Dicer cleaves long double-stranded RNA into small interfering RNA (siRNA). These strands of siRNA are then loaded onto an Argonaute protein, forming the RNA-induced silencing complex (RISC). The siRNA guides the RISC complex to its target RNA, and in the last step, the Argonaute protein cleaves the target RNA.<sup>[111]</sup> The siRNA can be chemically synthesized, and thereby, proteins of desire are accessible for knock down. A small molecule and an RNAi library can be assayed in parallel, and matching cellular phenotypes are indicators for the small molecule target. Eggert *et al.* performed a genome-wide RNA interference screen to identify proteins involved in cytokinesis and a chemical genetic screen for molecules inhibiting these proteins in *Drosophila*. They identified 214 genes essential for cytokinesis and 50 small molecule inhibitors of cytokinesis. *N'*-[1-(3-chloro-4-fluorophenyl)-4-cyano-1H-pyrazol-5-yl]-*N,N*-dimethyliminoforamide caused abnormal mitosis, malformed spindles and misaligned chromosomes (Figure 20). The same phenotype was caused by RNAi depletion of Aurora B or INCEP, a complex partner of Aurora B. This indicates that the small molecule inhibits cytokinesis by interfering with the Aurora B pathway.<sup>[112]</sup>



***N'*-[1-(3-chloro-4-fluorophenyl)-4-cyano-1H-pyrazol-5-yl]-*N,N*-dimethyliminoforamide**

**Figure 20.** Structure of *N'*-[1-(3-chloro-4-fluorophenyl)-4-cyano-1H-pyrazol-5-yl]-*N,N*-dimethyliminoforamide.

Phages can also be used for target ID. Phages are viruses that only infect bacteria. To use phage display for small molecule target discovery, a set of DNA sequences as a fusion with genes coding for the phage coat protein is cloned into phages. The small molecule of interest is immobilized on a solid support. This can be used to enrich the phages expressing the proteins with high enough affinity for the small molecule. These can then be eluted and amplified in bacteria. This new set of phages is greatly enriched with the phages coding for the target protein. After iterative rounds of this enrichment, the binding protein can be identified by sequencing the enriched phages after isolating their DNA.<sup>[113]</sup> This strategy was used to determine the target responsible for the potent anti-proliferative effect of a curcumin derivative called HBC (Figure 21). This could show that HBC interferes with  $\text{Ca}^{2+}$ /calmodulin in a Calcium-dependent manner.<sup>[114]</sup>

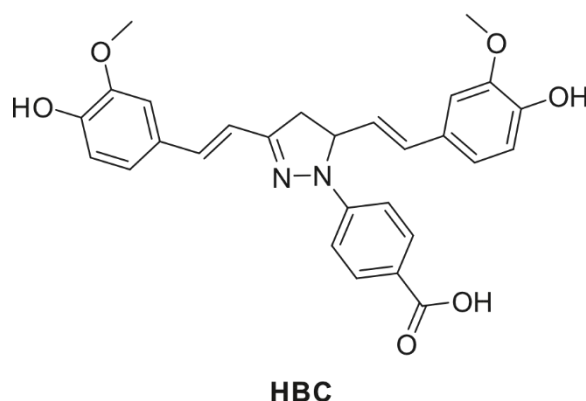


**Figure 21.** Structure of the curcumin derivative HBC.

#### 4.4.2 Computational methods

Advancements in computing power and areas like machine learning led to the development of *in silico* target prediction methods as a cost- and time-effective addition to or alternative to experimental techniques. *In silico*, target prediction is a growing field that is steadily improving. Similarity search, known as molecular similarity, is the simplest and fastest way for *in silico* target prediction. Similarity search is based on the assumption that similar molecules have the same targets. Therefore, the molecule of interest is compared to a database of small molecules with known targets (e.g., ChEMBL or PubChem), and the database compounds are ranked according to their similarity to the molecule of interest. It is then assumed that the molecule shares the target with the most similar compound from the database. This approach has several drawbacks. If the target is novel and no ligands for the target are known, similarity search fails to predict it. Furthermore, if a molecule has been altered at a key position, it might lose its affinity for a target while still being structurally very similar to the original molecule, resulting in a false positive.<sup>[115]</sup>

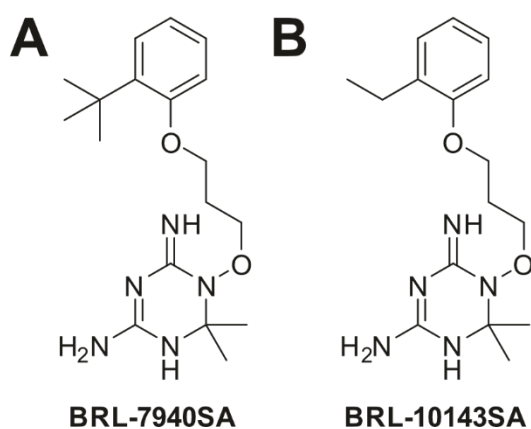


**Figure 22.** Structures of BRL-7940SA (A) and BRL-10143SA (B).

While similarity search methods treat all compound parameters equally, statistical methods that evaluate each parameter's importance for biological activity can be developed. During the

training phase of machine learning models, such a statistical model is fitted to a set of known active and inactive compounds.<sup>[115]</sup> Mugumbate *et al.* used a similarity-based and a machine learning-based approach to predict dihydrofolate reductase as the target of BRL-7940SA and BRL-10143SA active against *Mycobacterium tuberculosis* (Figure 22). They could show that the compounds inhibit the protein *in vitro*.<sup>[116]</sup> Docking is also a valuable tool for target prediction. For this application, a single molecule is docked to different proteins; this strategy is called reverse docking. The possible targets can be ranked by the interaction energies. Chen *et al.* demonstrated that reverse docking can successfully locate the target protein in the top 20 targets for over 50 % of the tested anti-tumor natural products.<sup>[117]</sup> Gong *et al.* isolated a novel cytotoxic steroid, swinhoeisterol A (Figure 23A), from the sponge *Theonella swinhoei*. They used reverse docking to narrow down potential targets and evaluated the ten highest-ranking targets in *in vitro* biological assays. They could show that swinhoeisterol A inhibits the histone acetyltransferase (h)p300 with an  $IC_{50}$  of 2.9  $\mu$ M.<sup>[118]</sup> A similar tactic was used by Lauro *et al.* to elucidate the target of the phenolic natural product xanthohumol (Figure 23B). Reverse docking to 163 targets involved in cancer processes hinted at phosphoinositide-dependent kinase 1 (PDK1) as a possible target, and they confirmed that with an *in vitro* assay, determining an  $IC_{50}$  of xanthohumol of 6.6  $\mu$ M.<sup>[119]</sup>

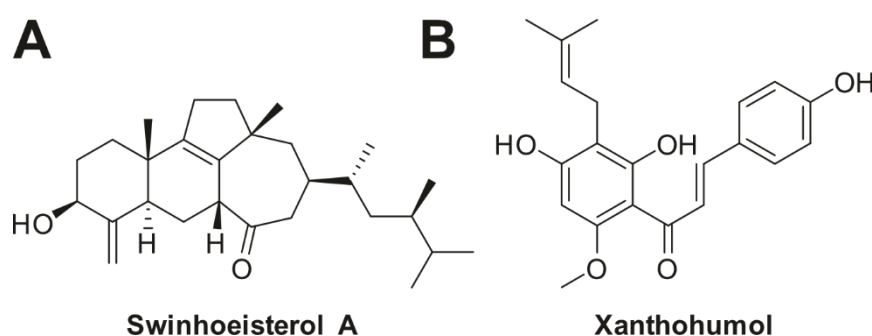


**Figure 23.** Structures of swinhoeisterol (A) and xanthohumol (B).

## 5. References

- [1] P. S. Baran, *Journal of the American Chemical Society* **2018**, *140*, 4751-4755.
- [2] A. G. Atanasov, B. Waltenberger, E.-M. Pferschy-Wenzig, T. Linder, C. Wawrosch, P. Uhrin, V. Temml, L. Wang, S. Schwaiger, E. H. Heiss, J. M. Rollinger, D. Schuster, J. M. Breuss, V. Bochkov, M. D. Mihovilovic, B. Kopp, R. Bauer, V. M. Dirsch, H. Stuppner, *Biotechnology Advances* **2015**, *33*, 1582-1614.
- [3] a.) U. W. Yun, Z. Yan, R. Amir, S. Hong, Y. W. Jin, E. K. Lee, G. J. Loake, *Biotechnol Genet Eng Rev* **2012**, *28*, 47-59; b.) G. R. Hamilton, T. F. Baskett, *Can J Anaesth* **2000**, *47*, 367-374.
- [4] a.) E. Chain, H. W. Florey, A. D. Gardner, N. G. Heatley, M. A. Jennings, J. Orr-Ewing, A. G. Sanders, *The Lancet* **1940**, *236*, 226-228; b.) M. C. Wani, H. L. Taylor, M. E. Wall, P. Coggon, A. T. McPhail, *Journal of the American Chemical Society* **1971**, *93*, 2325-2327; c.) J. Wang, C. Xu, Y. K. Wong, Y. Li, F. Liao, T. Jiang, Y. Tu, *Engineering* **2019**, *5*, 32-39.
- [5] Y. Tu, *Angewandte Chemie International Edition* **2016**, *55*, 10210-10226.
- [6] D. J. Newman, G. M. Cragg, *Journal of Natural Products* **2020**, *83*, 770-803.
- [7] Y. Chen, M. Garcia de Lomana, N.-O. Friedrich, J. Kirchmair, *Journal of Chemical Information and Modeling* **2018**, *58*, 1518-1532.
- [8] a.) T. Henkel, R. M. Brunne, H. Muller, F. Reichel, *Angew Chem Int Ed Engl* **1999**, *38*, 643-647; b.) M. Feher, J. M. Schmidt, *J Chem Inf Comput Sci* **2003**, *43*, 218-227.
- [9] Y. Chen, J. Kirchmair, *Mol Inform* **2020**, *39*, e2000171.
- [10] H. Chen, O. Engkvist, N. Blomberg, J. Li, *MedChemComm* **2012**, *3*, 312-321.
- [11] F. Lovering, J. Bikker, C. Humblet, *Journal of Medicinal Chemistry* **2009**, *52*, 6752-6756.
- [12] P. D. Leeson, B. Springthorpe, *Nature Reviews Drug Discovery* **2007**, *6*, 881-890.
- [13] F. Lovering, *MedChemComm* **2013**, *4*, 515-519.
- [14] X. Wang, N. Greene, *Mol Inform* **2012**, *31*, 145-159.
- [15] C. R. Pye, M. J. Bertin, R. S. Lokey, W. H. Gerwick, R. G. Linington, *Proc Natl Acad Sci U S A* **2017**, *114*, 5601-5606.
- [16] a.) G. Karageorgis, D. J. Foley, L. Laraia, S. Brakmann, H. Waldmann, *Angewandte Chemie International Edition* **2021**, *60*, 15705-15723; b.) M. Grigalunas, S. Brakmann, H. Waldmann, *Journal of the American Chemical Society* **2022**, *144*, 3314-3329.
- [17] a.) O. O. Olaku, E. A. Taylor, *Primary Care: Clinics in Office Practice* **2017**, *44*, 87-97; b.) M. R. Stratton, P. J. Campbell, P. A. Futreal, *Nature* **2009**, *458*, 719-724; c.) M. R. Stratton, *Science* **2011**, *331*, 1553-1558; dF. Martínez-Jiménez, F. Muiños, I. Sentís, J. Deu-Pons, I. Reyes-Salazar, C. Arnedo-Pac, L. Mularoni, O. Pich, J. Bonet, H. Kranas, A. Gonzalez-Perez, N. Lopez-Bigas, *Nature Reviews Cancer* **2020**, *20*, 555-572.
- [18] H. Sung, J. Ferlay, R. L. Siegel, M. Laversanne, I. Soerjomataram, A. Jemal, F. Bray, *CA: A Cancer Journal for Clinicians* **2021**, *71*, 209-249.
- [19] K. A. Cronin, S. Scott, A. U. Firth, H. Sung, S. J. Henley, R. L. Sherman, R. L. Siegel, R. N. Anderson, B. A. Kohler, V. B. Benard, S. Negoita, C. Wiggins, W. G. Cance, A. Jemal, *Cancer* **2022**, *128*, 4251-4284.
- [20] R. L. Siegel, K. D. Miller, N. S. Wagle, A. Jemal, *CA: A Cancer Journal for Clinicians* **2023**, *73*, 17-48.
- [21] N. Rivlin, R. Brosh, M. Oren, V. Rotter, *Genes & Cancer* **2011**, *2*, 466-474.
- [22] a.) Z. Waks, O. Weissbrod, B. Carmeli, R. Norel, F. Utro, Y. Goldschmidt, *Scientific Reports* **2016**, *6*, 38988; b.) E. N. KONTOMANOLIS, A. KOUTRAS, A. SYLLAIOS, D. SCHIZAS, A. MASTORAKI, N. GARMPIIS, M. DIAKOSAVVAS, K. ANGELOU, G. TSATSARIS, A. PAGKALOS, T. NTOUNIS, Z. FASOULAKIS, *Anticancer Research* **2020**, *40*, 6009-6015.
- [23] V. Llombart, M. R. Mansour, *EBioMedicine* **2022**, *75*, 103756.
- [24] a.) D. Hanahan, R. A. Weinberg, *Cell* **2000**, *100*, 57-70; b.) D. Hanahan, *Cancer Discovery* **2022**, *12*, 31-46; cD. Hanahan, Robert A. Weinberg, *Cell* **2011**, *144*, 646-674.
- [25] K. Shi, G. Wang, J. Pei, J. Zhang, J. Wang, L. Ouyang, Y. Wang, W. Li, *Journal of Hematology & Oncology* **2022**, *15*, 94.
- [26] R. Shah, J. F. Lester, *Clinical Lung Cancer* **2020**, *21*, e216-e228.

- [27] S. J. Jang, J. M. Gardner, J. Y. Ro, *Advances in Anatomic Pathology* **2011**, *18*.
- [28] A. W. Lambert, D. R. Pattabiraman, R. A. Weinberg, *Cell* **2017**, *168*, 670-691.
- [29] a.) C. A. Bradley, P. D. Dunne, V. Bingham, S. McQuaid, H. Khawaja, S. Craig, J. James, W. L. Moore, D. G. McArt, M. Lawler, S. Dasgupta, P. G. Johnston, S. Van Schaeybroeck, *Oncotarget* **2016**, *7*, 78932-78945; b.) Y. C. Lim, J. H. Han, H. J. Kang, Y. S. Kim, B. H. Lee, E. C. Choi, C.-H. Kim, *Oral Oncology* **2012**, *48*, 1114-1119; c.) T. Qin, Y. Xiao, W. Qian, X. Wang, M. Gong, Q. Wang, R. An, L. Han, W. Duan, Q. Ma, Z. Wang, *Cell Death & Disease* **2022**, *13*, 387.
- [30] a.) L. Demkova, L. Kucerova, *Molecular Cancer* **2018**, *17*, 26; b.) F. Blackhall, F. Cappuzzo, *Annals of Oncology* **2016**, *27*, iii35-iii41.
- [31] E. C. Scott, A. C. Baines, Y. Gong, R. Moore, G. E. Pamuk, H. Saber, A. Subedee, M. D. Thompson, W. Xiao, R. Pazdur, V. A. Rao, J. Schneider, J. A. Beaver, *Nature Reviews Drug Discovery* **2023**, *22*, 625-640.
- [32] a.) J. F. Diaz, M. Menendez, J. M. Andreu, *Biochemistry* **1993**, *32*, 10067-10077; b.) P. B. Schiff, J. Fant, S. B. Horwitz, *Nature* **1979**, *277*, 665-667; cA. M. Yvon, P. Wadsworth, M. A. Jordan, *Mol Biol Cell* **1999**, *10*, 947-959.
- [33] a.) Y. Pommier, *Nature Reviews Cancer* **2006**, *6*, 789-802; b.) N. H. Oberlies, D. J. Kroll, *Journal of Natural Products* **2004**, *67*, 129-135; c.) E. Martino, S. Della Volpe, E. Terribile, E. Benetti, M. Sakaj, A. Centamore, A. Sala, S. Collina, *Bioorganic & Medicinal Chemistry Letters* **2017**, *27*, 701-707.
- [34] M. Huang, J.-J. Lu, J. Ding, *Natural Products and Bioprospecting* **2021**, *11*, 5-13.
- [35] a.) I. Takahashi, K. Takahashi, M. Ichimura, M. Morimoto, K. Asano, I. Kawamoto, F. Tomita, H. Nakano, *J Antibiot (Tokyo)* **1988**, *41*, 1915-1917; b.) J. G. Felber, O. Thorn-Seshold, *JACS Au* **2022**, *2*, 2636-2644.
- [36] J. M. Sasso, R. Tenchov, D. Wang, L. S. Johnson, X. Wang, Q. A. Zhou, *Biochemistry* **2023**, *62*, 601-623.
- [37] a.) E. S. Toriki, J. W. Papatzimas, K. Nishikawa, D. Dovala, A. O. Frank, M. J. Hesse, D. Dankova, J.-G. Song, M. Bruce-Smythe, H. Struble, F. J. Garcia, S. M. Brittain, A. C. Kile, L. M. McGregor, J. M. McKenna, J. A. Tallarico, M. Schirle, D. K. Nomura, *ACS Central Science* **2023**, *9*, 915-926; b.) G. Dong, Y. Ding, S. He, C. Sheng, *Journal of Medicinal Chemistry* **2021**, *64*, 10606-10620.
- [38] L. I. Calderon-Villalobos, X. Tan, N. Zheng, M. Estelle, *Cold Spring Harb Perspect Biol* **2010**, *2*, a005546.
- [39] Y. Isobe, M. Okumura, L. M. McGregor, S. M. Brittain, M. D. Jones, X. Liang, R. White, W. Forrester, J. M. McKenna, J. A. Tallarico, M. Schirle, T. J. Maimone, D. K. Nomura, *Nature Chemical Biology* **2020**, *16*, 1189-1198.
- [40] E. S. Ali, K. Mitra, S. Akter, S. Ramproshad, B. Mondal, I. N. Khan, M. T. Islam, J. Sharifi-Rad, D. Calina, W. C. Cho, *Cancer Cell International* **2022**, *22*, 284.
- [41] J. Choi, J. Chen, S. L. Schreiber, J. Clardy, *Science* **1996**, *273*, 239-242.
- [42] a.) P. A. Horton, F. E. Koehn, R. E. Longley, O. J. McConnell, *Journal of the American Chemical Society* **1994**, *116*, 6015-6016; b.) A. E. Wright, Y. Chen, P. L. Winder, T. P. Pitts, S. A. Pomponi, R. E. Longley, *Journal of Natural Products* **2004**, *67*, 1351-1355.
- [43] R. Dubey, C. E. Stivala, H. Q. Nguyen, Y.-H. Goo, A. Paul, J. E. Carette, B. M. Trost, R. Rohatgi, *Nature Chemical Biology* **2020**, *16*, 206-213.
- [44] G. B. D. A. R. Collaborators, *Lancet* **2022**, *400*, 2221-2248.
- [45] M. Kolář, K. Urbánek, T. Látal, *International Journal of Antimicrobial Agents* **2001**, *17*, 357-363.
- [46] J. M. A. Blair, M. A. Webber, A. J. Baylay, D. O. Ogbolu, L. J. V. Piddock, *Nature Reviews Microbiology* **2015**, *13*, 42-51.
- [47] C. Antimicrobial Resistance, *Lancet* **2022**, *399*, 629-655.
- [48] J. O'Neill, **2014**.
- [49] M. A. Cook, G. D. Wright, *Science Translational Medicine* **2022**, *14*, eabo7793.
- [50] A. Teillant, S. Gandra, D. Barter, D. J. Morgan, R. Laxminarayan, *The Lancet Infectious Diseases* **2015**, *15*, 1429-1437.

## References

- [51] M. Singer, C. S. Deutschman, C. W. Seymour, M. Shankar-Hari, D. Annane, M. Bauer, R. Bellomo, G. R. Bernard, J. D. Chiche, C. M. Coopersmith, R. S. Hotchkiss, M. M. Levy, J. C. Marshall, G. S. Martin, S. M. Opal, G. D. Rubenfeld, T. van der Poll, J. L. Vincent, D. C. Angus, *JAMA* **2016**, *315*, 801-810.
- [52] K. E. Rudd, S. C. Johnson, K. M. Agesa, K. A. Shackelford, D. Tsoi, D. R. Kievlan, D. V. Colombara, K. S. Ikuta, N. Kissoon, S. Finfer, C. Fleischmann-Struzek, F. R. Machado, K. K. Reinhart, K. Rowan, C. W. Seymour, R. S. Watson, T. E. West, F. Marinho, S. I. Hay, R. Lozano, A. D. Lopez, D. C. Angus, C. J. L. Murray, M. Naghavi, *Lancet* **2020**, *395*, 200-211.
- [53] S. Narayana Iyengar, J. Dietvorst, A. Ferrer-Vilanova, G. Guirado, X. Muñoz-Berbel, A. Russom, *ACS Sensors* **2021**, *6*, 3357-3366.
- [54] R. S. Hotchkiss, L. L. Moldawer, S. M. Opal, K. Reinhart, I. R. Turnbull, J.-L. Vincent, *Nature Reviews Disease Primers* **2016**, *2*, 16045.
- [55] B. M. Peters, M. A. Jabra-Rizk, G. A. O'May, J. W. Costerton, M. E. Shirtliff, *Clin Microbiol Rev* **2012**, *25*, 193-213.
- [56] M. Jamal, W. Ahmad, S. Andleeb, F. Jalil, M. Imran, M. A. Nawaz, T. Hussain, M. Ali, M. Rafiq, M. A. Kamil, *Journal of the Chinese Medical Association* **2018**, *81*, 7-11.
- [57] H.-C. Flemming, J. Wingender, U. Szewzyk, P. Steinberg, S. A. Rice, S. Kjelleberg, *Nature Reviews Microbiology* **2016**, *14*, 563-575.
- [58] H.-C. Flemming, J. Wingender, *Nature Reviews Microbiology* **2010**, *8*, 623-633.
- [59] a.) O. Ciofu, E. Rojo-Moliner, M. D. Macià, A. Oliver, *APMIS* **2017**, *125*, 304-319; b.) O. Ciofu, C. Moser, P. Ø. Jensen, N. Høiby, *Nature Reviews Microbiology* **2022**, *20*, 621-635.
- [60] C. R. Arciola, D. Campoccia, L. Montanaro, *Nature Reviews Microbiology* **2018**, *16*, 397-409.
- [61] a.) J. R. Lentino, *Clinical Infectious Diseases* **2003**, *36*, 1157-1161; b.) W. B. Dale, M. H. Peter, f. t. S. I. P. G. W. Workgroup, *Clinical Infectious Diseases* **2004**, *38*, 1706-1715; c.) C. L. Romanò, S. Scarponi, E. Gallazzi, D. Romanò, L. Drago, *Journal of Orthopaedic Surgery and Research* **2015**, *10*, 157.
- [62] S. E. Rossiter, M. H. Fletcher, W. M. Wuest, *Chemical Reviews* **2017**, *117*, 12415-12474.
- [63] E. Patridge, P. Gareiss, M. S. Kinch, D. Hoyer, *Drug Discovery Today* **2016**, *21*, 204-207.
- [64] M. G. Watve, R. Tickoo, M. M. Jog, B. D. Bhole, *Archives of Microbiology* **2001**, *176*, 386-390.
- [65] R. E. de Lima Procópio, I. R. da Silva, M. K. Martins, J. L. de Azevedo, J. M. de Araújo, *The Brazilian Journal of Infectious Diseases* **2012**, *16*, 466-471.
- [66] A. Schatz, E. Bugle, S. A. Waksman, *Proceedings of the Society for Experimental Biology and Medicine* **1944**, *55*, 66-69.
- [67] K. B. Gromadski, M. V. Rodnina, *Nature Structural & Molecular Biology* **2004**, *11*, 316-322.
- [68] C. Watanakunakorn, *Journal of Antimicrobial Chemotherapy* **1984**, *14*, 7-18.
- [69] R. S. Griffith, *Journal of Antimicrobial Chemotherapy* **1984**, *14*, 1-5.
- [70] L. L. Ling, T. Schneider, A. J. Peoples, A. L. Spoering, I. Engels, B. P. Conlon, A. Mueller, T. F. Schäberle, D. E. Hughes, S. Epstein, M. Jones, L. Lazarides, V. A. Steadman, D. R. Cohen, C. R. Felix, K. A. Fetterman, W. P. Millett, A. G. Nitti, A. M. Zullo, C. Chen, K. Lewis, *Nature* **2015**, *517*, 455-459.
- [71] G. HÖGENAUER, *European Journal of Biochemistry* **1975**, *52*, 93-98.
- [72] S. A. Vichkanova, O. N. Tolkachev, R. G. Martynova, E. V. Arzamastsev, *Pharmaceutical Chemistry Journal* **1982**, *16*, 925-929.
- [73] a.) J. Grembecka, S. He, A. Shi, T. Purohit, A. G. Muntean, R. J. Sorenson, H. D. Showalter, M. J. Murai, A. M. Belcher, T. Hartley, J. L. Hess, T. Cierpicki, *Nature Chemical Biology* **2012**, *8*, 277-284; b.) R. E. Phillips, Y. Yang, R. C. Smith, B. M. Thompson, T. Yamasaki, Y. M. Soto-Feliciano, K. Funato, Y. Liang, J. Garcia-Bermudez, X. Wang, B. A. Garcia, K. Yamasaki, J. G. McDonald, K. Birsoy, V. Tabar, C. D. Allis, *Proceedings of the National Academy of Sciences* **2019**, *116*, 7957-7962.
- [74] a.) B. J. Leslie, P. J. Hergenrother, *Chemical Society Reviews* **2008**, *37*, 1347-1360; b.) Y. Tabana, D. Babu, R. Fahlman, A. G. Siraki, K. Barakat, *BMC Biotechnology* **2023**, *23*, 44.

## References

- [75] S. Lechner, R. R. Steimbach, L. Wang, M. L. Deline, Y.-C. Chang, T. Fromme, M. Klingenspor, P. Matthias, A. K. Miller, G. Médard, B. Kuster, *Nature Communications* **2023**, *14*, 3548.
- [76] F. del Gaudio, F. Pollastro, M. Mozzicafreddo, R. Riccio, A. Minassi, M. C. Monti, *Chemical Communications* **2018**, *54*, 12863-12866.
- [77] M. P. Gotsbacher, S. Cho, H. J. Kwon, P. Karuso, *Proteome Science* **2017**, *15*, 16.
- [78] E. Smith, I. Collins, *Future Medicinal Chemistry* **2015**, *7*, 159-183.
- [79] a.) L. P. Conway, A. M. Jadhav, R. A. Homan, W. Li, J. S. Rubiano, R. Hawkins, R. M. Lawrence, C. G. Parker, *Chemical Science* **2021**, *12*, 7839-7847; b.) Z. Li, P. Hao, L. Li, C. Y. J. Tan, X. Cheng, G. Y. J. Chen, S. K. Sze, H.-M. Shen, S. Q. Yao, *Angewandte Chemie International Edition* **2013**, *52*, 8551-8556; c.) C. G. Parker, M. R. Pratt, *Cell* **2020**, *180*, 605-632.
- [80] J. Ha, H. Park, J. Park, S. B. Park, *Cell Chemical Biology* **2021**, *28*, 394-423.
- [81] a.) S. A. Chambers, S. D. Townsend, *Carbohydrate Research* **2020**, *488*, 107895; b.) T. Kambe, B. E. Correia, M. J. Niphakis, B. F. Cravatt, *Journal of the American Chemical Society* **2014**, *136*, 10777-10782; c.) C.-F. Chang, A. Mfuh, J. Gao, H.-Y. Wu, C. M. Woo, *Tetrahedron* **2018**, *74*, 3273-3277; dA. V. West, Y. Amako, C. M. Woo, *Journal of the American Chemical Society* **2022**, *144*, 21174-21183.
- [82] P. Le, E. Kunold, R. Maccsics, K. Rox, M. C. Jennings, I. Ugur, M. Reinecke, D. Chaves-Moreno, M. W. Hackl, C. Fetzer, F. A. M. Mandl, J. Lehmann, V. S. Korotkov, S. M. Hacker, B. Kuster, I. Antes, D. H. Pieper, M. Rohde, W. M. Wuest, E. Medina, S. A. Sieber, *Nature Chemistry* **2020**, *12*, 145-158.
- [83] B. X. Li, J. Chen, B. Chao, L. L. David, X. Xiao, *ACS Chemical Biology* **2018**, *13*, 1380-1387.
- [84] X. Chen, M. Li, M. Li, D. Wang, J. Zhang, *Chemical Communications* **2021**, *57*, 3139-3142.
- [85] a.) P. Kleiner, W. Heydenreuter, M. Stahl, V. S. Korotkov, S. A. Sieber, *Angewandte Chemie International Edition* **2017**, *56*, 1396-1401; b.) H. Park, J. Y. Koo, Y. V. V. Srikanth, S. Oh, J. Lee, J. Park, S. B. Park, *Chemical Communications* **2016**, *52*, 5828-5831.
- [86] C. M. Pichler, J. Krysiak, R. Breinbauer, *Bioorganic & Medicinal Chemistry* **2016**, *24*, 3291-3303.
- [87] K. A. Kalesh, J. A. Clulow, E. W. Tate, *Chemical Communications* **2015**, *51*, 5497-5500.
- [88] Z. Huang, D. Ogasawara, U. I. Seneviratne, A. B. Cognetta, III, C. W. am Ende, D. M. Nason, K. Lapham, J. Litchfield, D. S. Johnson, B. F. Cravatt, *ACS Chemical Biology* **2019**, *14*, 192-197.
- [89] J. Lehmann, J. Vomacka, K. Esser, M. Nodwell, K. Kolbe, P. Rämer, U. Protzer, N. Reiling, S. A. Sieber, *MedChemComm* **2016**, *7*, 1797-1801.
- [90] a.) J. C. BISCHOF, X. HE, *Annals of the New York Academy of Sciences* **2006**, *1066*, 12-33; b.) M. Redhead, R. Satchell, C. McCarthy, S. Pollack, J. Unitt, *Biochemistry* **2017**, *56*, 6187-6199.
- [91] a.) J. A. Schellman, *Biopolymers* **1975**, *14*, 999-1018; b.) M. S. Celej, G. G. Montich, G. D. Fidelio, *Protein Science* **2003**, *12*, 1496-1506; c.) M. Vedadi, F. H. Niesen, A. Allali-Hassani, O. Y. Fedorov, P. J. Finerty, G. A. Wasney, R. Yeung, C. Arrowsmith, L. J. Ball, H. Berglund, R. Hui, B. D. Marsden, P. Nordlund, M. Sundstrom, J. Weigelt, A. M. Edwards, *Proceedings of the National Academy of Sciences* **2006**, *103*, 15835-15840.
- [92] *ASSAY and Drug Development Technologies* **2012**, *10*, 128-136.
- [93] a.) D. M. Molina, R. Jafari, M. Ignatushchenko, T. Seki, E. A. Larsson, C. Dan, L. Sreekumar, Y. Cao, P. Nordlund, *Science* **2013**, *341*, 84-87; b.) R. Jafari, H. Almqvist, H. Axelsson, M. Ignatushchenko, T. Lundbäck, P. Nordlund, D. M. Molina, *Nature Protocols* **2014**, *9*, 2100-2122.
- [94] M. M. Savitski, N. Zinn, M. Faeltsh-Savitski, D. Poeckel, S. Gade, I. Becher, M. Muelbaier, A. J. Wagner, K. Strohmmer, T. Werner, S. Melchert, M. Petretich, A. Rutkowska, J. Vappiani, H. Franken, M. Steidel, G. M. Sweetman, O. Gilan, E. Y. N. Lam, M. A. Dawson, R. K. Prinjha, P. Grandi, G. Bergamini, M. Bantscheff, *Cell* **2018**, *173*, 260-274.e225.
- [95] H. Franken, T. Mathieson, D. Childs, G. M. A. Sweetman, T. Werner, I. Tögel, C. Doce, S. Gade, M. Bantscheff, G. Drewes, F. B. M. Reinhard, W. Huber, M. M. Savitski, *Nature Protocols* **2015**, *10*, 1567-1593.
- [96] V. C. Kirsch, C. Orgler, S. Braig, I. Jeremias, D. Auerbach, R. Müller, A. M. Vollmar, S. A. Sieber, *Angewandte Chemie International Edition* **2020**, *59*, 1595-1600.

## References

---

- [97] A. L. Herneisen, S. M. Sidik, B. M. Markus, D. H. Drewry, W. J. Zuercher, S. Lourido, *ACS Chemical Biology* **2020**, *15*, 1801-1807.
- [98] E. Dehghan, M. Goodarzi, B. Saremi, R. Lin, H. Mirzaei, *Nature Communications* **2019**, *10*, 4905.
- [99] X. Zhang, Q. Wang, Y. Li, C. Ruan, S. Wang, L. Hu, M. Ye, *Analytical Chemistry* **2020**, *92*, 1363-1371.
- [100] a.) J. G. Van Vranken, J. Li, D. C. Mitchell, J. Navarrete-Perea, S. P. Gygi, *eLife* **2021**, *10*, e70784; b.) C. Yu, X. Chen, W. Xu, S. Li, Q. Chai, Y. Zhang, *PROTEOMICS* **2023**, *23*, 2200281.
- [101] a.) H. Taniuchi, L. Morávek, C. B. Anfinsen, *Journal of Biological Chemistry* **1969**, *244*, 4600-4606; b.) G. Markus, D. K. McClintock, B. A. Castellani, *Journal of Biological Chemistry* **1967**, *242*, 4402-4408; c.) C. Park, S. Marqusee, *Nature Methods* **2005**, *2*, 207-212.
- [102] L. Dai, Z. Li, D. Chen, L. Jia, J. Guo, T. Zhao, P. Nordlund, *Pharmacology & Therapeutics* **2020**, *216*, 107690.
- [103] F. Wang, S. Zhou, D. Qi, S.-H. Xiang, E. T. Wong, X. Wang, E. Fonkem, T.-c. Hsieh, J. Yang, B. Kirmani, J. B. Shabb, J. M. Wu, M. Wu, J. H. Huang, W.-H. Yu, E. Wu, *Journal of the American Chemical Society* **2019**, *141*, 3613-3622.
- [104] D. Benjamin, M. Colombi, S. K. Hindupur, C. Betz, H. A. Lane, M. Y. M. El-Shemerly, M. Lu, L. Quagliata, L. Terracciano, S. Moes, T. Sharpe, A. Wodnar-Filipowicz, C. Moroni, M. N. Hall, *Science Advances* **2016**, *2*, e1601756.
- [105] N. Wang, Q. Wang, H. Tang, F. Zhang, Y. Zheng, S. Wang, J. Zhang, Z. Wang, X. Xie, *Journal of Experimental & Clinical Cancer Research* **2017**, *36*, 172.
- [106] I. Hübner, J. A. Shapiro, J. Hoßmann, J. Drechsel, S. M. Hacker, P. N. Rather, D. H. Pieper, W. M. Wuest, S. A. Sieber, *ACS Central Science* **2021**, *7*, 488-498.
- [107] T. M. Kapoor, R. M. Miller, *Trends in Pharmacological Sciences* **2017**, *38*, 1100-1109.
- [108] F. Teraishi, S. Wu, L. Zhang, W. Guo, J. J. Davis, F. Dong, B. Fang, *Cancer Res* **2005**, *65*, 6380-6387.
- [109] S. A. Wacker, B. R. Houghtaling, O. Elemento, T. M. Kapoor, *Nature Chemical Biology* **2012**, *8*, 235-237.
- [110] C. Kasap, O. Elemento, T. M. Kapoor, *Nature Chemical Biology* **2014**, *10*, 626-628.
- [111] P. Svoboda, *Frontiers in Plant Science* **2020**, *11*.
- [112] U. S. Eggert, A. A. Kiger, C. Richter, Z. E. Perlman, N. Perrimon, T. J. Mitchison, C. M. Field, *PLOS Biology* **2004**, *2*, e379.
- [113] G. C. Terstappen, C. Schlüpen, R. Raggiaschi, G. Gaviraghi, *Nature Reviews Drug Discovery* **2007**, *6*, 891-903.
- [114] J. S. Shim, J. Lee, H.-J. Park, S.-J. Park, H. J. Kwon, *Chemistry & Biology* **2004**, *11*, 1455-1463.
- [115] D. Sydow, L. Burggraaff, A. Szengel, H. W. T. van Vlijmen, A. P. Ijzerman, G. J. P. van Westen, A. Volkamer, *Journal of Chemical Information and Modeling* **2019**, *59*, 1728-1742.
- [116] G. Mugumbate, K. A. Abrahams, J. A. G. Cox, G. Papadatos, G. van Westen, J. Lelièvre, S. T. Calus, N. J. Loman, L. Ballell, D. Barros, J. P. Overington, G. S. Besra, *PLOS ONE* **2015**, *10*, e0121492.
- [117] F. Chen, Z. Wang, C. Wang, Q. Xu, J. Liang, X. Xu, J. Yang, C. Wang, T. Jiang, R. Yu, *Journal of Molecular Graphics and Modelling* **2017**, *77*, 372-377.
- [118] J. Gong, P. Sun, N. Jiang, R. Riccio, G. Lauro, G. Bifulco, T.-J. Li, W. H. Gerwick, W. Zhang, *Organic Letters* **2014**, *16*, 2224-2227.
- [119] G. Lauro, M. Masullo, S. Piacente, R. Riccio, G. Bifulco, *Bioorganic & Medicinal Chemistry* **2012**, *20*, 3596-3602.



## **Part II**

### Research



## 6.

# A Pd-labile fluoroquinolone prodrug efficiently prevents biofilm formation on coated surfaces

---

This chapter is based on:

**J. Braun**, M. C. Ortega-Liebana, A. Unciti-Broceta, S. A. Sieber, „A Pd-labile fluoroquinolone prodrug efficiently prevents biofilm formation on coated surfaces,” *Org. Biomol. Chem.*, **2024**, 22, 1998–2002.

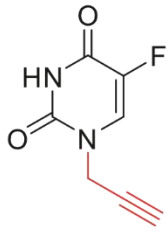
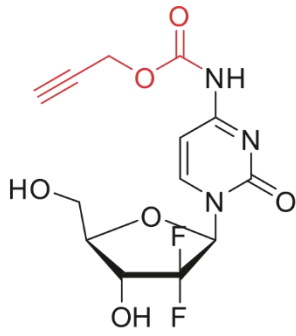
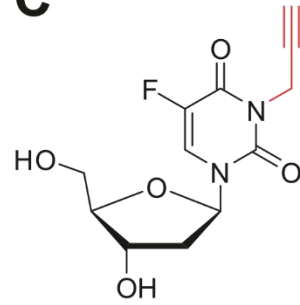
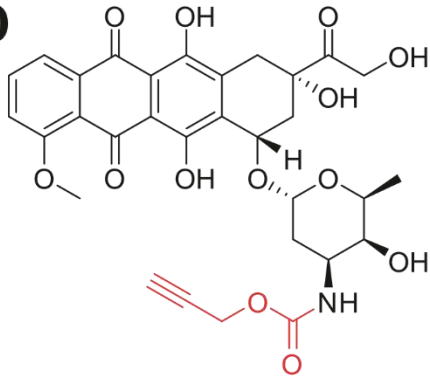
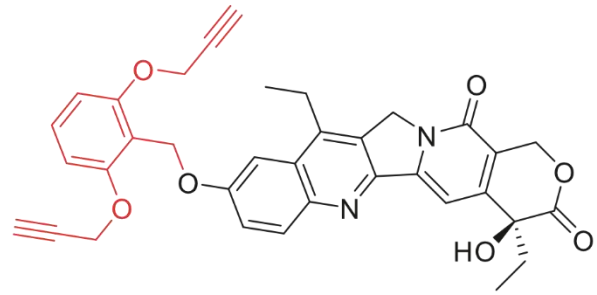
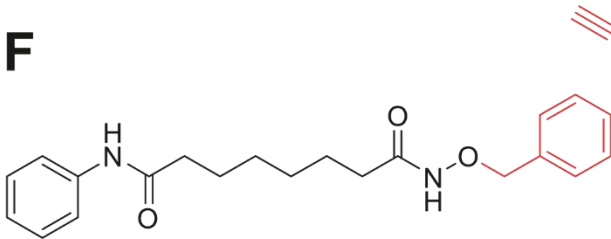
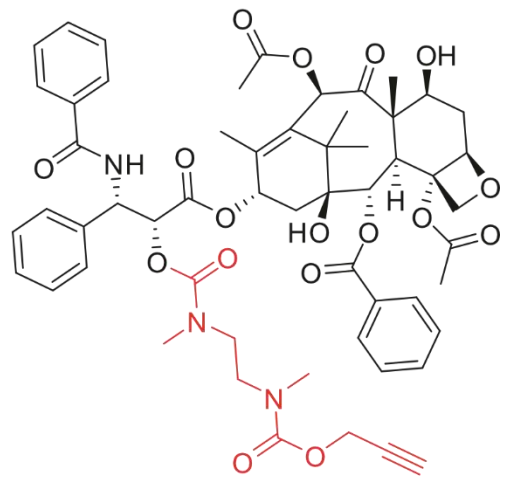
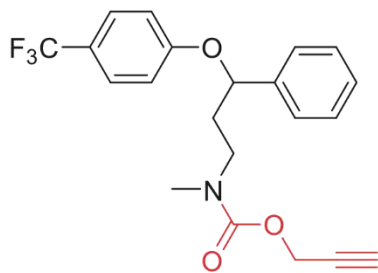
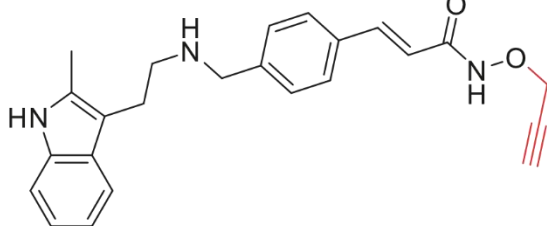
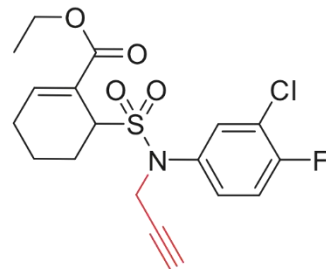
<https://doi.org/10.1039/D4OB00014E>

### Author Contributions

Josef Braun and Stephan A. Sieber conceived the project. M. Carmen Ortega-Liebana and Asier Unciti-Broceta developed the nanosheets. M. Carmen Ortega-Liebana synthesized the nanosheets and characterized them. Josef Braun designed the prodrugs, synthesized them, and characterized them for antibacterial activity and cell toxicity. He tested the nanosheets for activity and anti-biofilm activity.

## 6.1 Metal-labile prodrugs

Bioorthogonal organometallic reactions are a relatively new addition to the chemical biology toolbox. In 2010, Streu and Meggers reported cleavage of allyl carbamates with a ruthenium catalyst.<sup>[120]</sup> Li *et al.* reported in 2011 the functionalization of alkyne-encoded proteins in aqueous medium and bacterial cells via a copper-free sonogashira cross-coupling.<sup>[121]</sup> Further, Michel *et al.* utilized palladium-mediated carbonylation to build a reaction-based fluorescent probe to monitor carbon monoxide in living cells. They could show that the CO levels in HEK293T cells can be monitored using this probe.<sup>[122]</sup> A Suzuki-Miyaura coupling of genetically encoded unnatural aryl halide-containing amino acids with boronic acid-containing fluorophores was used by Spicer *et al.* for site-selective cell-surface labeling.<sup>[123]</sup> It was shown that bioorthogonal organometallic chemistry can not only be applied for research purposes but also for medical applications. 5-Fluorouracil is an antimetabolite drug used to treat cancer.<sup>[124]</sup> Due to its unspecific mechanism, it affects not only cancer cells but also healthy cells, causing severe side effects. It would be desirable to have active 5-fluorouracil only in the cancer tissue. Weiss *et al.* achieved this using bioorthogonal organometallic chemistry. They developed a novel prodrug strategy for 5-fluorouracil using a Pd-labile, propargylated derivative. A Pd<sup>0</sup>-loaded resin was used by them, which they injected into the tumor, to release free 5-fluorouracil (Figure 24A).<sup>[125]</sup> This strategy was later also used for other cancer drugs like gemcitabine, floxuridine, doxorubicin, the active metabolite of irinotecan, and the HDAC inhibitor vorinostat (Figure 24B-F).<sup>[126]</sup> Furthermore, Pd-loaded titanium devices and cancer-derived exosomes loaded with ultrathin palladium nanosheets were developed as alternative bioorthogonal catalysts for activating the prodrugs.<sup>[127]</sup> Pèrez *et al.* used hydrogels loaded with Pd-nanosheets to uncage a Pd-labile prodrug of paclitaxel (Figure 24G).<sup>[128]</sup> Besides Pd-catalysis the group of Unciti-Broceta also employed gold catalysis to activate their prodrugs. They applied a catalytic Au-polymer composite to activate the anxiolytic drug fluoxetine in the central nervous system of zebrafish (Figure 24H).<sup>[129]</sup> This group also employed Au-catalysis to activate a propargylated derivative of the potent HDAC inhibitor panobinostat (Figure 24I).<sup>[130]</sup> Encapsulated nanoparticles made of an AuPd-nano alloy showed great promise as they displayed superior catalytic properties and tolerability. Upon nanoencapsulation, the AuPd nanoparticles are able to uncage paclitaxel intracellularly.<sup>[131]</sup> Plunk *et al.* used Pd<sup>0</sup>-nanoparticles immobilized on TentaGel resins to activate Pd-labile derivatives of toll-like receptor 4 (TLR4) inhibitor Tak-242 and locally combat inflammation (Figure 24J).<sup>[132]</sup>

**A****5-Fluorouracil****B****Gemcitabine****C****Floxuridine****D****Doxorubicin****E****SN-38****F****Vorinostat****G****Paclitaxel****H****Fluoxetine****I****Panobinostat****J****Tak-242**

**Figure 24.** Structure of prodrugs that can be activated by organometallic chemistry. Metal-labile groups are depicted in red. (A) 5-fluorouracil, (B) gemcitabine, (C) floxuridine, (D) doxorubicin, (E) SN-38, (F) vorinostat, (G) paclitaxel, (H) fluoxetine, (I) panobinostat, (J) Tak-242.

## 6.2 Aim and significance of the project

The formation of bacterial biofilms on biomedical implants such as catheters and prosthetics poses a significant challenge. Device-associated infections represent 25.6% of all healthcare-associated infections in the US.<sup>[133]</sup> The formation of biofilms can lead to chronic and recurrent infections. Due to their high antibiotic tolerance, biofilms are difficult to treat, and implant removal and debridement are often necessary, which increases patient suffering and healthcare costs.<sup>[134]</sup> Ciprofloxacin or other fluoroquinolones are frequently used for the prevention of biofilms.<sup>[59a, 135]</sup> However, they can cause serious side effects such as tendinopathy and tendon rupture and, like all antibiotics, affect the gut microbiome.<sup>[136]</sup> Most clinically relevant biofilms are formed by *Staphylococcus aureus*.<sup>[137]</sup> This project aimed to develop a coating that actively prevents the formation of bacterial biofilms on biomedical implants, reduces exposure to active antibiotics, and limits the effect on the gut microbiome by utilizing a bioorganic organometallic prodrug strategy. Therefore, a metallic catalyst is needed, as well as prodrugs of antibiotics that can be activated by the catalyst and a biocompatible coating for the implant that can embed the catalyst and keep it in place.

## 6.3 Results and Discussion

### 6.3.1 Design and synthesis of the prodrugs

To test if this strategy is suitable for the prevention of biofilm formation, fluoroquinolones ciprofloxacin and moxifloxacin were selected. Usually, they are used at high concentrations to treat biofilms and are known to exhibit side effects.<sup>[138]</sup> Ciprofloxacin was derivatized with an alkyne group either directly at the carbonic acid or via a self-immolative linker at its secondary amino position, yielding prodrugs Cipro-Pro 1 and Cipro-Pro 2 (Figure 25A). Furthermore, moxifloxacin was modified with an alkyne group at its secondary amino-group via a self-immolative linker resulting in prodrug Moxi-Pro 1 (Figure 25B).

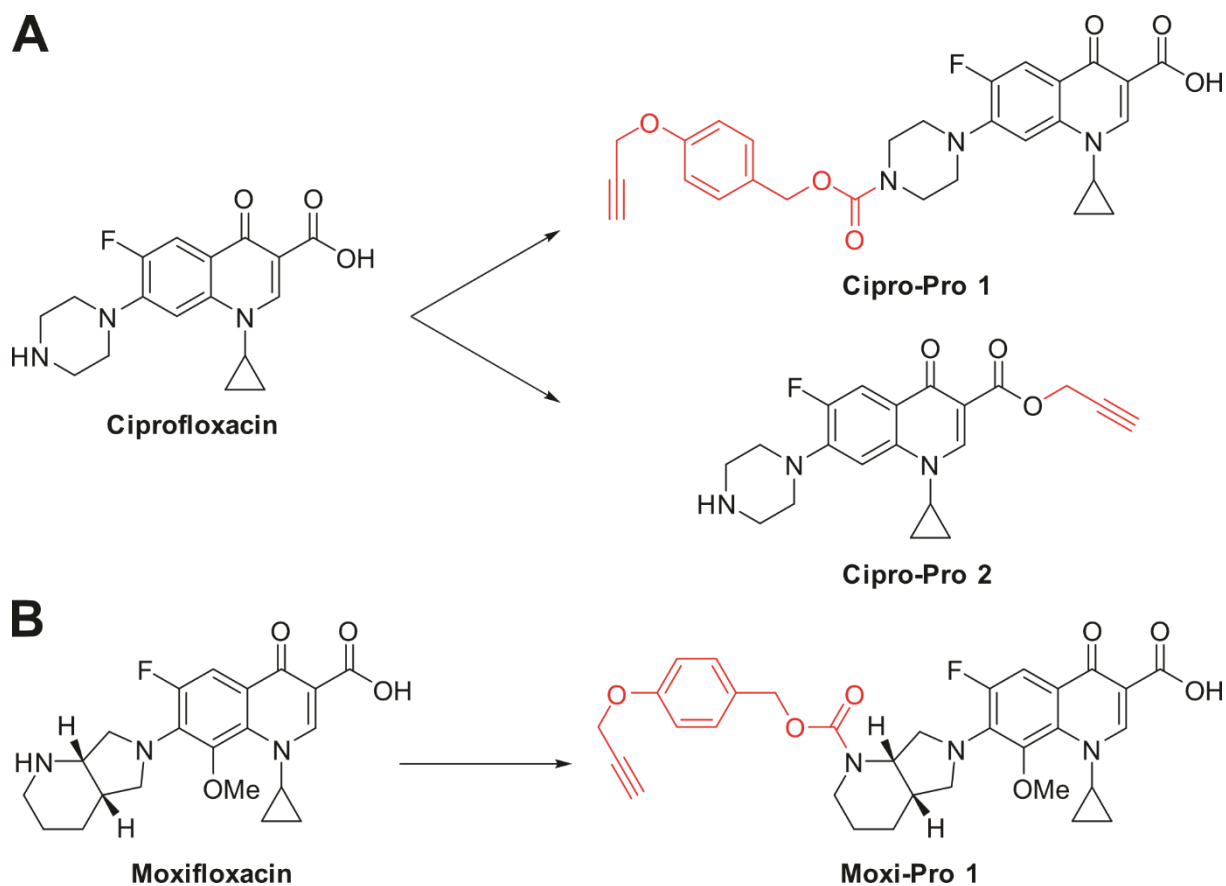


**Figure 25.** Structure of the parent antibiotics and the prodrugs. Metal-labile groups are depicted in red. (A) Structure of ciprofloxacin and the prodrugs Cipro-Pro 1 and Cipro-Pro 2, (B) Structure of moxifloxacin and the prodrug Moxi-Pro 1.

### 6.3.2 Biological characterization of the prodrugs

To determine if the introduction of the metal-labile groups resulted in the desired loss in antimicrobial activity, the minimal inhibitory concentration (MIC) of the prodrugs and their parent antibiotics was determined. Compared to their parent antibiotics, prodrugs Cipro-Pro 2 and Moxi-Pro 1 showed no pronounced antibiotic activity against *S. aureus* SA113 and *E. coli* UT189. *N*-terminally modified ciprofloxacin (Cipro-Pro 1) retained most of the antibiotic activity and was thus disregarded for further studies (Table 1). To test the ability of the prodrugs to inhibit the formation of bacterial biofilms, their minimal biofilm inhibitory concentration (MBIC) was determined. Following the trend of the MIC results, the MBIC against *S. aureus* SA113 was significantly higher for the prodrugs, with 8- to over 60-fold reduced potency for Cipro-Pro 2 and Moxi-Pro 1 (Table 1). Using the MTT assay, the metabolic activity was determined to see if the prodrugs affect cell viability. Treatment of HepG2 cells with the prodrugs did not affect their metabolic activity, indicating that none of the prodrugs is acutely cell toxic (Figure S1). Due to their reduced antibacterial activity and cell compatibility, the prodrugs Cipro-Pro 2 and Moxi-Pro 1 were progressed to the project's next stage.

**Table 1.** Minimal (biofilm) inhibitory concentrations of the prodrugs.

	MIC [ $\mu\text{M}$ ]	MIC [ $\mu\text{M}$ ]	MBIC [ $\mu\text{M}$ ]
	<i>E. coli</i> UTI89	<i>S. aureus</i> SA113	<i>S. aureus</i> SA113
Ciprofloxacin	0.03	0.63	1.25
Cipro-Pro 1	0.03	0.63	-
Cipro-Pro 2	1.25	10.0	10.0
Moxifloxacin	0.16	0.16	0.16
Moxi-Pro 1	> 10	> 10	> 10

### 6.3.3 Antibacterial activity of the nanosheets

Pd nanosheets (PdNS) of two different sizes (PdNS-90: 17.4 nm, PdNS-170: 9.1 nm) were provided by M. C. Ortega-Liebana (Unciti-Broceta lab, Edinburgh). The nanosheets were tested for their ability to prevent *S. aureus* SA113 biofilms. Satisfyingly, low concentrations of the nanosheets did not affect biofilm formation, but higher concentrations (50–100  $\mu\text{g/ml}$ ) reduced biofilm formation (Figure S2).

### 6.3.4 Cell-free prodrug-into-drug conversion

A propargyl-modified reporter molecule (*O*-propargyl-4-methylumbelliferone)<sup>[139]</sup> was used to compare the catalytic activities of the different nanosheets. Upon *O*-propargyl cleavage, it releases powerfully fluorescent 7-hydroxy-4-methylcoumarin (Figure 26A). The reactions were performed under physiological conditions in PBS (pH = 7.4, isotonicity) at 37 °C. The activity of PdNS-90 and PdNS-170 was tested by monitoring fluorescence over time. Both nanosheets reached about 30% release within 4 h (Figure 26B).

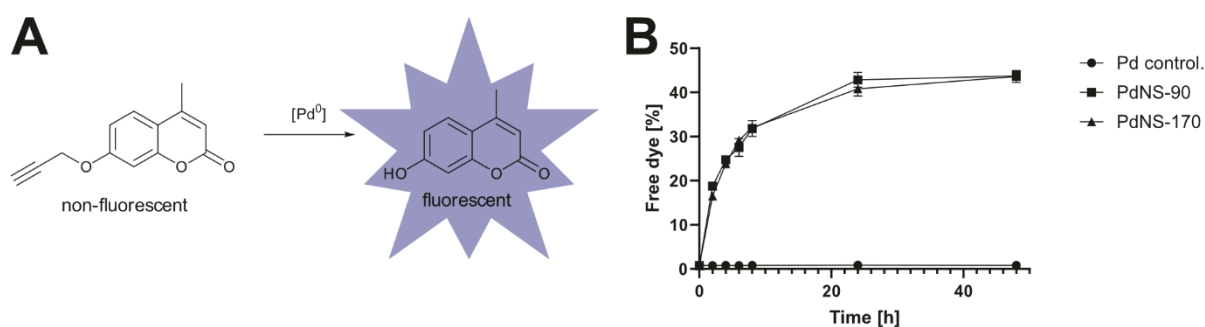


**Figure 26.** Cell-free prodrug into drug conversion. (A) The fluorogenic assay used to quantify PdNS activity, (B) Comparison of the catalytic activities of the different PdNS as determined with the fluorogenic assay (100  $\mu\text{M}$  pro-coumarin, 5  $\mu\text{g/ml}$  PdNS). The conversion values were calculated from fluorescence intensity measurements at  $\lambda_{\text{ex/em}} = 350/450$  nm using a standard curve of the fluorescence intensity of the coumarin. Negative controls: pro-coumarin without nanocatalysts. Error bars:  $\pm\text{SD}$  from  $n = 3$ .

Upon adding mouse 20% serum, the release activity was still effective, albeit with reduced kinetics and cleavage of about 20% within 4 h (Figure S3). Mass-spectrometry (MS) was used to monitor the cleavage of the prodrugs Cipro-Pro 2 and Moxi-Pro 1. The prodrugs were incubated in PBS (pH = 7.4, isotonicity) at 37 °C and analysis of the reaction mixtures by MS after 1 h revealed about 50% of Cipro-Pro 2 and 70% of Moxi-Pro 1 consumption and formation of mass peaks corresponding to the parent antibiotics at the same time (Figure S4, and S5).

### 6.3.5 Prevention of biofilms

Due to their proven track record in drug delivery, agarose hydrogels were chosen as carriers for the Pd nanosheets.<sup>[140]</sup> Since both nanosheets exhibited almost identical catalytic activity, PdNS-90 were selected for the studies on biofilm prevention. Their larger particle size promised a more stable incorporation into the agarose hydrogel matrix. Either 1 or 2 mm thick agarose hydrogels (20 mg/ml) were loaded with different concentrations of Pd nanosheets (5–50 µg/ml) and incubated with the prodrugs Cipro-Pro 2 or Moxi-Pro 1 (5 µM in CASO Medium) for 0–8 h before to the medium was inoculated with *S. aureus* SA113. CellTiter-Blue™ (Promega) was used to monitor biofilm formation after 24 h (Figures S6 and S7). The ciprofloxacin prodrug Cipro-Pro 2 did not completely inhibit the formation of biofilms even at the highest Pd nanosheet loading (50 µg/ml) and the longest tested preincubation (8 h). The moxifloxacin prodrug Moxi-Pro 1 prevented biofilm formation at the highest Pd nanosheet loading (50 µg/ml), even without preincubation (Figure 27A). Increasing the incubation time of Moxi-Pro 1 to 1 h allowed to reduce the concentration of Pd-nanosheets in the hydrogel required for abolishing biofilm formation to 25 µg/ml (Figure 27B). The incubation with prodrugs or hydrogels loaded with 50 µg/ml Pd nanosheets alone resulted in a minor reduction in biofilm formation (Figures S6 and S7). An increase in the hydrogel thickness from 1 mm to 2 mm did not influence the overall performance (Figure 27C).

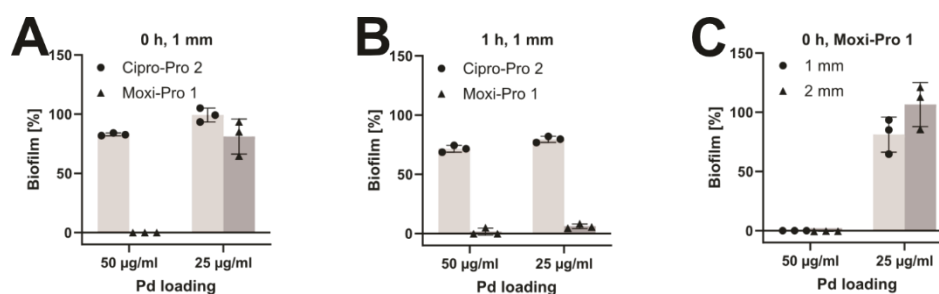


**Figure 27.** *In vitro* prevention of biofilms formation. (A) Anti-biofilm activity of Cipro-Pro 2 and Moxi-Pro 1 at different Pd-loadings (5 µM prodrug, no preincubation), (B) Anti-biofilm activity of Cipro-Pro 2 and Moxi-Pro 1 at different Pd-loadings (5 µM prodrug, 1 h preincubation), (C) Independence of the activation of Moxi-Pro 1 of hydrogel thickness (5 µM prodrug, no preincubation). Error bars: ±SD from n = 3. Full dataset in Figures S6 and S7.

These experiments indicate that moxifloxacin prodrug Moxi-Pro 1 and 50 µg/ml loaded hydrogels of 1 mm thickness are the optimal coating for implants to prevent the formation of biofilms on their surface. The long-term stability of the coating's catalytic activity was tested by

incubating hydrogels loaded with PdNS-90 for several weeks with PBS (pH = 7.4, isotonicity) and replacing the PBS weekly before the activity was visualized with the fluorogenic assay. The catalytic activity declined steadily over the 7 weeks, but the nanosheets still displayed 50% of their original catalytic activity after 7 weeks (Figure S8). However, when the medium with prodrug and bacteria was exchanged daily instead of PBS weekly, biofilm formation on the surface could be seen on the third day. It must be remembered that PBS and bacterial growth medium (CASO) both are representatives of extreme, non-physiological conditions. The actual situation in a patient's body lies somewhere in between these extremes. To study this technology in a system closer resembling the situation in a patient animal models of implant-associated infections could be used.

#### 6.4 Summary and conclusion

This work developed a hydrogel-coating loaded with Pd-nanosheets, which catalyze the activation of Pd-labile prodrugs to prevent bacterial biofilm formation on implants. Three different Pd-labile prodrugs of the fluoroquinolone antibiotics, ciprofloxacin, and moxifloxacin, were synthesized. Prodrugs Cipro-Pro 2 and Moxi-Pro 1 showed a significant drop in antibacterial activity compared to their parent drugs and displayed no cellular toxicity. M. C. Ortega-Liebana provided two palladium nanosheets of different sizes, which impaired biofilm formation at higher concentrations. The catalytic activity of the differently sized nanosheets was compared using a fluorogenic assay. Both nanosheets were equally active in PBS, and when 20% serum was added to the PBS. Mass spectrometry showed that the nanosheets could activate both prodrugs. The largest nanosheets were incorporated into an agarose hydrogel, and different Pd-loadings and hydrogels of various thicknesses were tested for their ability to prevent biofilm formation in combination with the prodrugs. In general, Moxi-Pro 1 needed less preincubation time to prevent biofilms compared to Cipro-Pro 2. At a 50 µg/ml Pd loading, the hydrogels combined with Moxi-Pro 1 managed to avoid biofilm formation without preincubation, regardless of whether the hydrogel thickness was 1 or 2 mm. The catalytic activity of the nanosheets was retained over several weeks when stored in PBS but failed to prevent the formation of biofilms on the third day in CASO-medium.

The catalytic release of antibiotics from inactive prodrugs is a suitable strategy to limit their overall exposure in the patient's body and localize it at a desired site. This strategy is especially appealing for preventing biofilm-associated infections of (orthopaedic) implants as the site of antibiotic release is predefined. Additionally, given the side effects of fluoroquinolones or other antibiotics, this strategy might be an exciting approach to limit toxicity and ensure a safe drug release at a defined location.

## 6.5 Supplementary Information

### 6.5.1 Supplementary Figures S1-S7

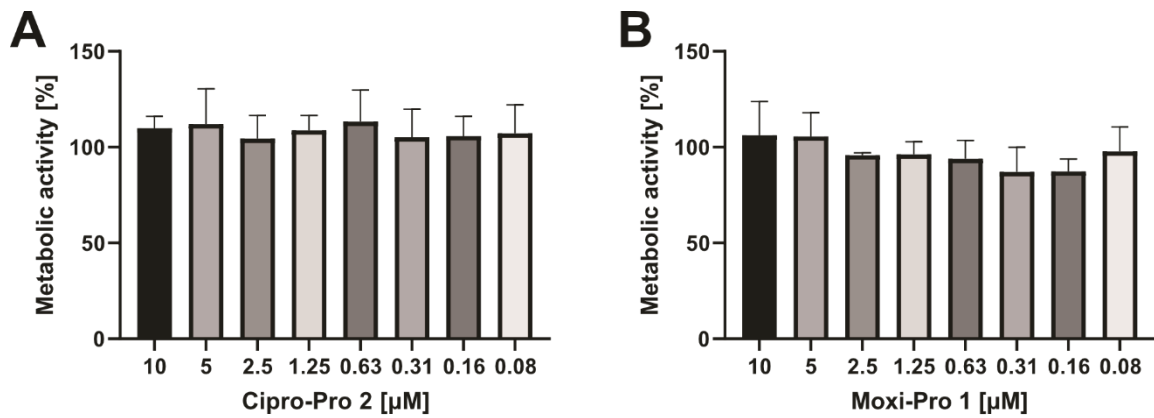


**Figure S1.** Prodrug toxicity on HepG2 cells was determined using an MTT assay after 24 h of compound treatment in an FCS-free DMEM medium. (A) Toxicity of Cipro Pro 2. (B) Toxicity of Moxi Pro 1. Experiments were performed in two biological replicates, with three technical replicates each, which were in qualitative agreement. Error bars:  $\pm$ SD from  $n = 3$ .

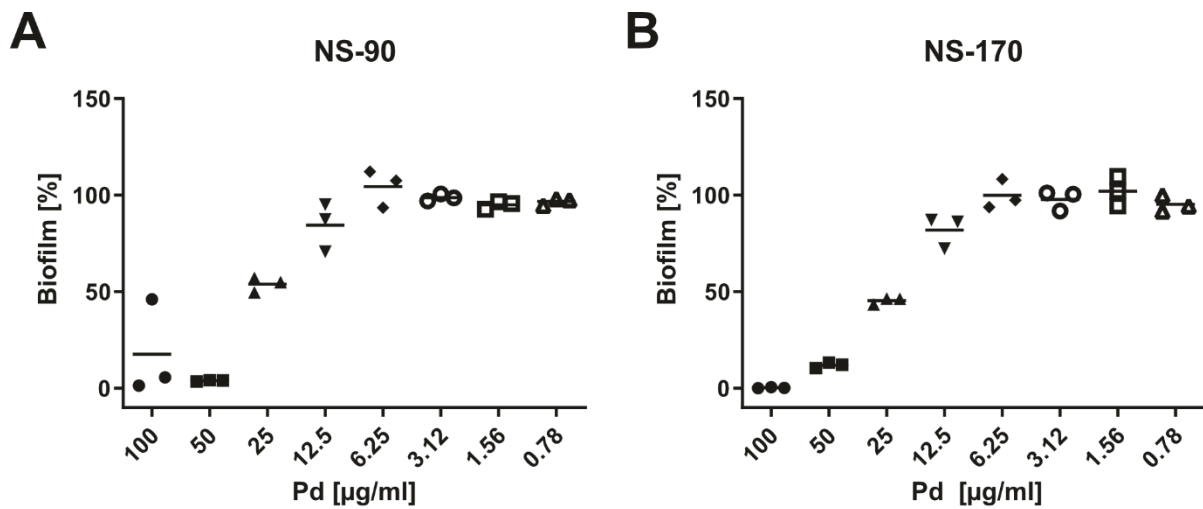


**Figure S2.** Minimal Biofilm Inhibitory Concentration (MBIC) of free nanosheets in CASO medium. (A) MBIC of PdNS-90. (B) MBIC of PdNS-170. Experiments were performed in two biological replicates, with three technical replicates each, which were in qualitative agreement.

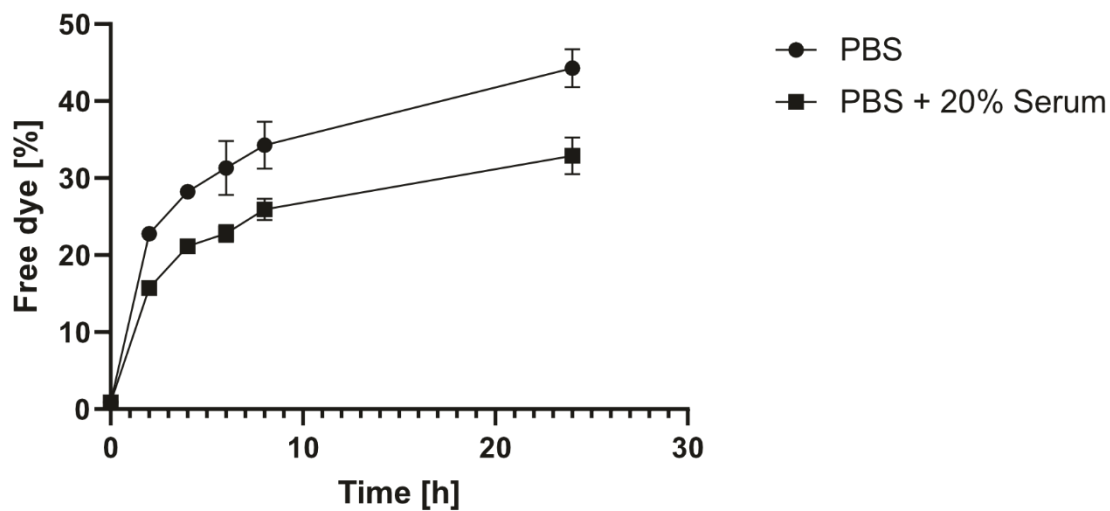


**Figure S3.** Comparison of the catalytic activity of PdNS-90 nanosheets in PBS and PBS + 20% serum. Error bars:  $\pm$ SD from  $n = 3$ .

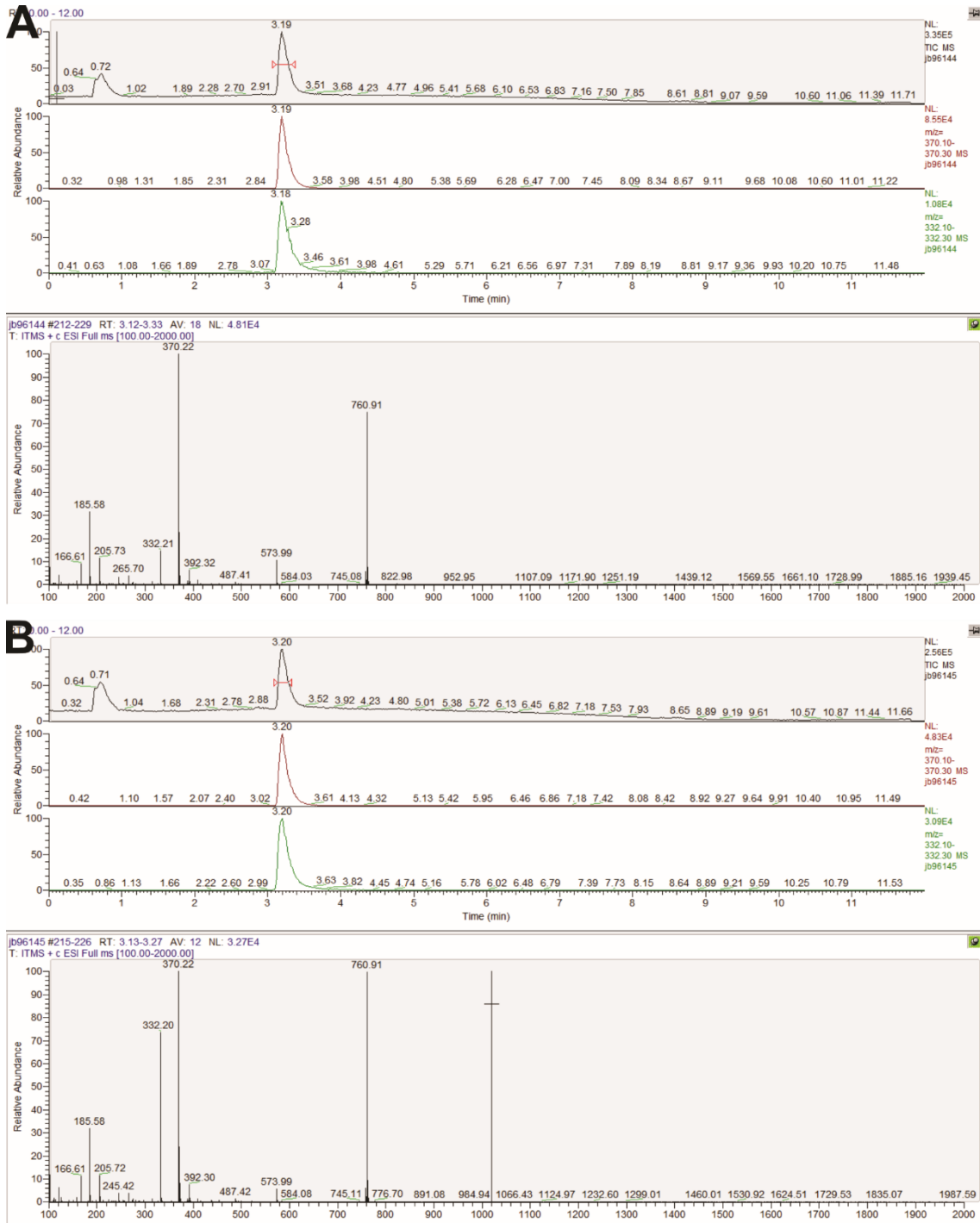


**Figure S4.** Activation of Cipro-Pro 2. (A) MS-analysis after 0 h. (B) MS-analysis after 1 h. The first panel displays the Total Ion Count (TIC). The second panel from the top shows the ion count for the mass range 370.1-370.3 (Cipro-Pro 2). The third panel from the top shows the ion count for the mass range 332.1-332.3 (Ciprofloxacin). The bottom panel displays the ions detected in the marked retention time of the TIC.



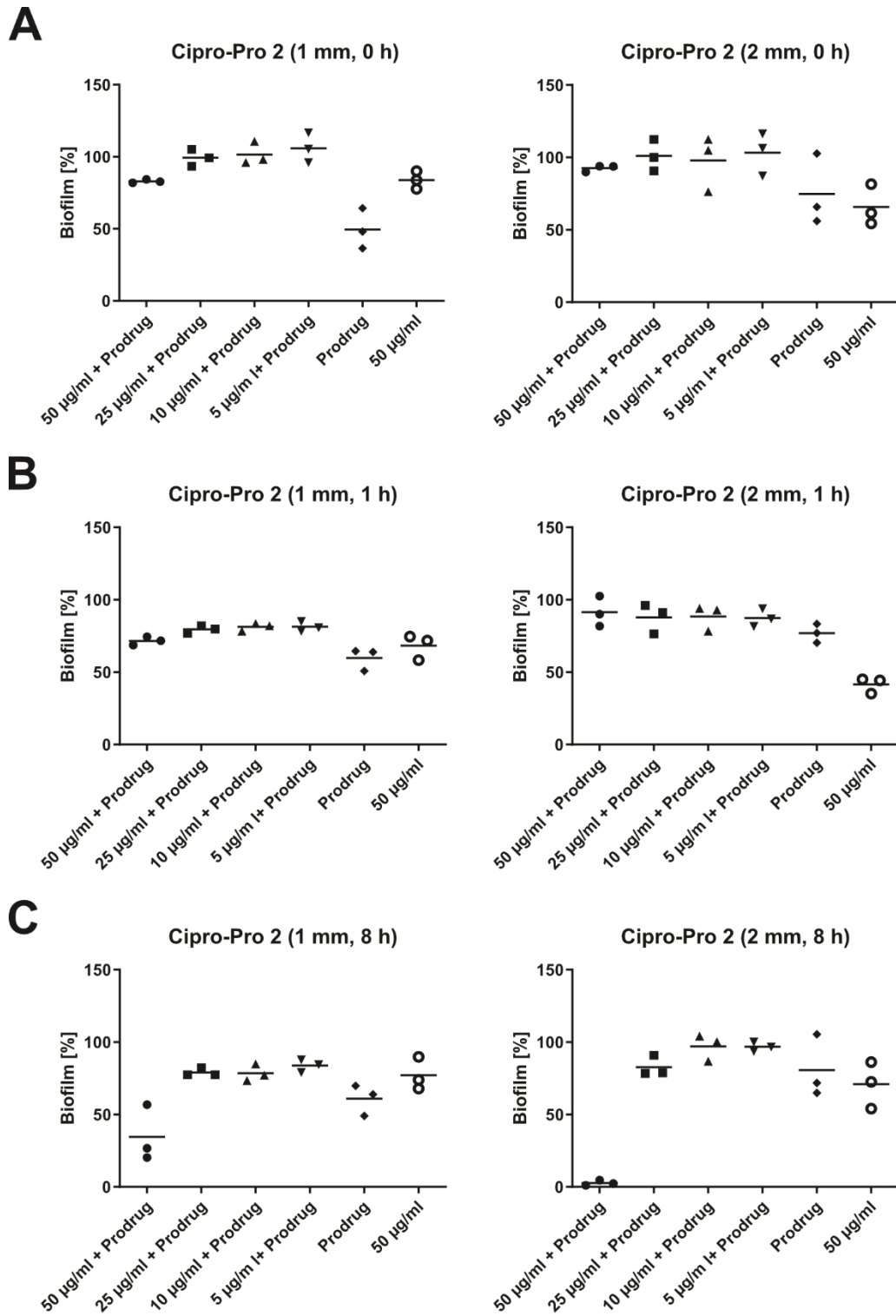


**Figure S6.** In vitro activity of agarose hydrogels loaded with different amounts of palladium nanosheets (PdNS-90) and Cipro-Pro 2 (5 µM) in the medium against *S. aureus* SA113 biofilm formation. (A) Biofilm growth on 1 (left) or 2 mm (right) thick hydrogels with no preincubation of prodrug. (B) Biofilm growth on 1 (left) or 2 mm (right) thick hydrogels with 1 h of preincubation of prodrug. (C) Biofilm growth on 1 (left) or 2 mm (right) thick hydrogels with 8 h of preincubation of prodrug. Experiments were performed in two biological replicates, with three technical replicates each, which were in qualitative agreement.

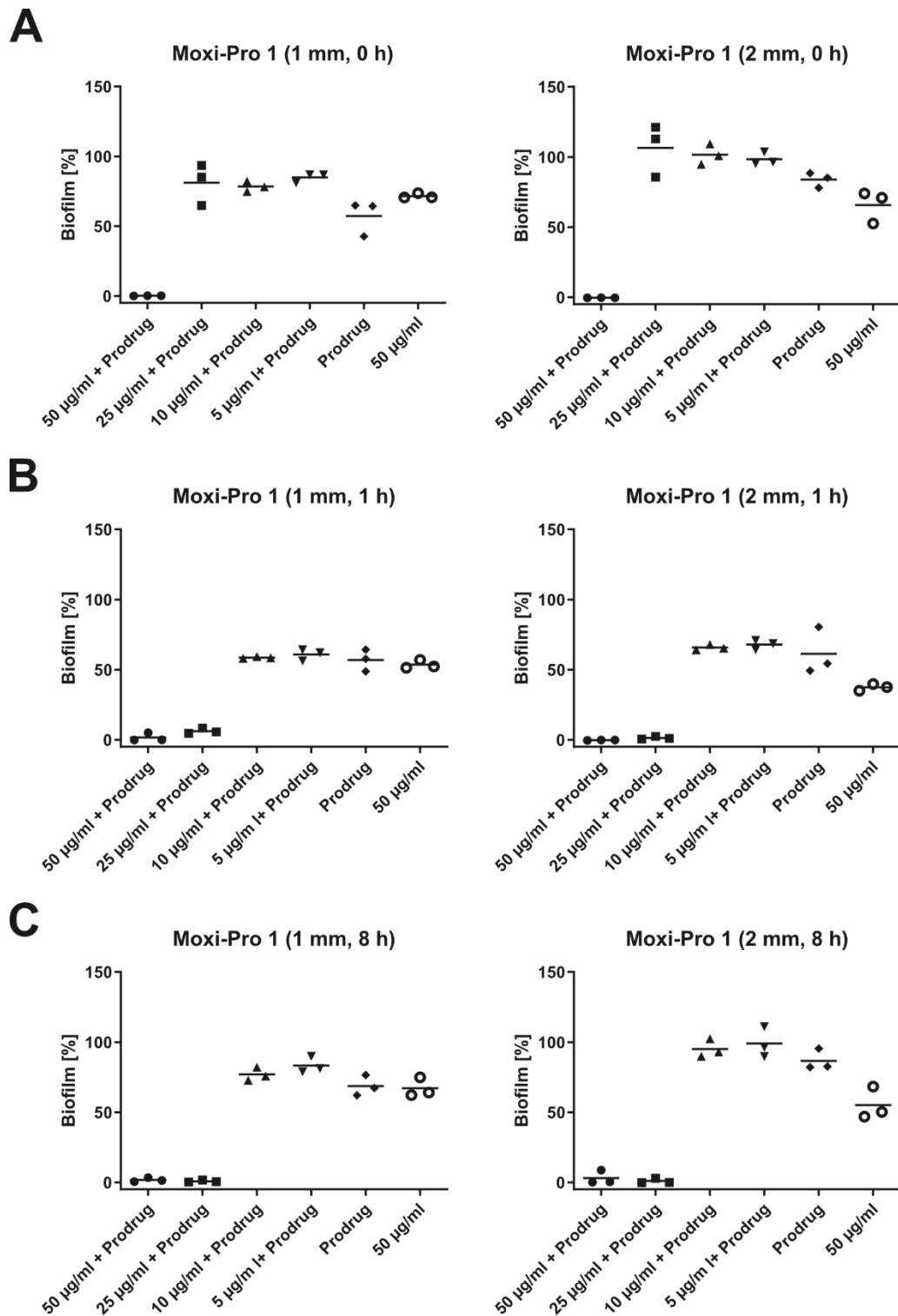


**Figure S 7.** In vitro activity of agarose hydrogels loaded with different amounts of palladium nanosheets (PdNS-90) and Moxi-Pro 1 (5 µM) in the medium against *S. aureus* SA113 biofilm formation. (A) Biofilm growth on 1 (left) or 2 mm (right) thick hydrogels with no preincubation of prodrug. (B) Biofilm growth on 1 (left) or 2 mm (right) thick hydrogels with 1 h of preincubation of prodrug. (C) Biofilm growth on 1 (left) or 2 mm (right) thick hydrogels with 8 h of preincubation of the prodrug. Experiments were performed in two biological replicates, with three technical replicates each, which were in qualitative agreement.

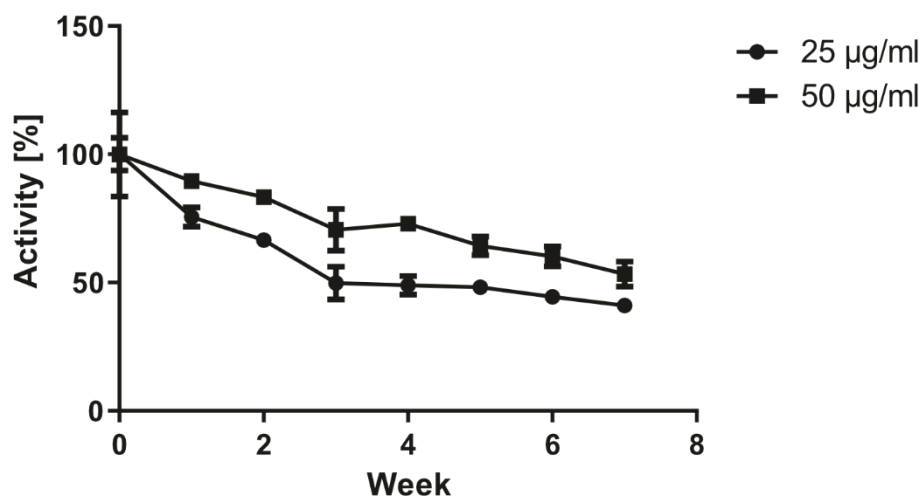


**Figure S8.** Long-term stability of the catalytic activity of PdNS-90 nanosheets in agarose hydrogels. Catalytic activity normalized to the initial activity. Error bars:  $\pm$ SD from  $n = 3$ .

### 6.5.2 Supplementary Tables

**Table S1.** Bacterial strains and media

Species	Strain	Medium
<i>Escherichia coli</i>	UTI89	LB
<i>Staphylococcus aureus</i>	SA133	CASO

**Table S2.** Composition of the used media

Medium	Composition
LB	10.0 g peptone ex casein 5.00 g NaCl 5.00 g yeast extract in 1 l ddH <sub>2</sub> O, pH = 7.5
CASO	17.0 g peptone ex casein 3.00 g peptone ex soybean 2.50 g K <sub>2</sub> HPO <sub>4</sub> 5.00 g NaCl 2.50 g glucose in 1 l ddH <sub>2</sub> O, pH = 7.3

### 6.5.3 Methods

#### **Compounds**

Stocks of Ciprofloxacin, Moxifloxacin, and the prodrug Cipro-Pro 2 were made with 0.1 M HCl<sub>aq</sub>. Stocks of prodrug Cipro-Pro 1, Moxi-Pro 1, and compound 1 were made with DMSO.

#### **Minimal Inhibitory Concentration (MIC) Assay**

The MICs were determined by the broth dilution method. Overnight cultures were diluted at 1:10 000. Various dilutions of the compounds were prepared, and 2 µl were added to 48 µl medium in a 96-well plate (transparent Nunc 96-well flat bottom, Thermo Fisher Scientific). A growth control, containing just a vehicle, was included. To the wells containing the compound or the growth control, 50 µl of the diluted overnight culture was added (Final vehicle conc. 1%). A sterile control, containing only 100 µl medium, was included. The plates were incubated for 24 h at 37 °C and 200 rpm, and the OD600 was measured on a microplate reader (Infinite® M Nano+, Tecan). The lowest concentration at which no bacterial growth could be observed was defined as the minimal inhibitory concentration (MIC). MIC values were determined in two experiments with three technical replicates each.

#### **Minimal Biofilm Inhibitory Concentration (MBIC) Assay**

Overnight cultures of *S. aureus* SA113 were diluted 1:100. Various dilutions of the compounds were prepared, and 2 µl were added to 98 µl medium in a 96-well plate (transparent Nunc 96-well flat bottom, Thermo Fisher Scientific). A growth control, containing just vehicle, was included. To the wells containing the compound or the growth control, 100 µl of the diluted overnight culture was added (Final vehicle conc. 1%). A sterile control, containing only 200 µl medium, was included. The plates were incubated for 24 h at 37 °C without shaking. The supernatant was carefully removed, and each biofilm was washed with 100 µl PBS. The biofilms were dried at 37 °C overnight, and 50 µl crystal violet (1% in ddH<sub>2</sub>O) was added. After 10 min incubation at room temperature, the supernatant was removed, and the biofilms were rinsed twice with 200 µl ddH<sub>2</sub>O. The remaining crystal violet was dissolved in 10% acetic acid, and the absorbance at 595 nm of the solution was determined with a microplate reader (Infinite® M Nano+, Tecan). The lowest concentration at which no biofilm growth could be observed was defined as the minimal biofilm inhibitory concentration (MBIC). MBIC values were determined in two experiments with three technical replicates each.

#### **Minimal Biofilm Inhibitory Concentration of Pd-nanosheets**

An overnight culture of *S. aureus* SA113 was diluted 1:100. To 50 µl of various dilutions of Pd-nanosheets in water in a 96-well plate (transparent Nunc 96-well flat bottom, Thermo Fisher Scientific), 50 µl of the diluted overnight culture were added. The plates were incubated at 37 °C, 200 rpm for 24 h. The medium was carefully aspirated, and the biofilms were carefully

rinsed with 200  $\mu$ l PBS. 100  $\mu$ l PBS and 20  $\mu$ l CellTiter-Blue™ (Promega) were added to each well, and the plates were incubated for 1 h at 37 °C. 100  $\mu$ l were transferred into a new 96-well plate (black pure Grade™ 96-well flat bottom, Brand). Fluorescence (Ex: 560 nm, Em: 590 nm) was determined with a microplate reader (Infinite® M Nano+, Tecan). A growth control, containing just a vehicle, and a negative growth control, containing just vehicle and no bacteria, were included and used to normalize the results. The experiment was conducted twice with three technical replicates each.

### **Prevention of Biofilms by Pd-labile Prodrugs**

Agarose (for DNA electrophoresis, SERVA) hydrogels (20 mg/ml) with PdNS-90 nanosheets (5 – 50  $\mu$ g/ml) were poured into a 96-well plate (transparent pure Grade™ 96-well flat bottom, Brand) to a thickness of 1 or 2 mm and allowed to solidify overnight at room temperature. The plates were sterilized by UV-radiation (1 h), and 50  $\mu$ l of 5  $\mu$ M Prodrug in CASO-Medium (1% vehicle) was added. The plates were incubated for 0, 1, or 8 h at 37 °C. An overnight culture of *S. aureus* SA113 was diluted 1:100 with CASO-medium, and 50  $\mu$ l was added to each well. The plates were incubated for 24 h at 37 °C before carefully aspirating the medium. The biofilms were washed with 200  $\mu$ l PBS and 100  $\mu$ l PBS, and 20  $\mu$ l CellTiter-Blue™ (Promega) were added to each well. The plates were incubated for 1 h at 37 °C, and 100  $\mu$ l were transferred into a new 96-well plate (black pure Grade™ 96-well flat bottom, Brand). Fluorescence (Ex: 560 nm, Em: 590 nm) was determined with a microplate reader (Infinite® M Nano+, Tecan). Controls containing only Pd-nanosheets or prodrugs were included. A growth control, containing just a vehicle, and a negative growth control, containing just vehicle and no bacteria, were included and used to normalize the results. Inhibition of biofilm growth was determined in two experiments with three technical replicates each.

### **General cell culture**

HepG2 cells were obtained from DSMZ and cultured in Dulbecco's Modified Eagle's Medium high glucose (DMEM) supplemented with heat-inactivated 10% (v/v) fetal bovine serum (FBS, Sigma-Aldrich) and 2 mM L-glutamine (Sigma-Aldrich). Cells were grown at 37 °C and 5% CO<sub>2</sub>.

Human breast adenocarcinoma MDA-MB-231 cells and human colon carcinoma HCT116 cells (purchased from ECACC) were cultured in culture media supplemented with serum (10 % of FBS) and L-glutamine (2 mM). HCT116 cells were cultured in McCoy's 5A medium, and MDA-MB-231 cells were cultured in DMEM media supplemented with serum (10 % of FBS) and L-glutamine (2 mM). Each cell line was checked for mycoplasma before use and maintained in normoxic conditions at 37 °C and 5% CO<sub>2</sub>.

### **Study of the biocompatibility of Pd nanosheets**

The tolerability of cells to PdNS-90 and PdNS-170 was tested by performing dose-response studies in HCT116 and MDA-MB-231 cells. Cells were seeded in a 96-well plate at a density of 1.500 cells/well for MDA-MB-231 cells and 3.000 cells/well for HCT116 cells; then incubated for 24 h before treatment. Each well was then replaced with 100  $\mu$ L of fresh media containing PdNS-90 or PdNS-170 at 2, 5, 10, 20, and 30  $\mu$ g/mL for all cells. After 1 week, PrestoBlue™ cell viability reagent (10 % v/v) was added to each well, and the plate was incubated for 90 min. Fluorescence emission was detected using a PerkinElmer EnVision 2101 multilabel reader (Ex/Em: 540/590 nm). Experiments were performed in triplicate. All conditions were normalized to the untreated cells (100 %).

### **Compound Toxicity Assay**

The MTT assay was used to determine compound toxicity. HepG2 cells (12000 in 200  $\mu$ l medium per well) were seeded into a 96-well plate (BioLite™, Thermo Fisher Scientific) and were grown for 1 d at 37 °C and 5%. The medium was aspirated, and 100  $\mu$ l of FCS-free medium with various concentrations of the compound (1% final conc. of the vehicle) or vehicle (1% final conc.) were added. The cells were incubated with the compound or controls for 24 h, and 20  $\mu$ l of thiazolyl blue tetrazolium bromide (MTT, 5 mg/ml in PBS, Sigma-Aldrich) were added. The plates were incubated for 3 h at 37 °C, 5% CO<sub>2</sub>, and 80  $\mu$ l of supernatant was carefully removed. The formazan crystals were dissolved in 200  $\mu$ l of DMSO, and the absorbance at 570 nm was measured on a microplate reader (Infinite® M Nano+, Tecan), and the background at 630 nm was subtracted. Metabolic activity was normalized to the vehicle control. Metabolic activity was determined in two experiments with three technical replicates each.

### **Fluorophore Activation Studies**

Per time point, 100  $\mu$ l of 100  $\mu$ M compound **1** in PBS or PBS + 20% mouse serum (Sigma-Aldrich) were incubated with 5  $\mu$ g/ml Pd-nanosheets at 37 °C and 200 rpm (Final DMSO conc. 1%). Timepoint t=0 never contained any Pd. At the respective time points, samples were spun down (13 000 rpm, 15 min), and 75  $\mu$ l of the supernatant was transferred to a 96-well plate (black pure Grade™ 96-well flat bottom, Brand). Fluorescence (Ex: 350 nm, Em: 450 nm) was determined with a microplate reader (Infinite® M Nano+, Tecan). An external calibration curve was used to quantify the conversion. All time points were done in technical triplicates.

### **MS-based Prodrug Conversion Studies**

Per time point, 100  $\mu$ l of 100  $\mu$ M of the respective prodrug in PBS were incubated with 5  $\mu$ g/ml PdNS-90 at 37 °C and 200 rpm (Final vehicle conc. 1%). Timepoint t=0 never contained any Pd. At the respective time points, samples were spun down (13 000 rpm, 15 min), and 75  $\mu$ l of

the supernatant was transferred into MS vials. The samples were measured on a LCQ-Fleet (Thermo Fisher Scientific) coupled to an UltiMate 3000 HPLC (Thermo Fisher Scientific). An external calibration curve of the prodrug was used to quantify the conversion.

### Longterm Stability Assay

Agarose (for DNA electrophoresis, SERVA) hydrogels (20 mg/ml) with PdNS-90 nanosheets (25 or 50  $\mu\text{g/ml}$ ) was poured into a 96-well plate (transparent pure Grade™ 96-well flat bottom, Brand) to a thickness of 1 mm and allowed to solidify overnight. The plates were sterilized by UV-radiation (1 h), and 200  $\mu\text{l}$  PBS was added. The plates were incubated at 37 °C for various intervals. The PBS was aspirated weekly, and 200  $\mu\text{l}$  of fresh PBS was added. For the wells of the respective time point, the PBS was removed and replaced by 100  $\mu\text{M}$  compound **1** in PBS (1% DMSO). The plates were incubated at 37 °C, and 50  $\mu\text{l}$  of the compound **1** solution was transferred to a new 96-well plate (black pure Grade™ 96-well flat bottom, Brand). Fluorescence (Ex: 350 nm, Em: 450 nm) was determined with a microplate reader (Infinite® M Nano+, Tecan). An external calibration curve was used to quantify the conversion. All time points were done in technical triplicates.

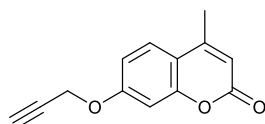
### General Synthetic Methods and Materials

All reagents and solvents were purchased in reagent grade or higher from commercial vendors (Sigma-Aldrich, Thermo Fisher Scientific Inc., Merck KGaA, Alfa Aesar, Roth, VWR International, and Acros Chemicals). They were used as delivered without further purification. All air and/or water-sensitive reactions were conducted under an argon atmosphere using flame-dried glassware using standard Schlenk techniques. Merck silica-gel 60 F254 plates were used for analytical thin-layer chromatography (TLC). The spots were visualized using short wave UV light ( $\lambda=254$  nm and 366 nm) or a  $\text{KMnO}_4$ -stain (1.50 g  $\text{KMnO}_4$ , 10.0 g  $\text{K}_2\text{CO}_3$ , 1.25 mL  $\text{NaOH}_{\text{aq}}$  (10 wt-%), 200 mL  $\text{ddH}_2\text{O}$ ). Flash chromatography was performed using Silica gel 60 (particle size = 40–63  $\mu\text{m}$ ) from Merck KGaA with compressed air. Proton-NMR spectra were recorded on Avance-III (AV-HD300, AV-HD400, or AV-HD500) NMR systems (Bruker Co.) at room temperature in deuterated Chloroform ( $\text{CDCl}_3$ ) or Dimethylsulfoxide ( $\text{DMSO-d}_6$ ). Spectra were referenced to the residual proton signal of the corresponding deuterated solvent ( $\text{CDCl}_3$ :  $\delta = 7.26$  ppm,  $\text{DMSO-d}_6$ :  $\delta = 2.50$  ppm). Chemical shifts are reported in parts per million (ppm). Coupling constants ( $J$ ) are reported in hertz (Hz). The following abbreviations were used for the multiplicity assignment to the signals: virt. = virtual, s = singlet, br s = broad singlet, d = doublet, t = triplet, q = quartet, p = pentet, m = multiplet or unresolved.  $^{13}\text{C}$ -NMR spectra were collected on Avance-III (AV-HD300, AV-HD400) NMR systems (Bruker Co.) at 75, 101 MHz with  $\text{CDCl}_3$  or  $\text{DMSO-d}_6$  as solvents. Chemical shifts were referenced to the residual solvent peak as an internal standard ( $\text{CDCl}_3$ :  $\delta = 77.16$  ppm,  $\text{DMSO-d}_6$ :  $\delta = 39.52$  ppm). High-resolution mass spectra were recorded using an LTQ-FT Ultra

(Thermo Fisher Scientific) coupled with a Dionex UltiMate 3000 HPLC system and an ESI or APCI ion source.

## Synthesis

### O-Propargyl-4-methyl-umbelliferone (1)



Chemical Formula: C<sub>13</sub>H<sub>10</sub>O<sub>3</sub>  
Molecular Weight: 214.22 g/mol

O-Propargyl-4-methyl-umbelliferone was synthesized as previously reported.<sup>[141]</sup>

4-Methyl-umbelliferone (1.00 g, 5.68 mmol, 1.0 eq) was dissolved in acetone (20 ml), and K<sub>2</sub>CO<sub>3</sub> (1.57 g, 11.4 mmol, 2.0 eq) was added. Propargyl bromide (860 μl, 1.35 g, 11.4 mmol, 2.0 eq) was added dropwise. The reaction was heated to 50 °C and stirred at this temperature overnight. The reaction was allowed to reach room temperature, and the volatile components were removed under reduced pressure. Water (100 ml) was added to the residue, and the resulting solid was filtered off. Purification by recrystallization from ethanol (20 ml) yielded the desired product (917 mg, 4.26 mmol, 75%) as an off-white solid.

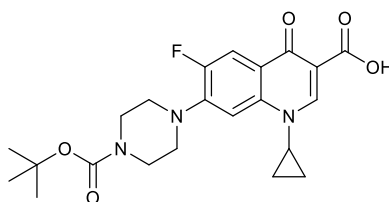
**HRMS ESI** calcd. for C<sub>13</sub>H<sub>11</sub>O<sub>3</sub> [M+H]<sup>+</sup>: 215.0703, found 215.0694.

**<sup>1</sup>H-NMR** (400 MHz, CDCl<sub>3</sub>): δ [ppm] = 7.66 – 7.41 (m, 1H), 7.00 – 6.81 (m, 2H), 6.16 (q, *J* = 1.2 Hz, 1H), 4.76 (d, *J* = 2.4 Hz, 2H), 2.57 (t, *J* = 2.4 Hz, 1H), 2.41 (d, *J* = 1.2 Hz, 3H).

**<sup>13</sup>C-NMR** (101 MHz, CDCl<sub>3</sub>): δ [ppm] = 161.2, 160.5, 155.2, 152.5, 125.8, 114.4, 112.9, 112.6, 102.6, 76.6, 56.3, 18.8.

The spectroscopic data is in accordance with the literature.<sup>[142]</sup>

### N-Boc-Ciprofloxacin (2)



Chemical Formula: C<sub>22</sub>H<sub>26</sub>FN<sub>3</sub>O<sub>5</sub>  
Molecular Weight: 431.46 g/mol

N-Boc-Ciprofloxacin was synthesized as previously reported.<sup>[143]</sup>

Ciprofloxacin (500 mg, 1.51 mmol, 1.0 eq) was dissolved in dioxane/water (50:50, 9 ml), and NaOH<sub>aq</sub> (1 M, 2.26 ml, 90.5 mg, 2.26 mmol, 1.5 eq) and Boc anhydride (494 mg, 2.26 mmol, 1.5 eq) were added. The reaction was stirred at room temperature overnight, and the volatile components were removed under reduced pressure. Purification by flash chromatography (DCM/MeOH = 95:5) yielded the desired product (486 mg, 1.13 mmol, 75%) as a white solid.

**TLC:**  $R_f$  = 0.39 (DCM/MeOH = 95:5) [UV]

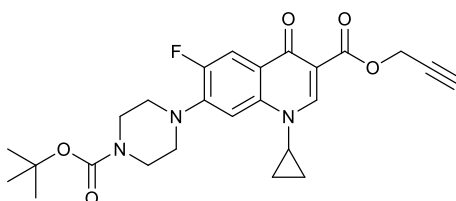
**HRMS ESI** calcd. for C<sub>22</sub>H<sub>27</sub>FN<sub>3</sub>O<sub>5</sub> [M+H]<sup>+</sup>: 432.1924, found 432.1926.

**<sup>1</sup>H-NMR** (400 MHz, CDCl<sub>3</sub>):  $\delta$  [ppm] = 14.93 (s, 1H), 8.78 (s, 1H), 8.05 (d,  $J$  = 12., 1H), 7.36 (d,  $J$  = 7.1 Hz, 1H), 3.69 – 3.65 (m, 4H), 3.60 – 3.48 (m, 1H), 3.34 – 3.26 (m, 4H), 1.50 (s, 9H), 1.43 – 1.37 (m, 2H), 1.24 – 1.18 (m, 2H).

**<sup>13</sup>C-NMR** (101 MHz, CDCl<sub>3</sub>):  $\delta$  [ppm] = 167.1, 154.7, 147.7, 113.0, 112.7, 108.5, 105.1, 80.5, 35.4, 28.6, 8.4.

The spectroscopic data is in accordance with the literature.<sup>[143]</sup>

### **N-Boc-O-Propargyl-Ciprofloxacin (3)**



Chemical Formula: C<sub>25</sub>H<sub>28</sub>FN<sub>3</sub>O<sub>5</sub>  
Molecular Weight: 469.51 g/mol

N-Boc-O-Propargyl-Ciprofloxacin was synthesized analogous to previous reports.<sup>[144]</sup>

Compound **2** (468 mg, 1.08 mmol, 1.0 eq) was dissolved in dry DCM (15 ml). HBTU (514 mg, 1.36 mmol, 1.3 eq), DMAP (13.5 mg, 108  $\mu$ mol, 0.1 eq), trimethylamine (166  $\mu$ l, 121 mg, 1.19 mmol, 1.1 eq), and propargyl alcohol (256  $\mu$ l, 243 mg, 4.34 mmol, 4.0 eq) were added sequentially. The reaction was stirred at room temperature overnight, and the volatile components were removed under reduced pressure. The crude product was purified by flash chromatography (DCM/MeOH = 97:3), yielding the desired product (208 mg, 443  $\mu$ mol, 41%) as a white solid.

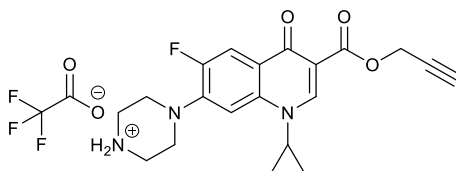
**TLC:**  $R_f$  = 0.26 (DCM/MeOH = 95:5) [UV]

**HRMS ESI** calcd. for C<sub>25</sub>H<sub>29</sub>FN<sub>3</sub>O<sub>5</sub> [M+H]<sup>+</sup>: 470.2086, found 470.2082.

**<sup>1</sup>H-NMR** (400 MHz, CDCl<sub>3</sub>): δ [ppm] = 8.55 (s, 1H), 8.02 (d, *J* = 13.1 Hz, 1H), 7.27 (s, 1H), 4.92 (d, *J* = 2.4 Hz, 2H), 3.69 – 3.61 (m, 4H), 3.51 – 3.38 (m, 1H), 3.24 – 3.17 (m, 4H), 2.49 (t, *J* = 2.4 Hz, 1H), 1.50 (s, 9H), 1.38 – 1.30 (m, 2H), 1.19 – 1.13 (m, 2H).

**<sup>13</sup>C-NMR** (101 MHz, CDCl<sub>3</sub>): δ [ppm] = 173.0, 164.8, 154.8, 154.8, 152.3, 148.7, 144.7, 144.6, 138.1, 123.4, 123.4, 113.7, 113.5, 109.6, 105.2, 105.2, 80.4, 78.3, 74.9, 52.3, 34.8, 28.6, 8.3.

### O-Propargyl-Ciprofloxacin trifluoroacetate (Cipro-Pro 2)



Chemical Formula: C<sub>22</sub>H<sub>21</sub>F<sub>4</sub>N<sub>3</sub>O<sub>5</sub>  
Molecular Weight: 483.42 g/mol

O-Propargyl-Ciprofloxacin trifluoroacetate was synthesized analogous to previous reports.<sup>[144]</sup>

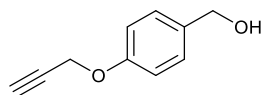
Compound **3** (200 mg, 426 μmol, 1.0 eq) was dissolved in a mixture of DCM (6 ml) and trifluoroacetic acid (3 ml), and the solution was stirred at room temperature for 2 h. Diethyl ether (20 ml) was added, and the product (96.5 mg, 200 μmol, 47%) was filtered off as a white solid.

**HRMS ESI** calcd. for C<sub>20</sub>H<sub>21</sub>FN<sub>3</sub>O<sub>3</sub> [M+H]<sup>+</sup>: 370.1561, found 370.1559.

**<sup>1</sup>H-NMR** (500 MHz, DMSO-d<sub>6</sub>): δ [ppm] = 8.91 (br s, 2H), 8.48 (s, 1H), 7.81 (d, *J* = 13.1 Hz, 1H), 7.49 (d, *J* = 7.4 Hz, 1H), 4.84 (d, *J* = 2.4 Hz, 2H), 3.72 – 3.66 (m, 1H), 3.57 (t, *J* = 2.4 Hz, 1H), 3.33 (s, 4H), 1.31 – 1.21 (m, 2H), 1.14 – 1.07 (m, 2H).

**<sup>13</sup>C-NMR** (126 MHz, DMSO): δ [ppm] = 171.5, 163.6, 158.2, 157.9, 153.6, 151.6, 148.9, 142.9, 142.8, 138.1, 122.6, 112.0, 111.8, 108.3, 107.0, 79.0, 77.6, 51.5, 46.7, 42.8, 35.1, 7.7.

### (4-(Prop-2-yn-1-yloxy)phenyl)methanol (**4**)



Chemical Formula: C<sub>10</sub>H<sub>10</sub>O<sub>2</sub>  
Molecular Weight: 162.19 g/mol

Compound **4** was synthesized as reported in the literature.<sup>[145]</sup>

4-Hydroxybenzyl alcohol (2.50 g, 20.1 mmol, 1.0 eq) was dissolved in acetonitrile (50 ml), and K<sub>2</sub>CO<sub>3</sub> (4.70 g, 34.0 mmol, 1.7 eq) was added. The mixture was stirred for 1 h at room temperature, and propargyl bromide (80%, 2.56 ml, 3.21 g, 27.0 mmol, 1.4 eq) was added. The reaction was heated to 80 °C and stirred at this temperature for 2 days. The reaction was

allowed to reach room temperature, the solids were filtered off, and the volatile components were removed under reduced pressure. Purification by flash chromatography (Hex/EtOAc = 1:0 → 1:1) yielded the desired product (2.72 g, 16.7 mmol, 83%) as a yellow oil.

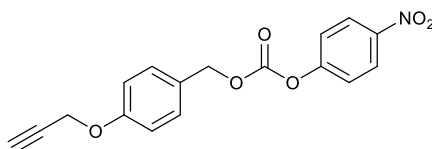
**TLC:**  $R_f$  = 0.35 (Hex/EtOAc = 2:1) [UV]

**$^1\text{H-NMR}$**  (400 MHz,  $\text{CDCl}_3$ ):  $\delta$  [ppm] = 7.55 – 7.25 (m, 2H), 7.09 – 6.78 (m, 2H), 4.70 (d,  $J$  = 2.4 Hz, 2H), 4.63 (s, 2H), 2.52 (s, 1H).

**$^{13}\text{C-NMR}$**  (101 MHz,  $\text{CDCl}_3$ ):  $\delta$  [ppm] = 157.3, 134.2, 128.7, 115.2, 78.6, 75.7, 65.1, 56.0.

The spectroscopic data is in accordance with the literature.<sup>[145]</sup>

#### 4-Nitrophenyl 4-propargyloxybenzyl carbonate (5)



Chemical Formula:  $\text{C}_{17}\text{H}_{13}\text{NO}_6$   
Molecular Weight: 327.29 g/mol

4-Nitrophenyl 4-propargyloxybenzyl carbonate was synthesized as reported in the literature.<sup>[145]</sup>

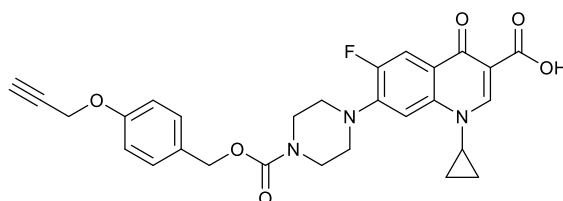
(4-(Prop-2-yn-1-yloxy)phenyl)methanol (4, 1.00 g, 6.17 mmol, 1.0 eq) and pyridine (54  $\mu\text{l}$ , 53.7 mg, 678  $\mu\text{mol}$ , 0.1 eq) were dissolved in dichloromethane (20 ml). The solution was cooled to 0 °C, and 4-nitrophenyl chloroformate (1.37 g, 6.78 mmol, 1.1 eq) dissolved in dichloromethane (20 ml) was slowly added. The reaction was stirred overnight and allowed to reach room temperature. The volatile components were removed under reduced pressure. The residue was dissolved in ethyl acetate (100 ml) and washed with water (2  $\times$  100 ml) and brine (2  $\times$  100 ml). The organic phase was dried over  $\text{Na}_2\text{SO}_4$ , and the volatile organic compounds were removed under reduced pressure to yield the desired product (1.65 g, 5.04 mmol, 82%) as a white solid.

**$^1\text{H-NMR}$**  (400 MHz,  $\text{CDCl}_3$ ):  $\delta$  [ppm] = 8.27 (d,  $J$  = 9.1 Hz, 2H), 7.60 – 7.33 (m, 4H), 7.01 (d,  $J$  = 8.7 Hz, 2H), 5.24 (s, 2H), 4.72 (d,  $J$  = 2.3 Hz, 2H), 2.53 (t,  $J$  = 2.3 Hz, 1H).

**$^{13}\text{C-NMR}$**  (101 MHz,  $\text{CDCl}_3$ ):  $\delta$  [ppm] = 158.3, 155.7, 152.6, 130.8, 127.4, 125.4, 121.9, 115.3, 78.4, 75.9, 70.9, 56.0.

The spectroscopic data is in accordance with the literature.<sup>[145]</sup>

### O-(4-Propargyloxybenzyl)-N-ciprofloxacin carbamate (Cipro-Pro 1)



Chemical Formula:  $C_{28}H_{26}FN_3O_6$   
Molecular Weight: 519.53 g/mol

Ciprofloxacin (605 mg, 1.82 mmol, 1.1 eq) and triethylamine (463  $\mu$ l, 336 mg, 3.32 mmol, 2.0 eq) were dissolved in DMF (40 ml). Compound **5** (543 mg, 1.66 mmol, 1.0 eq), dissolved in DMF (10 ml), was added dropwise. The reaction was stirred at room temperature over the weekend, and the volatile components were removed under reduced pressure. Purification by flash chromatography (DCM/MeOH = 97:3) yielded the desired product (457 mg, 880  $\mu$ mol, 53%) as a white solid.

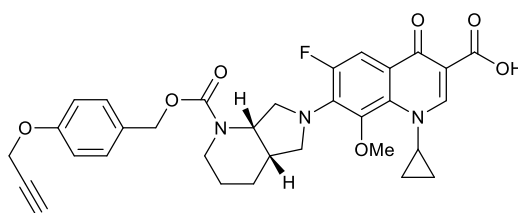
**TLC:**  $R_f$  = 0.22 (DCM/MeOH = 95:5) [UV]

**HRMS ESI** calcd. for  $C_{28}H_{27}FN_3O_6$  [ $M+H^+$ ]<sup>+</sup>: 520.1873, found 520.1875.

**<sup>1</sup>H-NMR** (500 MHz, DMSO- $d_6$ ):  $\delta$  [ppm] = 8.67 (s, 1H), 7.94 (d,  $J$  = 13.1 Hz, 1H), 7.59 (d,  $J$  = 7.5 Hz, 1H), 7.35 (d,  $J$  = 8.7 Hz, 2H), 6.99 (d,  $J$  = 8.7 Hz, 2H), 5.05 (s, 2H), 4.80 (d,  $J$  = 2.4 Hz, 2H), 3.86 – 3.76 (m, 1H), 3.58 (t,  $J$  = 2.4 Hz, 1H), 1.37 – 1.28 (m, 2H), 1.20 – 1.14 (m, 2H).

**<sup>13</sup>C-NMR** (126 MHz, DMSO- $d_6$ ):  $\delta$  [ppm] = 166.0, 157.0, 154.5, 148.2, 129.7, 114.8, 79.3, 78.4, 66.3, 55.40, 49.3, 36.0, 7.7.

### O-(4-Propargyloxybenzyl)-N-moxifloxacin carbamate (Moxi-Pro-1)



Chemical Formula:  $C_{32}H_{32}FN_3O_7$   
Molecular Weight: 589.62 g/mol

Moxifloxacin hydrochloride (294 mg, 672  $\mu\text{mol}$ , 1.1 eq) was dissolved in DMF (15 ml), and triethylamine (264  $\mu\text{l}$ , 192 mg, 1.89 mmol, 3.1 eq) was added. Compound **5** (200 mg, 611  $\mu\text{mol}$ , 1.0 eq), dissolved in DMF (3 ml), was added dropwise. The reaction was stirred at room temperature for 4 d, and the volatile components were removed under reduced pressure. The crude product was purified by flash chromatography (DCM/MeOH = 1:0  $\rightarrow$  98:2) and preparative HPLC (40  $\rightarrow$  98%, 17 min) to yield the desired product (136 mg, 226  $\mu\text{mol}$ , 37%) as an off-white solid.

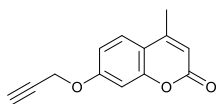
**TLC:**  $R_f$  = 0.15 (DCM/MeOH = 98:2) [UV]

**HRMS ESI** calcd. for  $\text{C}_{32}\text{H}_{33}\text{FN}_3\text{O}_7$   $[\text{M}+\text{H}]^+$ : 560.2297, found 560.2294.

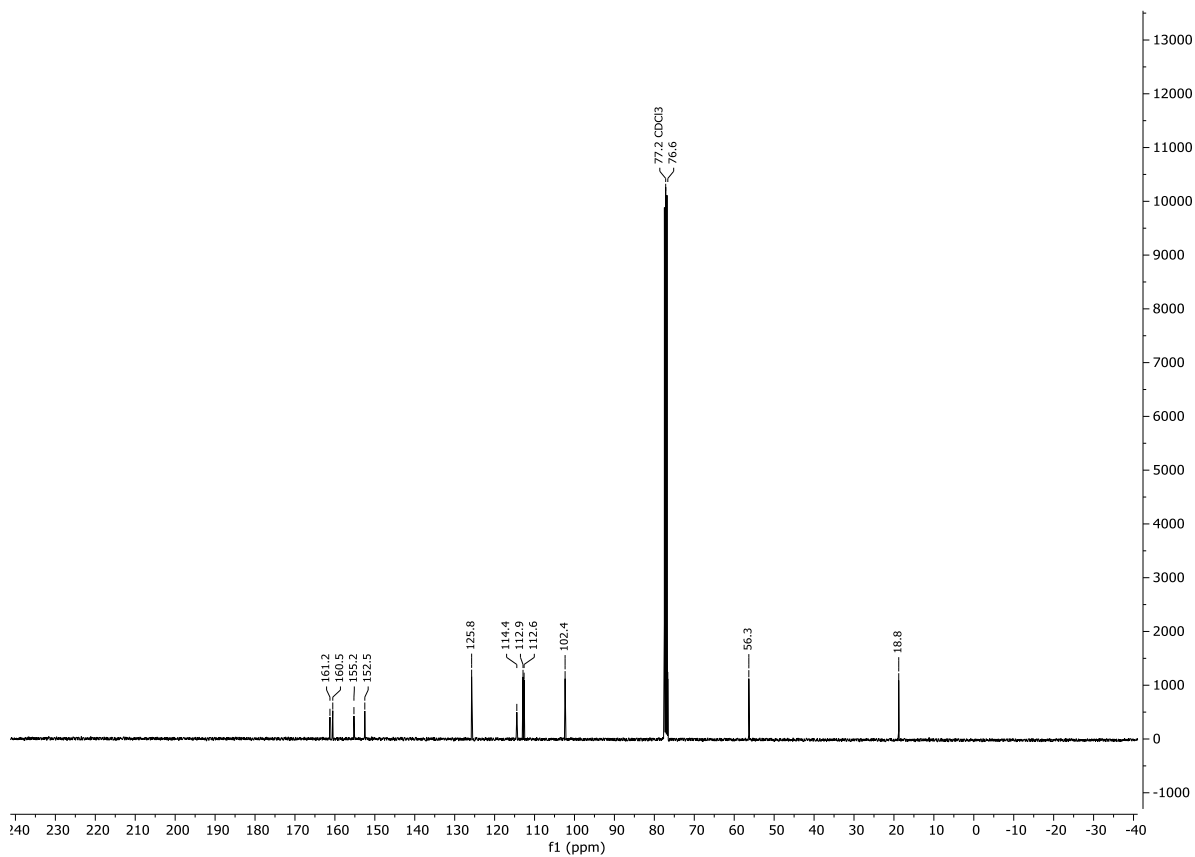
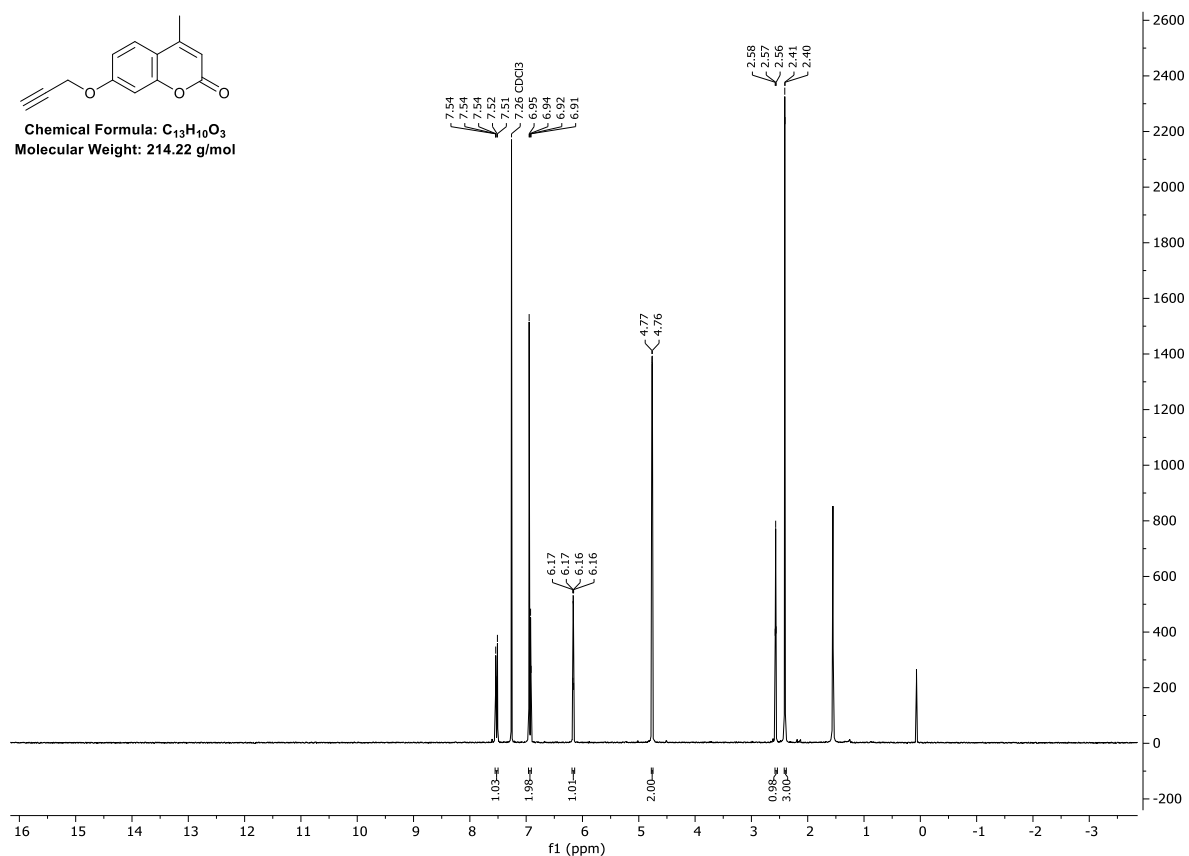
**$^1\text{H-NMR}$**  (400 MHz,  $\text{CDCl}_3$ ):  $\delta$  [ppm] = 8.75 (s, 1H), 7.75 (d,  $J$  = 13.9 Hz, 1H), 7.32 (d,  $J$  = 8.7 Hz, 2H), 6.95 (d,  $J$  = 8.6 Hz, 2H), 5.09 (s, 2H), 4.83 (br s, 1H), 4.68 (d,  $J$  = 2.4 Hz, 2H), 4.18 – 4.04 (m, 2H), 4.02 – 3.93 (m, 1H), 3.91 – 3.84 (m, 1H), 3.56 (s, 3H), 3.40 (br s, 1H), 3.27 (d,  $J$  = 10.6 Hz, 1H), 2.94 (t,  $J$  = 11.6 Hz, 1H), 2.51 (t,  $J$  = 2.4 Hz, 1H), 2.39 – 2.16 (m, 1H), 1.90 – 1.74 (m, 2H), 1.63 – 1.39 (m, 2H), 1.37 – 1.21 (m, 1H), 1.19 – 0.99 (m, 2H), 0.90 – 0.75 (m, 1H).

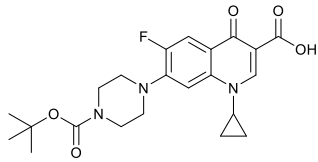
**$^{13}\text{C-NMR}$**  (101 MHz,  $\text{CDCl}_3$ ):  $\delta$  [ppm] = 176.8, 167.1, 157.6, 156.0, 155.0, 152.5, 149.8, 141.0, 137.4, 137.3, 134.5, 130.0, 129.7, 118.8, 115.0, 108.2, 108.0, 107.7, 78.5, 75.8, 67.2, 61.3, 56.6, 56.5, 55.9, 52.7, 40.5, 39.7, 35.6, 25.3, 24.1, 10.7, 8.6.

# NMR Spectra

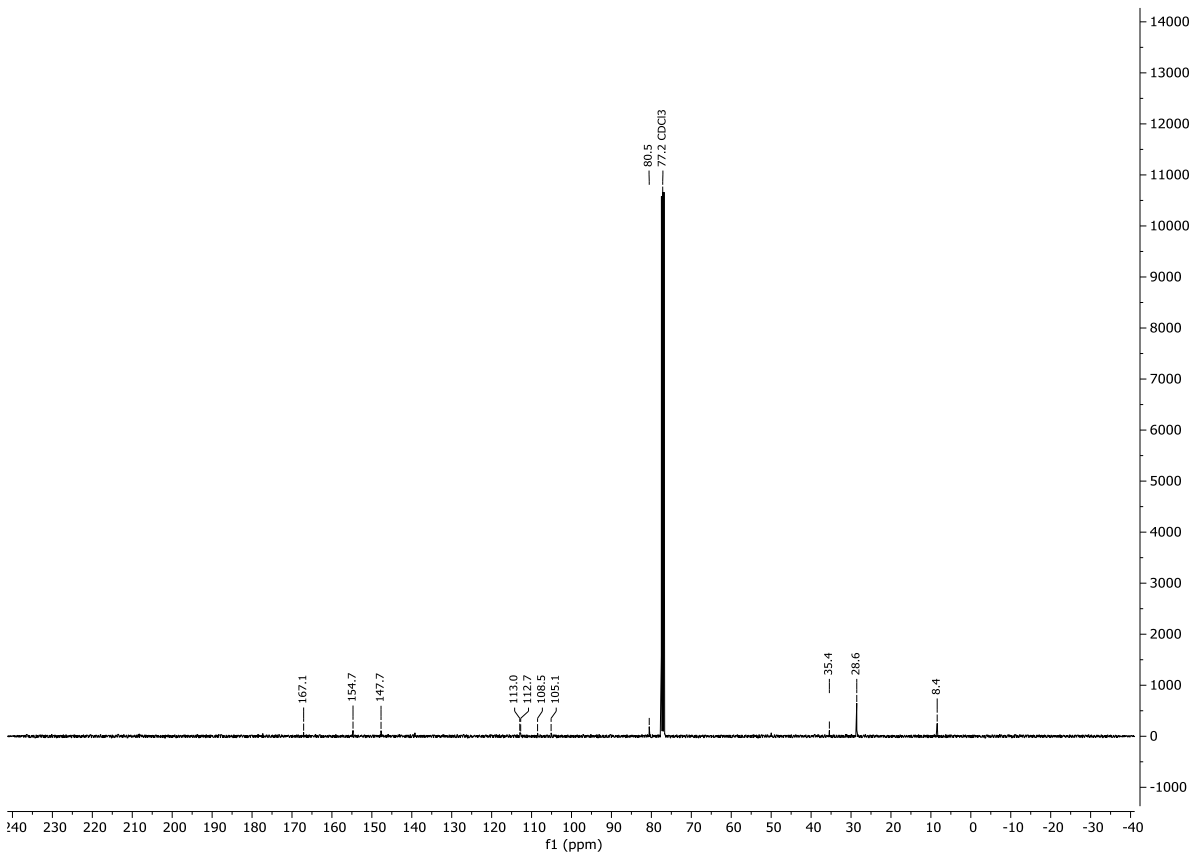
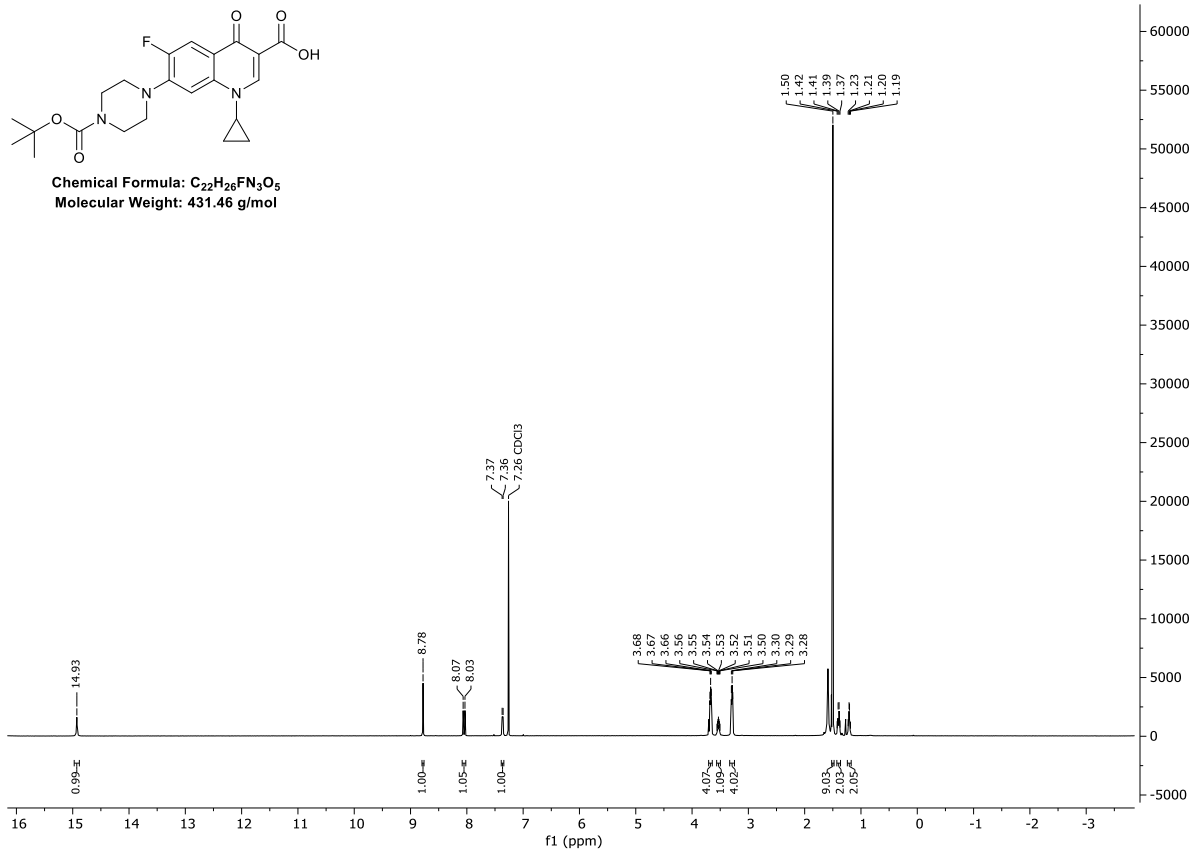


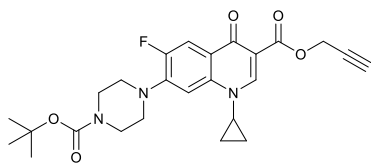
Chemical Formula:  $C_{13}H_{10}O_3$   
Molecular Weight: 214.22 g/mol



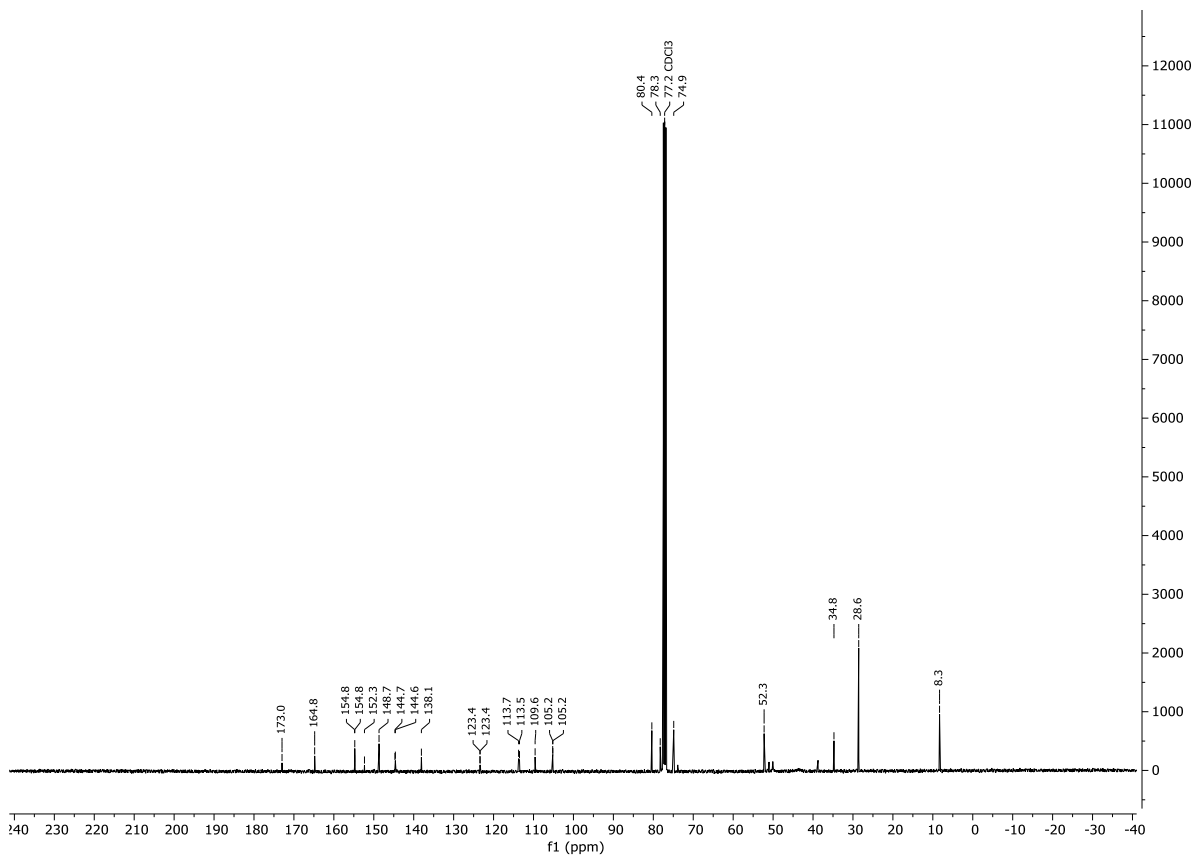
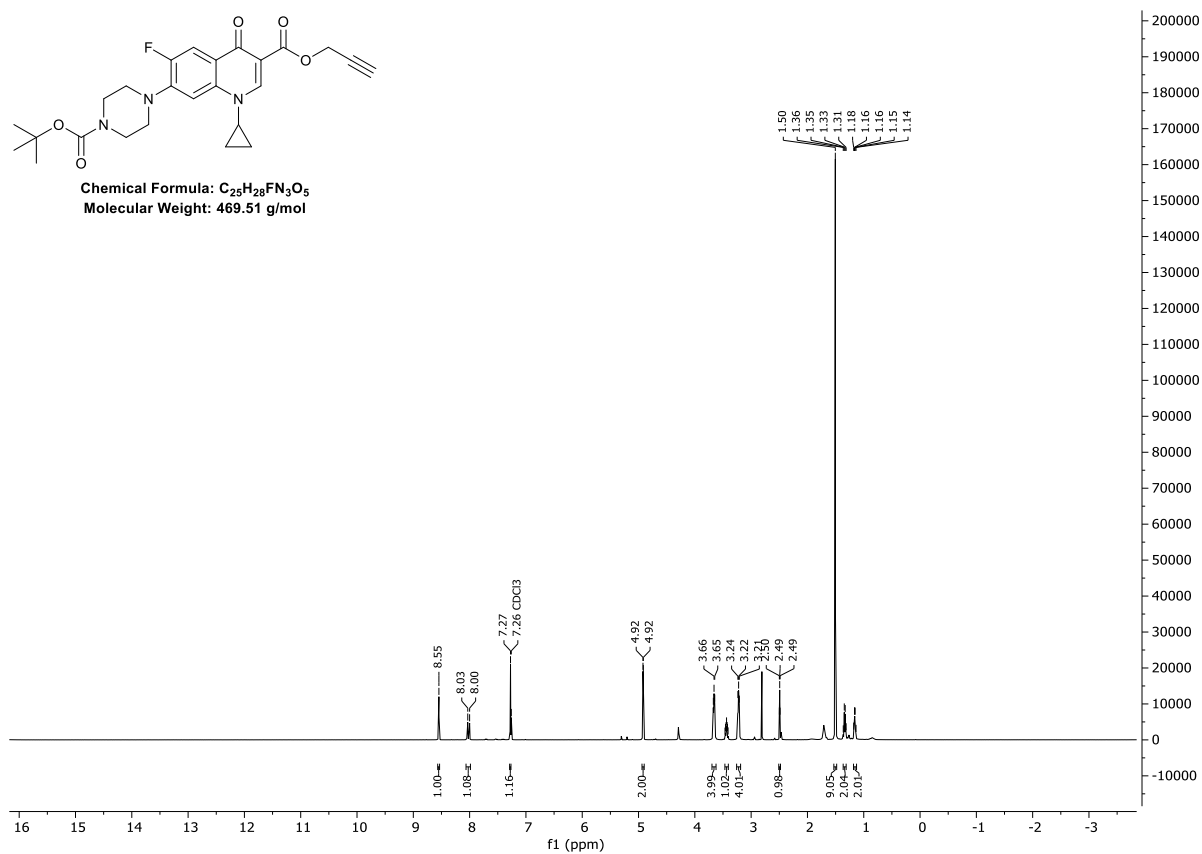


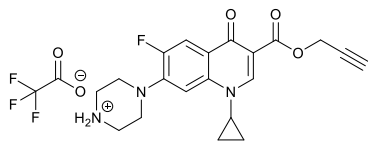
Chemical Formula: C<sub>22</sub>H<sub>26</sub>FN<sub>3</sub>O<sub>5</sub>  
 Molecular Weight: 431.46 g/mol



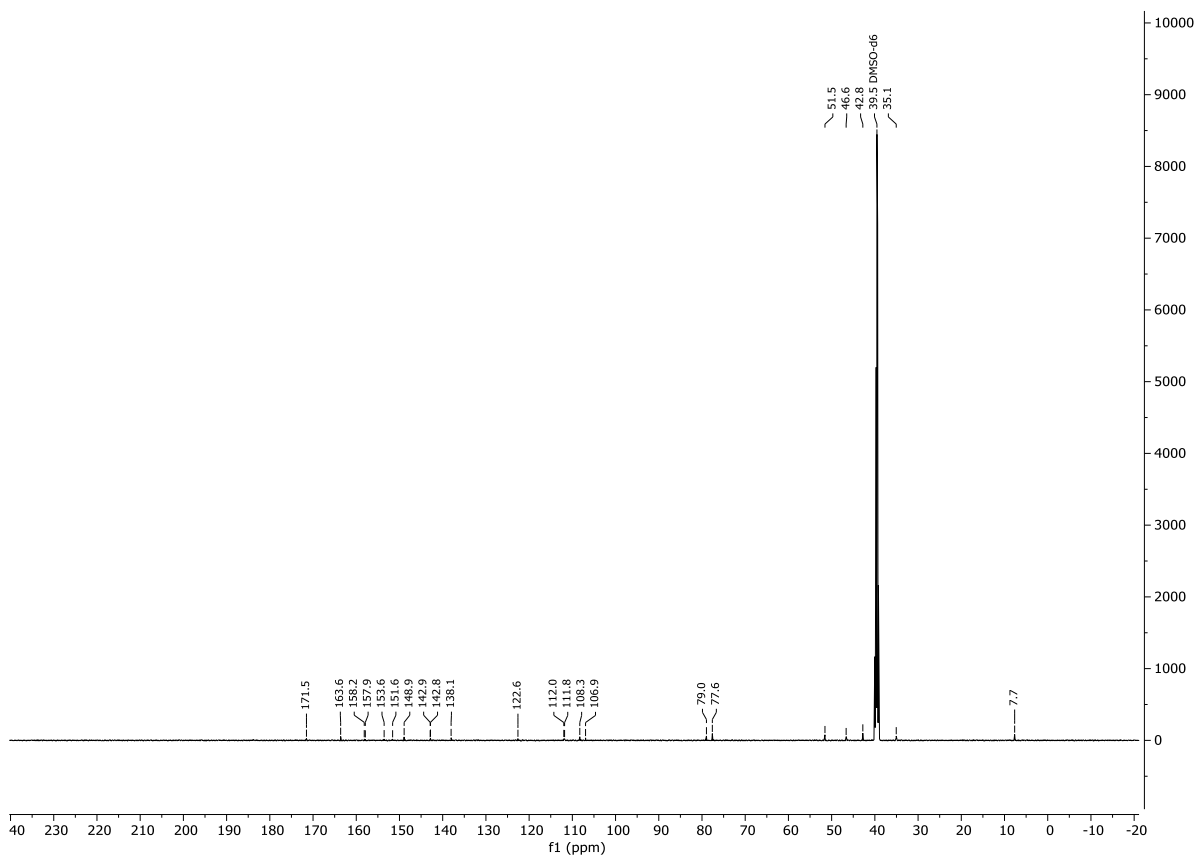
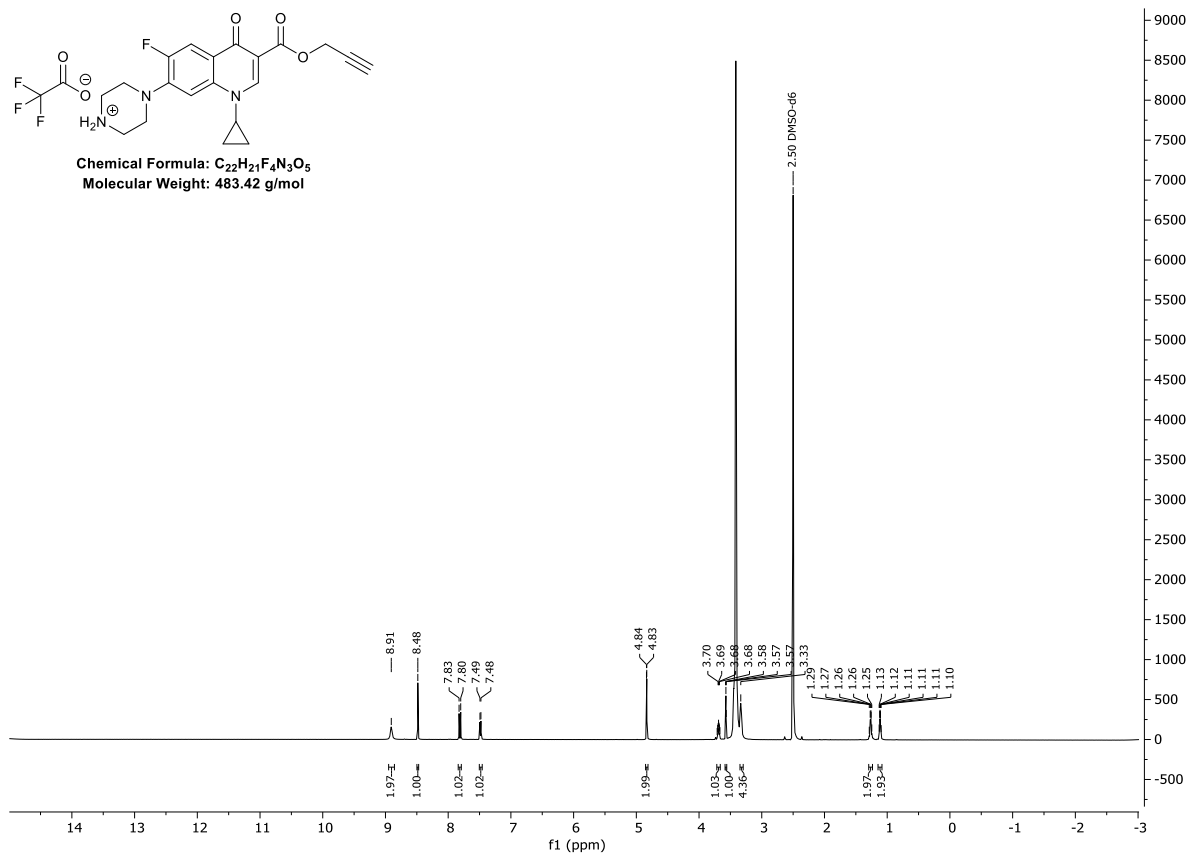


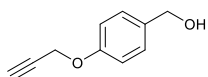
Chemical Formula:  $C_{25}H_{28}FN_3O_5$   
 Molecular Weight: 469.51 g/mol



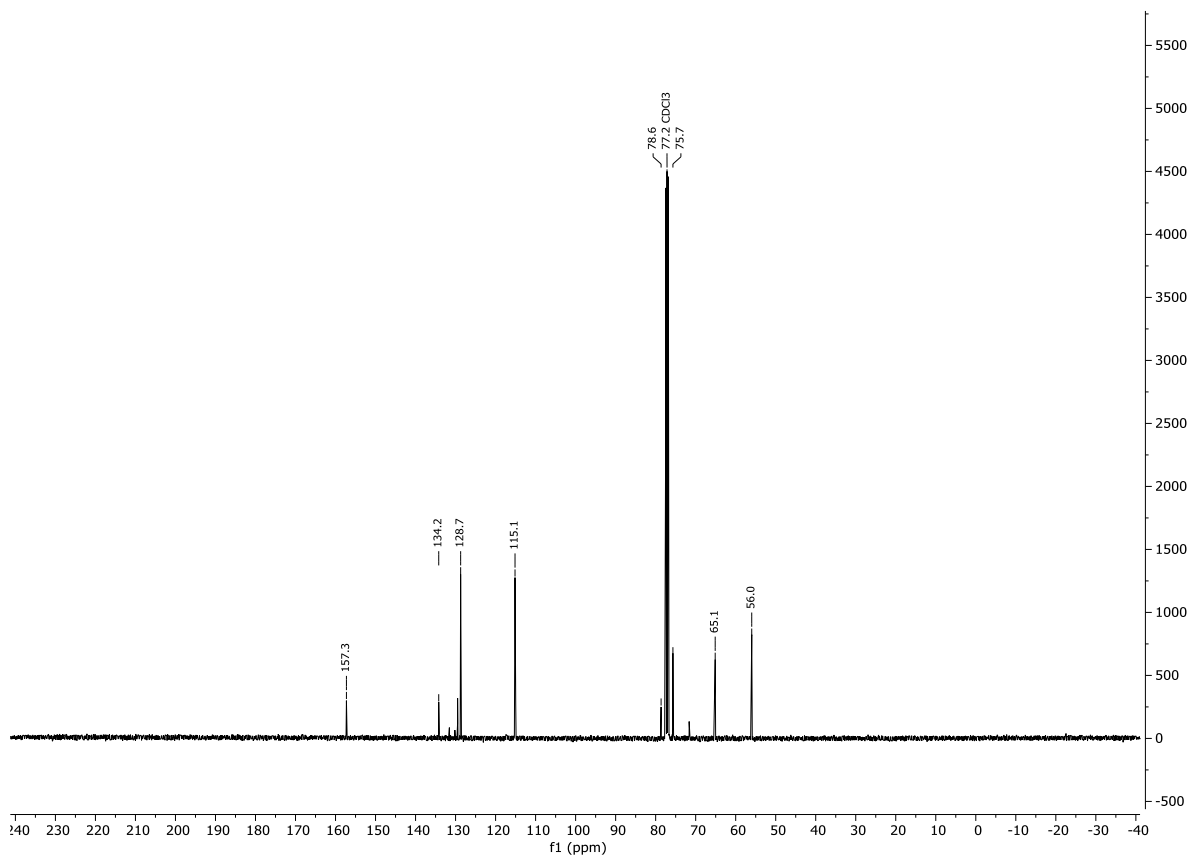
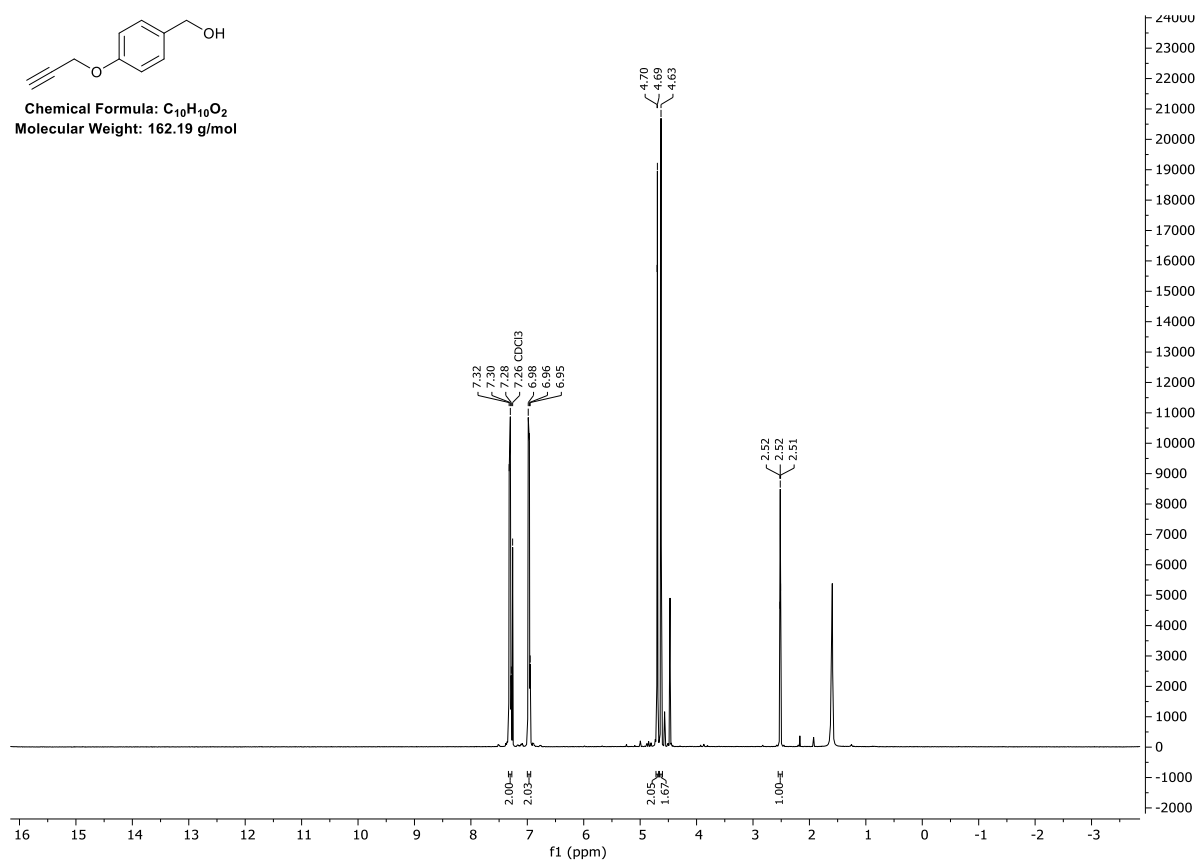


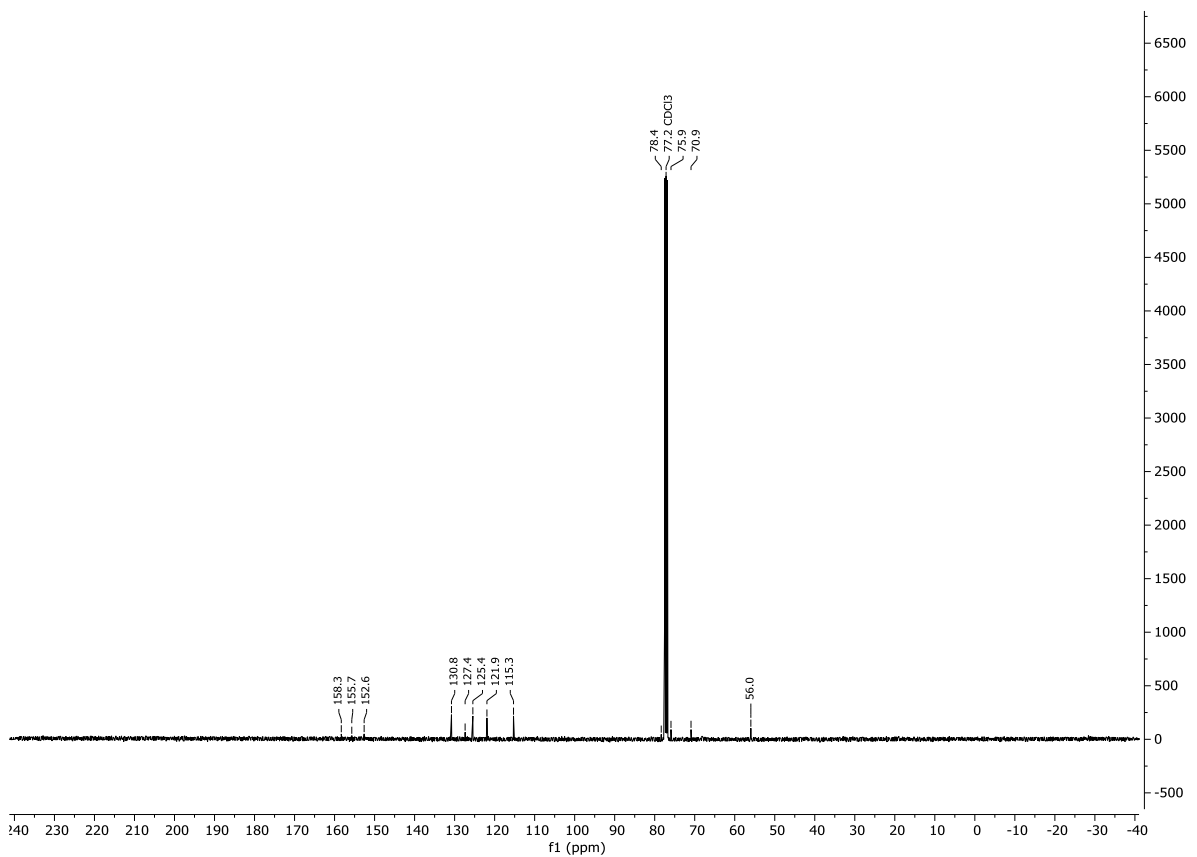
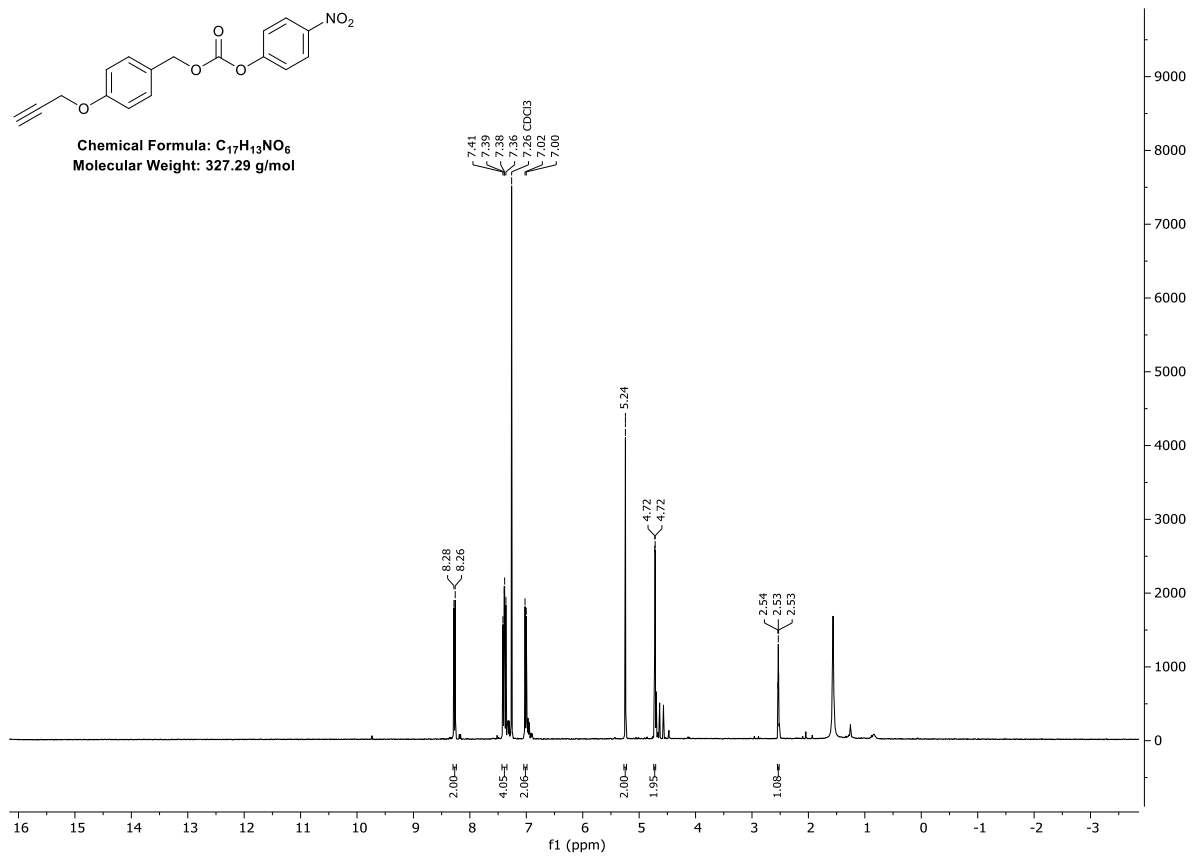
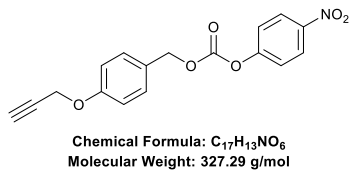
Chemical Formula:  $C_{22}H_{21}F_4N_3O_5$   
 Molecular Weight: 483.42 g/mol

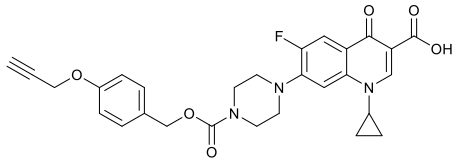




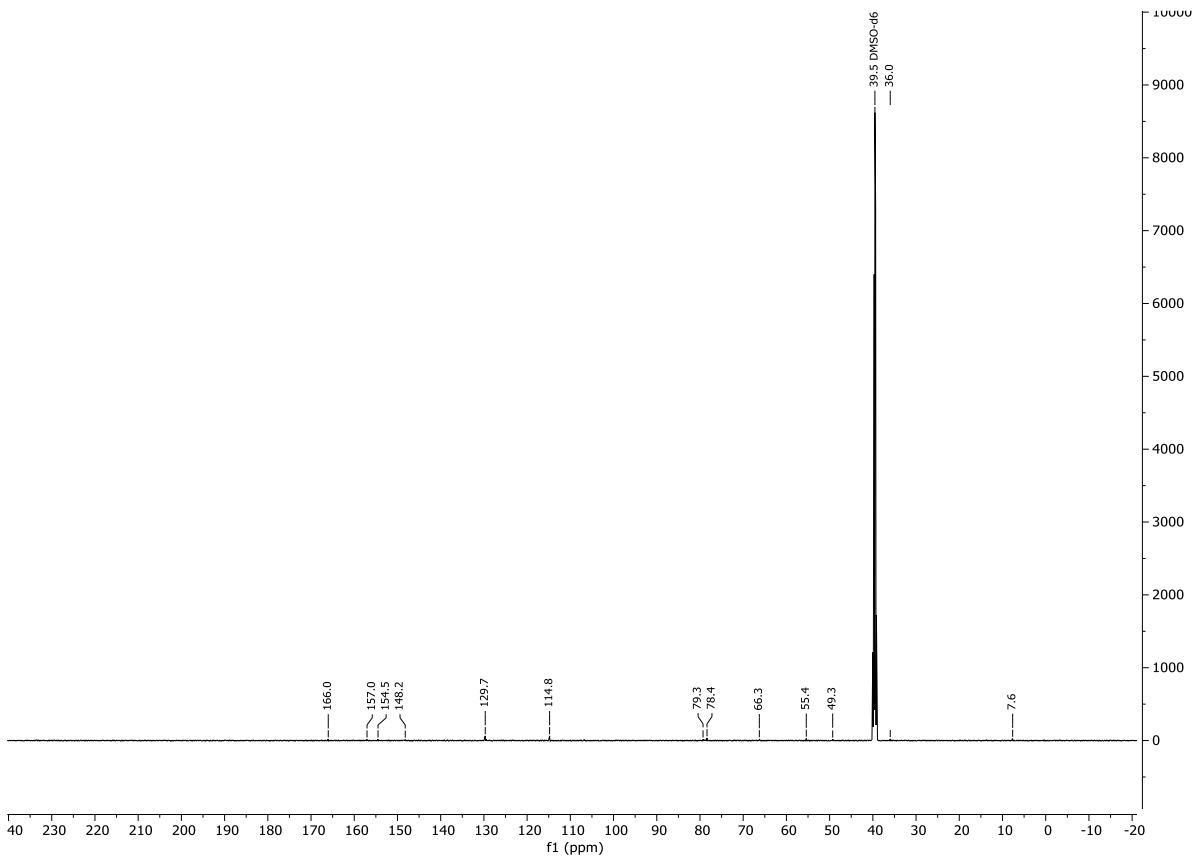
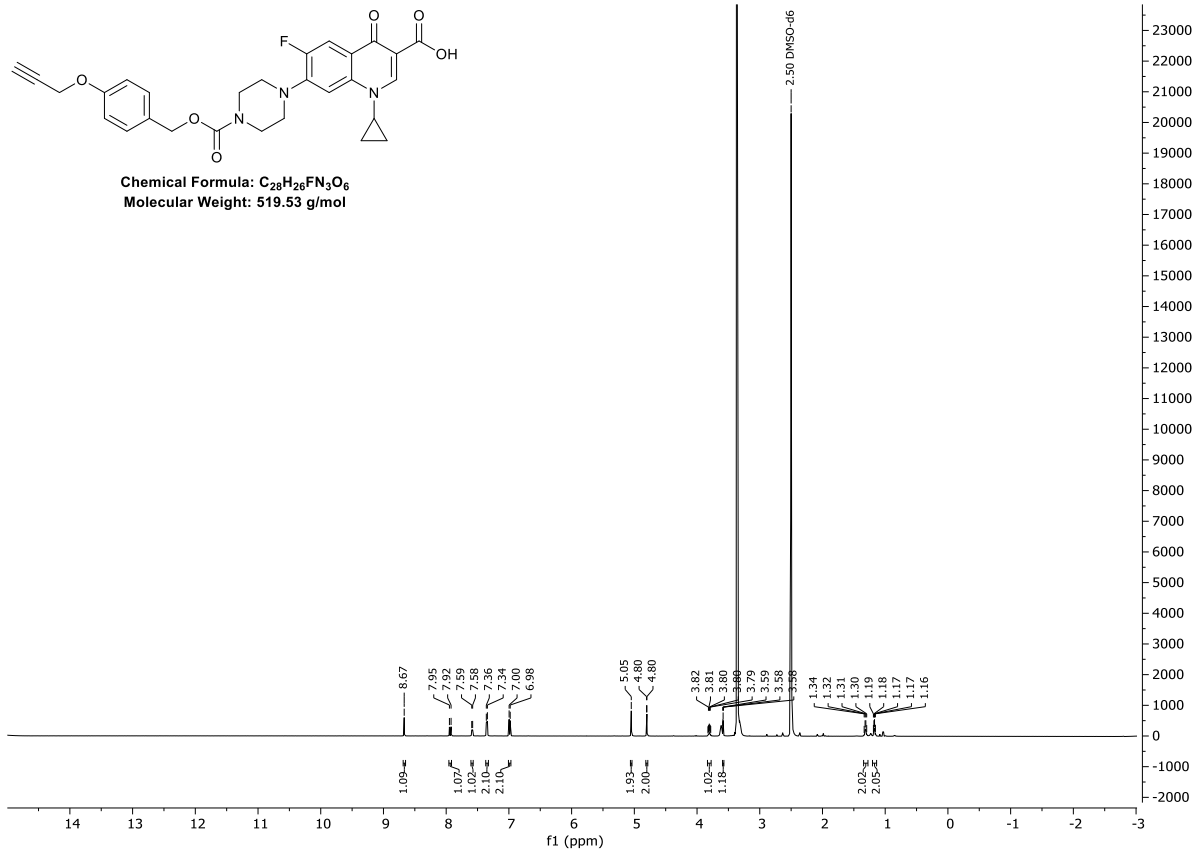
Chemical Formula:  $C_{10}H_{10}O_2$   
Molecular Weight: 162.19 g/mol

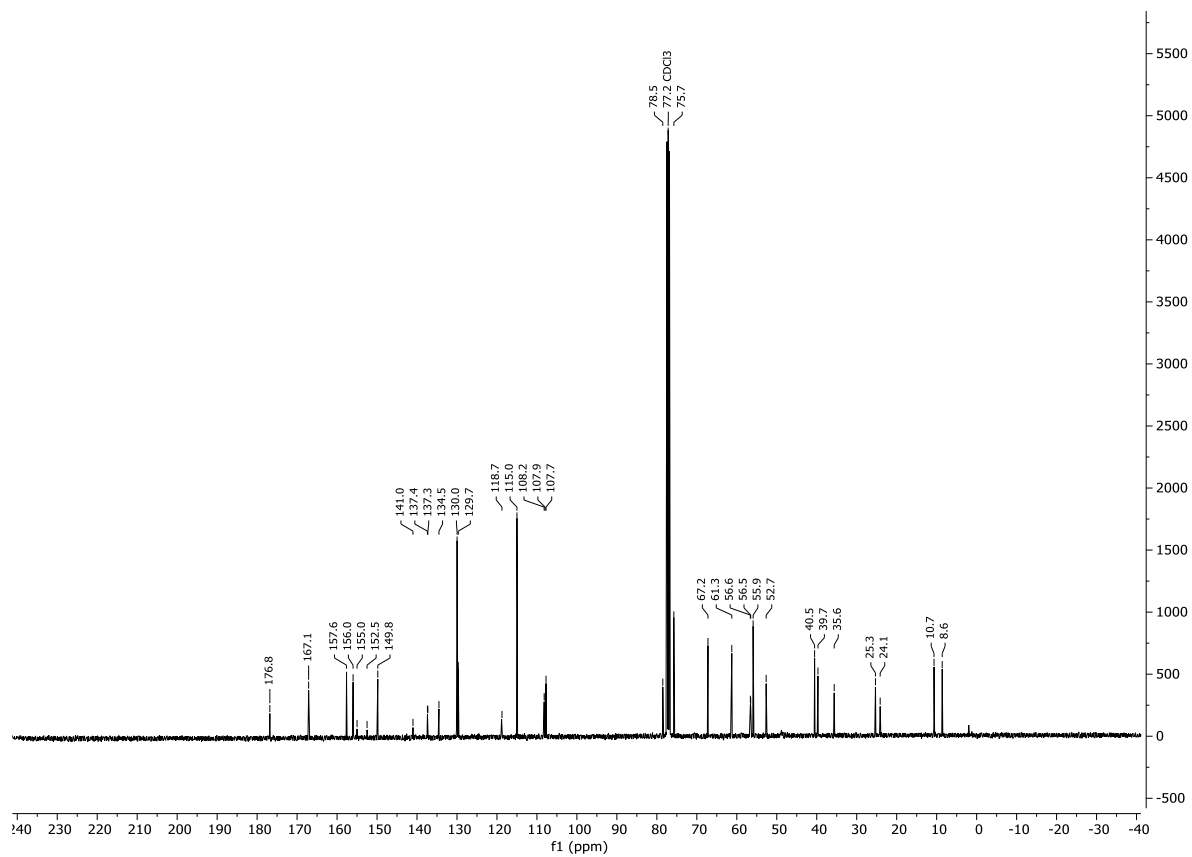
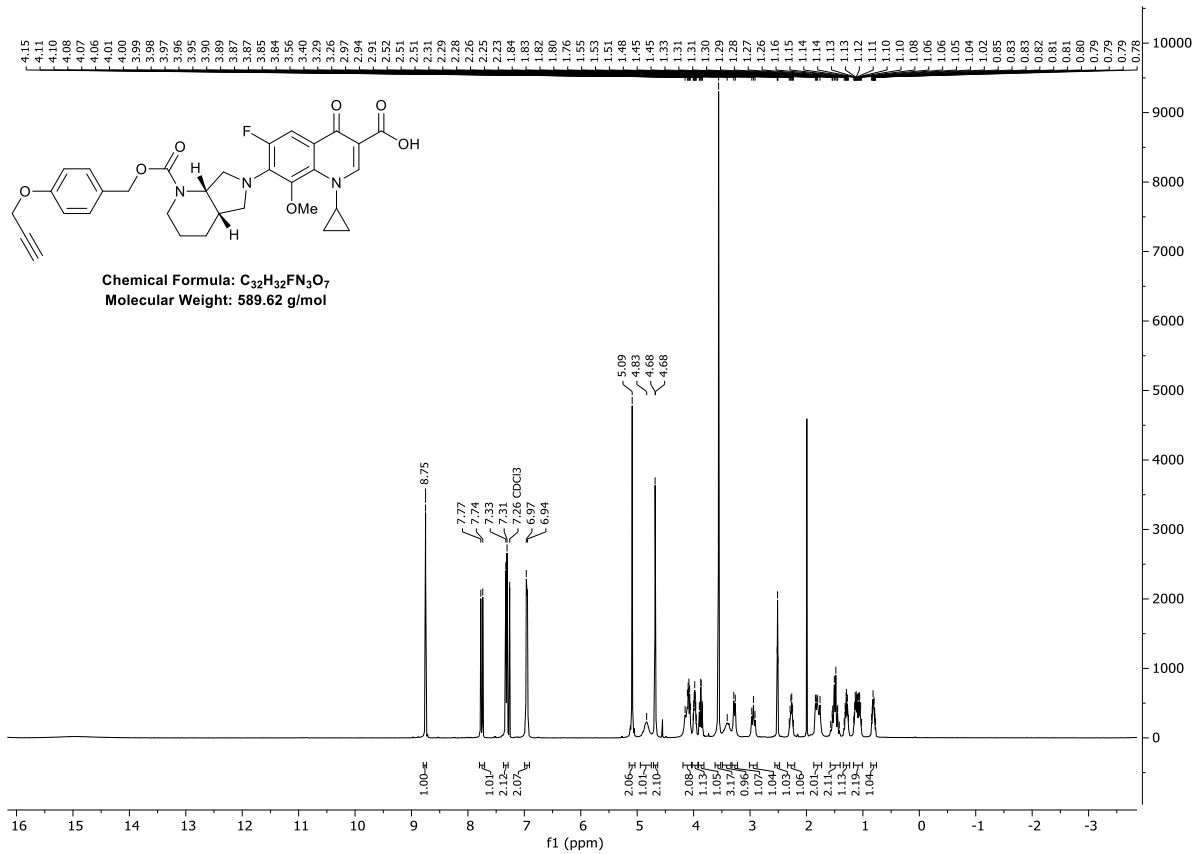






Chemical Formula:  $C_{28}H_{26}FN_2O_6$   
 Molecular Weight: 519.53 g/mol





## 6.6 References

- [59] a.) O. Ciofu, E. Rojo-Molinero, M. D. Macià, A. Oliver, *APMIS* **2017**, *125*, 304-319; b.) O. Ciofu, C. Moser, P. Ø. Jensen, N. Høiby, *Nature Reviews Microbiology* **2022**, *20*, 621-635.
- [120] C. Streu, E. Meggers, *Angewandte Chemie International Edition* **2006**, *45*, 5645-5648.
- [121] N. Li, R. K. V. Lim, S. Edwardraja, Q. Lin, *Journal of the American Chemical Society* **2011**, *133*, 15316-15319.
- [122] B. W. Michel, A. R. Lippert, C. J. Chang, *Journal of the American Chemical Society* **2012**, *134*, 15668-15671.
- [123] C. D. Spicer, T. Triemer, B. G. Davis, *Journal of the American Chemical Society* **2012**, *134*, 800-803.
- [124] D. B. Longley, D. P. Harkin, P. G. Johnston, *Nature Reviews Cancer* **2003**, *3*, 330-338.
- [125] a.) J. T. Weiss, J. C. Dawson, K. G. Macleod, W. Rybski, C. Fraser, C. Torres-Sánchez, E. E. Patton, M. Bradley, N. O. Carragher, A. Unciti-Broceta, *Nature Communications* **2014**, *5*, 3277; b.) A. Unciti-Broceta, E. M. V. Johansson, R. M. Yusop, R. M. Sánchez-Martín, M. Bradley, *Nature Protocols* **2012**, *7*, 1207-1218; c.) J. T. Weiss, C. Fraser, B. Rubio-Ruiz, S. H. Myers, R. Crispin, J. C. Dawson, V. G. Brunton, E. E. Patton, N. O. Carragher, A. Unciti-Broceta, *Frontiers in Chemistry* **2014**, *2*.
- [126] a.) J. T. Weiss, J. C. Dawson, C. Fraser, W. Rybski, C. Torres-Sánchez, M. Bradley, E. E. Patton, N. O. Carragher, A. Unciti-Broceta, *Journal of Medicinal Chemistry* **2014**, *57*, 5395-5404; b.) J. T. Weiss, N. O. Carragher, A. Unciti-Broceta, *Scientific Reports* **2015**, *5*, 9329; c.) B. Rubio-Ruiz, J. T. Weiss, A. Unciti-Broceta, *Journal of Medicinal Chemistry* **2016**, *59*, 9974-9980; d.) T. L. Bray, M. Salji, A. Brombin, A. M. Pérez-López, B. Rubio-Ruiz, L. C. A. Galbraith, E. E. Patton, H. Y. Leung, A. Unciti-Broceta, *Chemical Science* **2018**, *9*, 7354-7361.
- [127] a.) C. Torres-Sánchez, A. M. Pérez-López, M. N. Alqahtani, A. Unciti-Broceta, B. Rubio-Ruiz, *New Journal of Chemistry* **2019**, *43*, 1449-1458; b.) M. Sancho-Albero, B. Rubio-Ruiz, A. M. Pérez-López, V. Sebastián, P. Martín-Duque, M. Arruebo, J. Santamaría, A. Unciti-Broceta, *Nature Catalysis* **2019**, *2*, 864-872.
- [128] A. M. Pérez-López, B. Rubio-Ruiz, T. Valero, R. Contreras-Montoya, L. Álvarez de Cienfuegos, V. Sebastián, J. Santamaría, A. Unciti-Broceta, *Journal of Medicinal Chemistry* **2020**, *63*, 9650-9659.
- [129] M. C. Ortega-Liebana, N. J. Porter, C. Adam, T. Valero, L. Hamilton, D. Sieger, C. G. Becker, A. Unciti-Broceta, *Angew Chem Int Ed Engl* **2022**, *61*, e202111461.
- [130] B. Rubio-Ruiz, A. M. Pérez-López, V. Sebastián, A. Unciti-Broceta, *Bioorganic & Medicinal Chemistry* **2021**, *41*, 116217.
- [131] B. Rubio-Ruiz, A. M. Pérez-López, L. Uson, M. C. Ortega-Liebana, T. Valero, M. Arruebo, J. L. Hueso, V. Sebastian, J. Santamaria, A. Unciti-Broceta, *Nano Letters* **2023**, *23*, 804-811.
- [132] M. A. Plunk, A. Alaniz, O. P. Olademihin, T. L. Ellington, K. L. Shuford, R. R. Kane, *ACS Medicinal Chemistry Letters* **2020**, *11*, 141-146.
- [133] S. S. Magill, J. R. Edwards, W. Bamberg, Z. G. Beldavs, G. Dumyati, M. A. Kainer, R. Lynfield, M. Maloney, L. McAllister-Hollod, J. Nadle, S. M. Ray, D. L. Thompson, L. E. Wilson, S. K. Fridkin, *New England Journal of Medicine* **2014**, *370*, 1198-1208.
- [134] D. Lebeaux, J.-M. Ghigo, C. Beloin, *Microbiology and Molecular Biology Reviews* **2014**, *78*, 510-543.
- [135] Z. Khatoon, C. D. McTiernan, E. J. Suuronen, T.-F. Mah, E. I. Alarcon, *Heliyon* **2018**, *4*, e01067.
- [136] a.) C. Alves, D. Mendes, F. B. Marques, *European Journal of Clinical Pharmacology* **2019**, *75*, 1431-1443; b.) A. A. Bhalodi, T. S. R. van Engelen, H. S. Virk, W. J. Wiersinga, *Journal of Antimicrobial Chemotherapy* **2019**, *74*, i6-i15.
- [137] C. R. Arciola, Y. H. An, D. Campoccia, M. E. Donati, L. Montanaro, *The International Journal of Artificial Organs* **2005**, *28*, 1091-1100.
- [138] D. Baggio, M. R. Ananda-Rajah, *Aust Prescr* **2021**, *44*, 161-164.
- [139] X.-P. Zhang, Q. Yuan, Y.-L. Qi, D.-J. Zheng, Q.-X. Liu, B.-Z. Wang, Y.-S. Yang, H.-L. Zhu, *Spectrochimica Acta Part A: Molecular and Biomolecular Spectroscopy* **2019**, *220*, 117134.

- [140] M. Khodadadi Yazdi, A. Taghizadeh, M. Taghizadeh, F. J. Stadler, M. Farokhi, F. Mottaghitalab, P. Zarrintaj, J. D. Ramsey, F. Seidi, M. R. Saeb, M. Mozafari, *Journal of Controlled Release* **2020**, *326*, 523-543.
- [141] C. Ritter, N. Nett, C. G. Acevedo-Rocha, R. Lonsdale, K. Kräling, F. Dempwolff, S. Hoebenreich, P. L. Graumann, M. T. Reetz, E. Meggers, *Angewandte Chemie International Edition* **2015**, *54*, 13440-13443.
- [142] W. Chen, T. Mohy Ei Dine, S. P. Vincent, *Chemical Communications* **2021**, *57*, 492-495.
- [143] U. Tehler, J. H. Fagerberg, R. Svensson, M. Larhed, P. Artursson, C. A. S. Bergström, *Journal of Medicinal Chemistry* **2013**, *56*, 2690-2694.
- [144] J. B. McManus, N. P. R. Onuska, M. S. Jeffreys, N. C. Goodwin, D. A. Nicewicz, *Organic Letters* **2020**, *22*, 679-683.
- [145] T. L. Bray, M. Salji, A. Brombin, A. M. Pérez-López, B. Rubio-Ruiz, L. C. A. Galbraith, E. E. Patton, H. Y. Leung, A. Unciti-Broceta, *Chemical Science* **2018**, *9*, 7354-7361.

## 7.

# Neocarzilin inhibits cancer cell proliferation via BST-2 degradation resulting in lipid raft trapped EGFR.

---

This chapter is based on:

**J. Braun\***, Y Hu\*, A. T. Jauch\*, T. F. Gronauer, J. Mergner, N. C. Bach, F. R. Traube, S. Zahler, S. A. Sieber, „Neocarzilin inhibits cancer cell proliferation via BST-2 degradation resulting in lipid raft trapped EGFR“, just accepted in *JACS Au*, **2024**.

\* These authors contributed equally to this work.

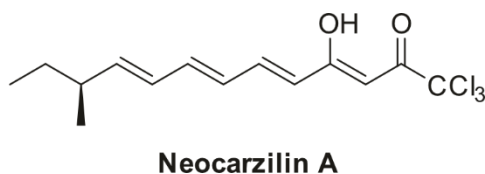
<https://pubs.acs.org/doi/10.1021/jacsau.4c00039>

### Author Contributions

Josef Braun, Yudong Hu, Adrian T. Jauch, Stefan Zahler, and Stephan A. Sieber conceived the project. Thomas F. Gronauer synthesized Neocarzillin A (NCA) and the probe (NC-4). Josef Braun conducted the proteomics experiments. Adrian T. Jauch generated the VAT-1 KO mutants and determined the anti-proliferative and anti-migratory. Yudong Hu generated the BST-2 KO mutants, determined the effect of NCA on the KO mutants, and determined the effect of NCA on BST-2 levels with western blot.

## 7.1 Neocarzinil

Neocarzinil A (NCA) is a polyenone natural product that was isolated from the mycelium of *Streptomyces carzinostaticus* var. I341 in 1992 due to its high antitumor activity (Figure 28).<sup>[146]</sup>



**Neocarzinil A**

**Figure 28.** Structure of neocarzinil A.

Otsuka *et al.* identified a novel type I PKS system responsible for the synthesis of neocarzinil. Further upstream, they identified an open reading frame that encodes a protein closely resembling an FADH<sub>2</sub>-dependent halogenase that could be responsible for the halogenation of neocarzinil precursors.<sup>[147]</sup> Neocarzinil A has potent anti-migratory and anti-proliferative activity in the nanomolar range. With a simplified probe lacking the stereocenter and the methyl group, it has been shown that the synaptic vesicle membrane protein VAT-1, a quinone oxidoreductase, is the target protein responsible for the anti-migratory effect of neocarzinil A.<sup>[148]</sup> The protein target responsible for the anti-proliferative effect of neocarzinil A is still unknown.

## 7.2 Aim and significance of the project

As described in Chapter 2 cancer is a significant cause of death, and novel cancer therapies are urgently needed. Neocarzinil A displays potent anti-proliferative activity against cancer cells, and elucidating the target responsible for this effect might thus unveil a new opportunity to influence the proliferation of cancer cells that can be used to develop novel cancer drugs. This project aimed to identify the protein target of neocarzinil A that is responsible for its anti-proliferative effect.

## 7.3 Results and Discussion

### 7.3.1 Probe labeling in cancer cells

The first generation probe NC-1 was lacking the methyl group and the stereocenter of neocarzinil A. The greatly reduced anti-proliferative effect of NC-1 is an indication for the importance of these features for the anti-proliferative effect of neocarzinil A (Figure 29A). Therefore, Carolin Gleißner (AK Sieber, TUM) and Thomas Gronauer (Sieber lab, TUM) devised the novel probe NC-4 (Figure 29B) including both features and Thomas Gronauer (AK Sieber, TUM) synthesized the novel probe. Data generated by Adrian Jauch (Vollmar lab, LMU) showed that NC-4 retained more of the anti-proliferative activity of NCA in comparison to NC-1 (Figure 29C). This indicates an increased engagement of the anti-proliferative target by NC-4 compared to NC-1.

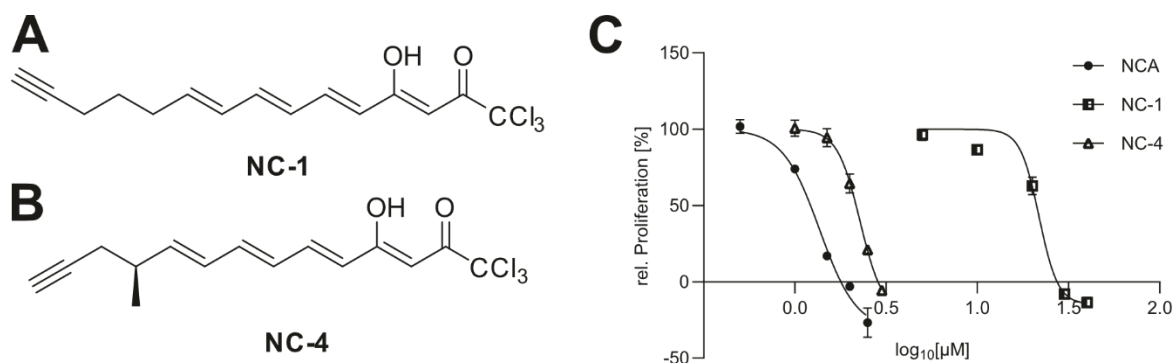


**Figure 29.** New probe NC-4. (A) Structure of the first-generation probe NC-1, (B) Structure of the new probe NC-4 (Synthesized by Tomas Gronauer, Sieber lab, TUM), (C) Antiproliferative activity of NCA, NC-1, and NC-4 in HeLa wt cells was measured by crystal violet staining assay. Cells were treated with the respective compounds at the indicated concentrations for 72 h. Data are presented as mean  $\pm$  SEM ( $n = 3$ ). (Data by Adrian Jauch, Vollmar lab, LMU)

Before NC-4 was applied in quantitative MS-analysis (Figure 30A), it was tested for *in situ* labeling of target proteins in the breast cancer cell line MDA-MB-231, used in the previous study by Gleißner *et al.* The cells were treated with probe concentrations ranging from 50 to 500 nM and were incubated with the probe for 1 h. After cell lysis and click-conjugation to rhodamine azide, the labeled proteome was separated by SDS-PAGE, followed by in-gel fluorescent scanning (Figure 30B, Figure S8A). NC-4 displayed an increased signal-to-noise ratio, high band intensities, and a diverging labeling pattern compared to the first-generation probe NC-1. This indicates a sufficient reactivity of the probe and coverage of so far unidentified targets of neocarzinil A. The concentration, resulting in an optimal labeling intensity for quantitative mass-spectrometry analysis, was 250 nM. Two representative cancer cell lines, HeLa and MDA-MB-231, were selected for probe labeling. The cells were labeled with 250 nM NC-4 for 1 h and lysed. The lysate was conjugated to a biotin azide handle via click-chemistry, the probe-bound proteins were enriched on avidin beads (Figure 30A) and digested with trypsin. LC-MS/MS analysis via label-free quantification (LFQ) revealed a significant enrichment of 12 proteins in MDA-MB-231 and 17 in HeLa cells ( $p$ -value  $< 0.05$ ,  $\log_2$  fold-change  $> 2$ ) (Figure 30C, Figure S8B, Table S1, Table S2). VAT-1, the previously identified target of NCA, was one of the most significantly enriched proteins, confirming the validity of the new probe NC-4. Several additional putative targets could be found among the other significantly enriched proteins. Among these top targets were the anti-viral defense protein BST-2 and heme oxygenase 2 (HMOX2). Due to its reactive cysteine residues, HMOX2 is a frequently encountered target of covalent probes and was previously enriched with NC-1. A competition experiment with an excess of NCA was used to verify the target engagement of the enriched proteins VAT-1, HMOX2, and BST-2 (Figure 30D, Figure S8C, Table S3). Comparing the labeling results of NC-4 in MDA-MB-231 cells and the previously generated labeling results of NC-1 in MDA-MB-231 cells, with decreased anti-proliferative effect, revealed BST-2 as the most prominent difference.<sup>[149]</sup>

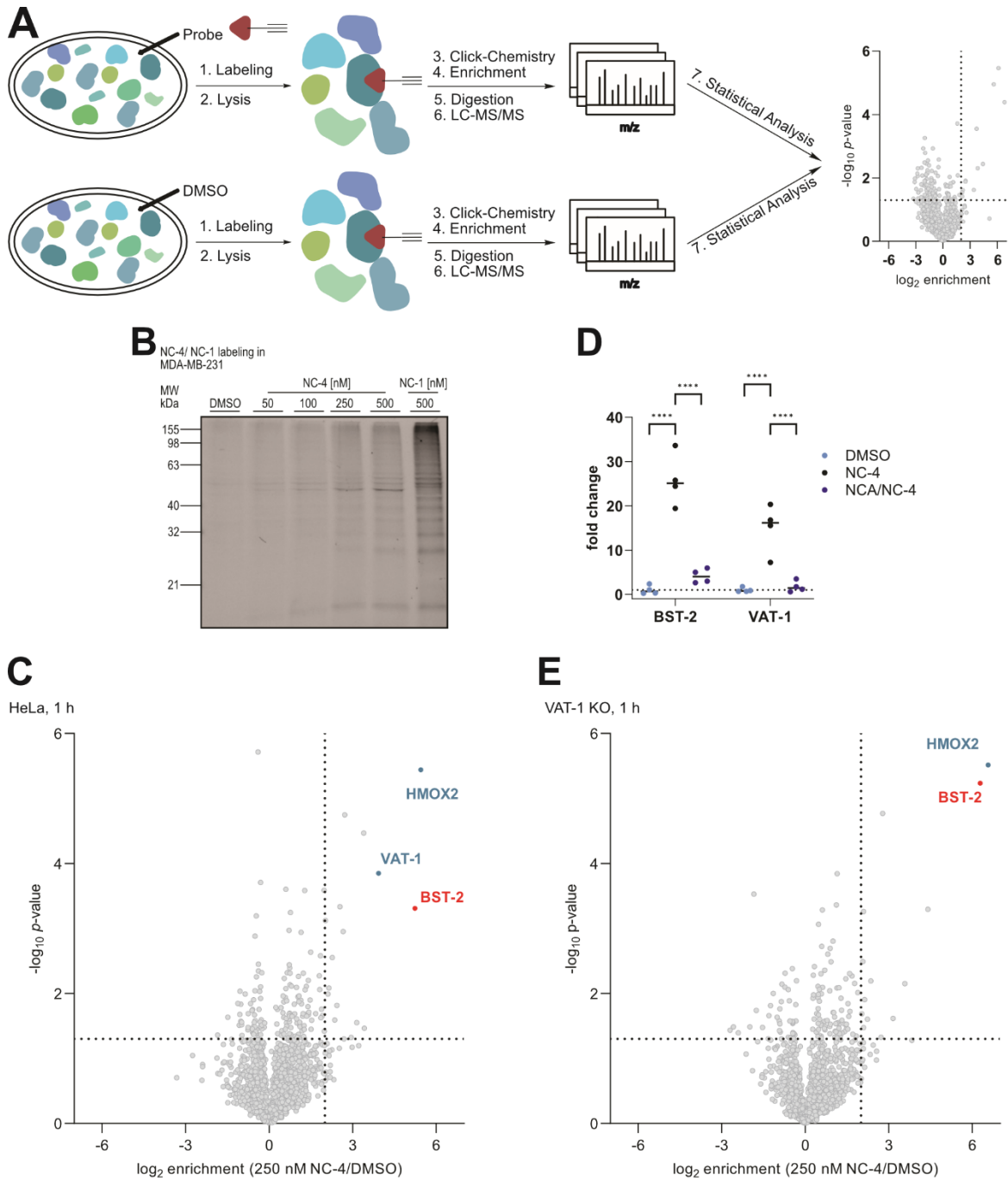


**Figure 30.** Identification of BST-2 as a cellular target of neocarzinil A. (A) Schematic overview of an MS-based *in situ* ABPP experiment, (B) SDS-Page analysis of MDA-MB-231 cells after in situ labeling with NC-4 (Figure S8A), (C) Volcano plot of an LFQ-DDA ABPP experiment of HeLa cells labeled with 250 nM NC-4 for 1 h (n = 4). Proteins fulfilling the criteria  $p\text{-value} < 0.05$  and  $\log_2$  fold-change  $> 2$  were considered significantly enriched (Table S2), (D) Fold change of BST-2 and VAT-1 in an in situ competitive LFQ-DDA ABPP experiment in HeLa cells (n = 4) (for complete MS data: Figure S8C, Table S3). Depicted are the fold changes of VAT-1 and BST-2 upon enrichment with the probe (NC-4) and after saturation of binding sites with NCA and subsequent enrichment with NC-4 (NCA (25  $\mu\text{M}$ )/NC-4 (250 nM)) in comparison to the DMSO control (DMSO). Two-way ANOVA, Dunnett's test, \*\*\*\* $P < 0.0001$ , (E) Volcano plot of in situ LFQ-DDA ABPP experiment in VAT-1 KO cells labeled with 250 nM NC-4 for 1h (n = 4). Proteins fulfilling the criteria  $p\text{-value} < 0.05$  and  $\log_2$  fold-change  $> 2$  were considered significantly enriched (Table S4).

Probe labeling in cells lacking VAT-1 was envisioned to focus on novel targets other than VAT-1. Adrian Jauch (Vollmar lab, LMU) generated HeLa knockout (KO) cells using Crispr-

Cas9 technology.<sup>[150]</sup> The knockout of VAT-1 was confirmed by Western blot (Adrian Jauch, Vollmar lab, LMU) and whole proteome LC-MS/MS analysis (Figure S9). Performing the target analysis experiment described above in these VAT-1 KO cells revealed once more HMOX2 and BST-2 as the most significantly enriched proteins (Figure 30E, Table S4). BST-2 (also called tetherin, CD317, and HM1.24) is a membrane-anchored, cell-surface glycoprotein known for its vital role in the defense against viruses such as dengue. BST-2 is aberrantly expressed in many cancers, and silencing studies have revealed its role in cell proliferation.<sup>[151]</sup> It is reported that BST-2 releases EGFR from lipid rafts, thereby regulating its activity, which is connected to proliferation.<sup>[152]</sup> Therefore, BST-2 seems to be a promising candidate and was selected for target validation studies.

### 7.3.2 BST-2 mediates the anti-proliferative effects of NCA

To further investigate the cellular effects of NCA on BST-2, HeLa BST-2 KO cells were generated by Yudong Hu (Vollmar lab, LMU) via Crispr-Cas9. The knockout was confirmed by Western blot (Yudong HU, Vollmar lab, LMU) and whole proteome LC-MS/MS analysis (Figure S10). In experiments performed by Yudong Hu (Vollmar lab, LMU), the BST-2 KO cells displayed a decreased sensitivity to the anti-proliferative effect of NCA (Figure 31A). They regained their sensitivity to the anti-proliferative effect of NCA upon reconstitution of BST-2 in KO cells via overexpression using a respective plasmid (Figure 31B). This validates BST-2 is a major anti-proliferative target of NCA.

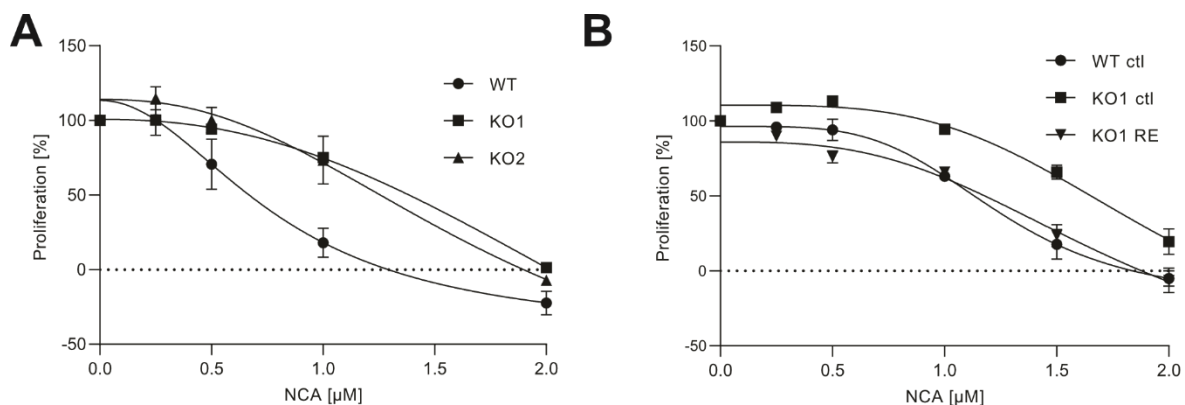


**Figure 31.** BST-2 is the anti-proliferative target of NCA. (A) The anti-proliferative effects of NCA in wt and BST-2 KO HeLa cells were measured using a crystal violet staining assay. Cells were treated with indicated concentrations of NCA for 72 h and data are presented as means  $\pm$  SEM, (n = 3), (B) Anti-proliferative effects of NCA in wt with empty plasmid (ctl) HeLa cells, BST-2 KO with empty plasmid (ctl) HeLa cells, and BST-2 KO HeLa cells with BST-2 reconstitution (RE). Cells were treated with indicated concentrations of NCA for 72 h, and data are presented as means  $\pm$  SEM (n = 3). (Data by Yudong Hu, Vollmar lab, LMU)

### 7.3.3 NCA treatment reduces BST-2 levels via lysosomal degradation

Protein expression levels were monitored via LC-MS/MS whole proteome analysis to study the cellular effects of NCA treatment on the global proteome of HeLa cells, especially BST-2. NCA treatment led to significantly reduced BST-2 levels after 24 h (Figure S11). This raises the question of the mechanism underlying the discovery of decreased BST-2 levels, which, among

others, could be caused by the degradation of BST-2. Yudong Hu (Vollmar lab, LMU) confirmed the reduction of BST-2 levels in whole cells caused by NCA treatment in a concentration-dependent manner by Western blot (Figure 32A). The BST-2 mRNA levels remained constant, indicating that the decrease in BST-2 levels must occur post-transcriptionally (Figure 32B). Following up on this, Yudong Hu (Vollmar lab, LMU) studied different degradation pathways to explain the mechanisms of BST-2 degradation causing the reduction of BST-2 levels after treatment with NCA. She applied inhibitors of different degradation pathways to narrow down possible pathways (proteasome inhibitor MG132 and the autophagosome-lysosome inhibitors bafilomycin A and chloroquine). An inhibition of BST-2 degradation upon cotreatment with the autophagosome-lysosome inhibitors bafilomycin A or chloroquine could be observed, indicating lysosomal degradation of BST-2 (Figure 32C, D). Lysosomal degradation of BST-2 has been reported in the literature as a viral strategy by which the viral protein Vpu induces ubiquitinylation of BST-2 followed by lysosomal removal and subsequent viral entry.<sup>[153]</sup> Yudong Hu (Vollmar lab, LMU) used flow cytometry after antibody staining to measure surface levels and investigate if there is a correlation between the degradation of BST-2 and its abundance in the cell membrane. Surface levels of BST-2 were reduced to a similar degree as total BST-2 levels (Figure 32E).

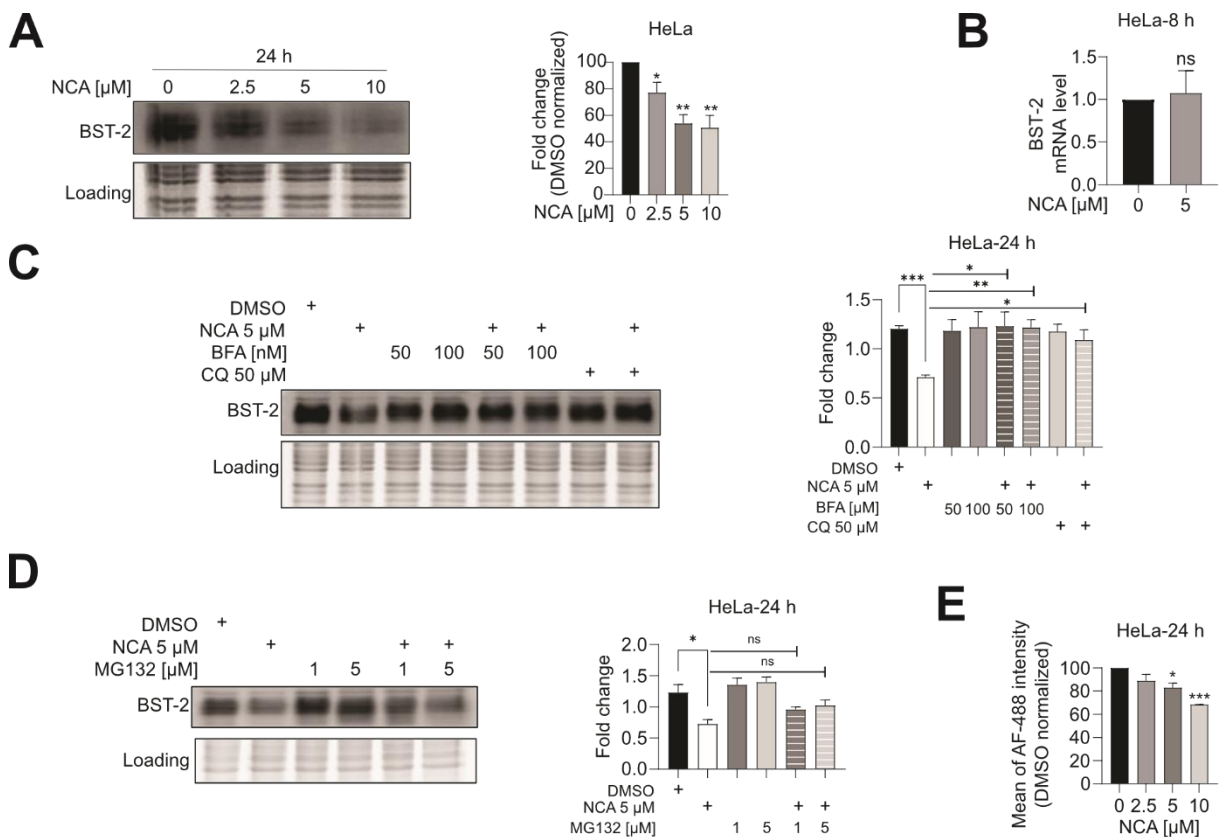


**Figure 32.** NCA promotes BST-2 protein degradation via the lysosomal pathway in a concentration-dependent manner. (A) Western blot analysis of BST-2 protein level in HeLa cells treated with different concentrations of NCA for 24 h. Representative blots of three independent experiments are shown. The amount of BST-2 was normalized to the loading control, and the results were normalized to the DMSO control. Data are presented as means  $\pm$  SEM (n = 3), one-way ANOVA, Dunnett's test, \*\*P<0.002. (B) qPCR analysis of BST-2 mRNA level in DMSO or NCA-

treated HeLa cells for 8 h. Data are presented as means  $\pm$  SEM ( $n = 3$ ), unpaired t-test with Welch's correction,  $nsp > 0.12$ . (C) Western blot analysis of BST-2 protein level in HeLa cells with indicated treatment. HeLa cells were pre-treated with BFA or CQ for 1 h before NCA treatment for 24 h. Representative blots of three independent experiments are shown. The amount of BST-2 was normalized to loading control, and data are presented as means  $\pm$  SEM, ( $n = 3$ ), one-way ANOVA, Dunnett's test,  $*p < 0.033$ . (D) Western blot analysis of BST-2 protein level in HeLa cells with indicated treatment. HeLa cells were pre-treated with MG132 for 1 h before NCA treatment for 24 h. Representative blots of three independent experiments are shown. The amount of BST-2 was normalized to loading control, and data are presented as means  $\pm$  SEM ( $n = 3$ ), one-way ANOVA, Dunnett's test,  $nsp > 0.12$ ,  $**P < 0.002$ . (E) BST-2 surface levels analysis of HeLa cells with indicated concentrations of NCA for 24 h. Data are presented as means  $\pm$  SEM ( $n = 3$ ), one-way ANOVA, Dunnett's test,  $*p < 0.033$ ,  $***P < 0.001$ . Supplementary figure. (Data by Yudong Hu, Vollmar lab, LMU)

## 7.4 Summary and Conclusion

Many natural products are known for targeting more than one protein to increase their biological effects.<sup>[154]</sup> Neocarzinil A is inhibiting migration and proliferation of cancer cells, and it achieves this by addressing multiple target proteins. This thesis used the novel probe NC-4 containing the stereocenter and the methyl group lacking in the first-generation probe NC-1 to identify the protein target responsible for the anti-proliferative effect of neocarzinil A (NCA). The three proteins most prominently enriched by NC-4 from MDA-MB-231, HeLa, and VAT-1 KO cells were the known target VAT-1, the common off-target HMOX2, and the protein BST-2. Bone marrow stromal antigen 2 (BST-2) was the most obvious difference between the proteins enriched with probe NC-1 and those enriched with NC-4. BST-2 is known for its role in the antiviral defense. HeLa BST-2 KO cells were less sensitive to the anti-proliferative effect of NCA. When BST-2 was overexpressed, the KO cells completely regained their sensitivity to the anti-proliferative effect of NCA. NCA treatment of HeLa cells led to a decrease in the cellular levels of BST-2. Co-treatment of cells with NCA and inhibitors of different degradation pathways revealed that the reduction in BST-2 was due to lysosomal degradation of BST-2.

This work reveals BST-2 as the second target of NCA and as the target responsible for the anti-proliferative effect. This indicates that pharmacologically addressing BST-2 in cancer cells would represent a novel and effective treatment option for cancer patients.

## 7.5 Supplementary Information

### 7.5.1 Supplementary Figures S8-12

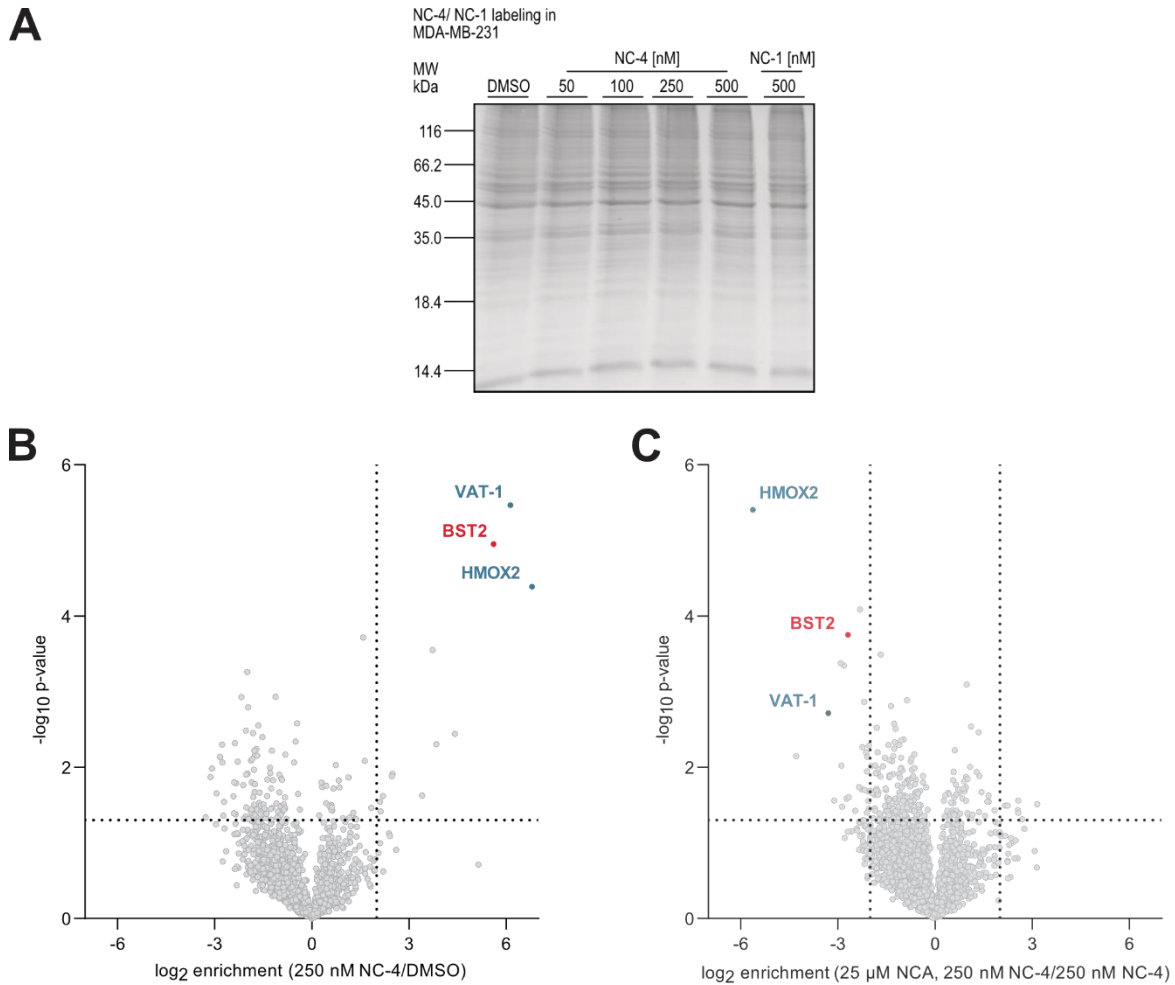


**Figure S8.** *In situ* labeling with NC-4. (A) Coomassie-stained SDS-Page analysis of MDA-MB-231 cells after *in situ* labeling with NC-4 (Figure 30B fluorescent image of gel). (B) Volcano plot of an LFQ ABPP experiment of MDA-MB-231 cells labeled with 250 nM NC-4 for 1 h ( $n = 4$ ) (Table S1). Proteins fulfilling the criteria  $p$ -value  $< 0.05$  and  $\log_2$  fold-change  $> 2$  were considered significantly enriched. (C) Volcano plot of *in situ* competitive LFQ ABPP experiment in HeLa cells (NCA (25  $\mu$ M) /NC-4 (250 nM), 1 h each) ( $n = 4$ ) (Table S3). Proteins fulfilling the criteria  $p$ -value  $< 0.05$  and  $\log_2$  fold-change  $< -2$  were considered significantly outcompeted.

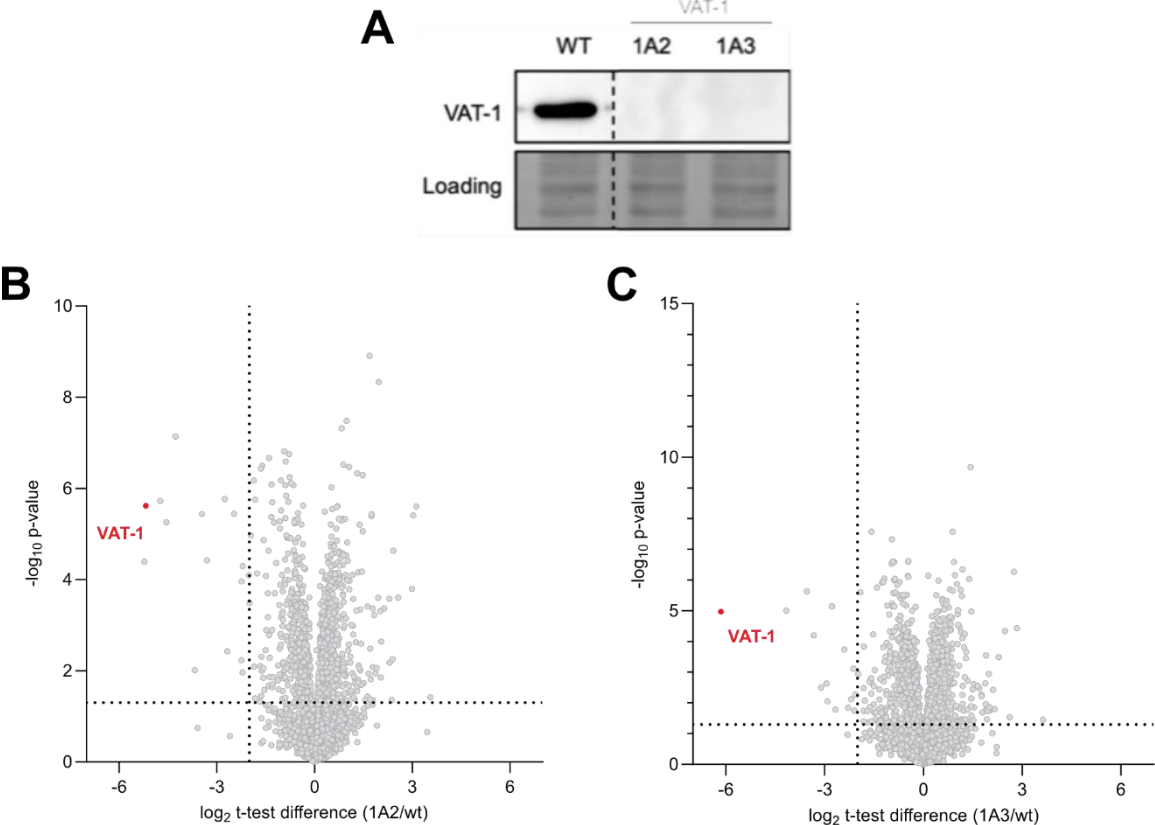


**Figure S9.** Validation of VAT-1 CRISPR knockout clones. (A) Western blot of VAT-1 protein levels in HeLa wt cells and HeLa VAT1 KO clones generated via CRISPR-Cas9 (performed by Adrian Jauch, Vollmar lab, LMU). (B) Volcano plot of whole proteome analysis of KO clone 1A2 compared to HeLa wt cells (n =4). Proteins fulfilling the criteria p-value < 0.05 and log<sub>2</sub> fold-change < -2 were considered significantly downregulated (values for VAT-1 imputed. MS did not detect VAT-1 in KO clones). (C) Volcano plot of whole proteome analysis of KO clone 1A3 compared to HeLa wt cells (n =4). Proteins fulfilling the criteria p-value < 0.05 and log<sub>2</sub> fold-change < -2 were considered significantly downregulated (values for VAT-1 imputed. MS did not detect VAT-1 in KO clones).

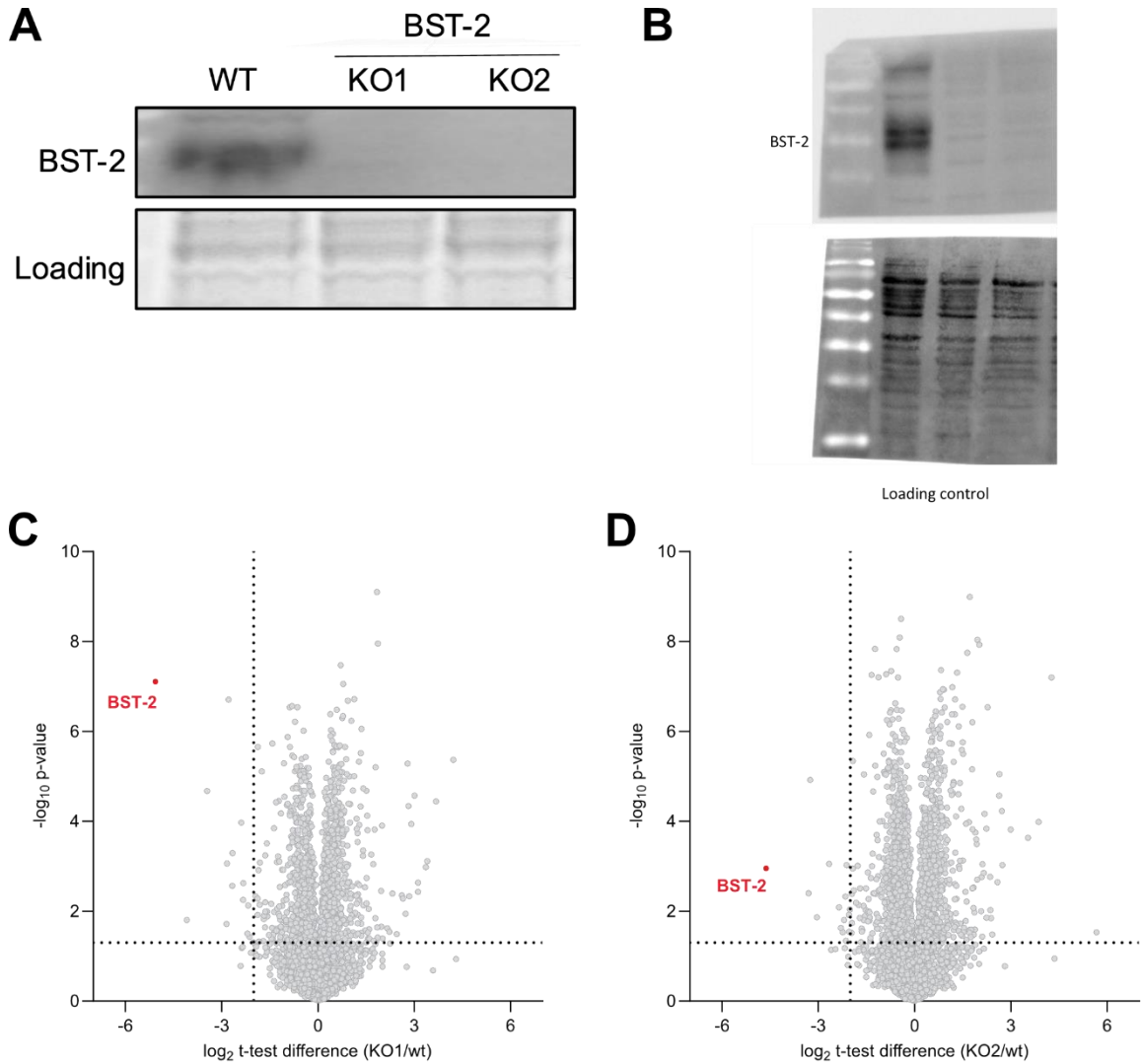


**Figure S10.** Validation of BST-2 CRISPR knockout clones. (A) Western blot of BST-2 protein levels in HeLa wt cells and HeLa BST-2 KO clones generated via CRISPR-Cas9 (performed by Yudong Hu, Vollmar lab, LMU). (B) Uncropped version of Figure S4A (performed by Yudong Hu, Vollmar lab, LMU). (C) Volcano plot of whole proteome analysis of KO clone KO1 compared to HeLa wt cells (n =4). Proteins fulfilling the criteria p-value < 0.05 and log<sub>2</sub> fold-change < -2 were considered significantly downregulated (MS did not detect values for BST-2 imputed. BST-2 in KO clones). (D) Volcano plot of whole proteome analysis of KO clone KO2 compared to HeLa wt cells (n =4). Proteins fulfilling the criteria p-value < 0.05 and log<sub>2</sub> fold-change < -2 were considered significantly downregulated (values for BST-2 imputed. BST-2 was not detected by MS in KO clones).

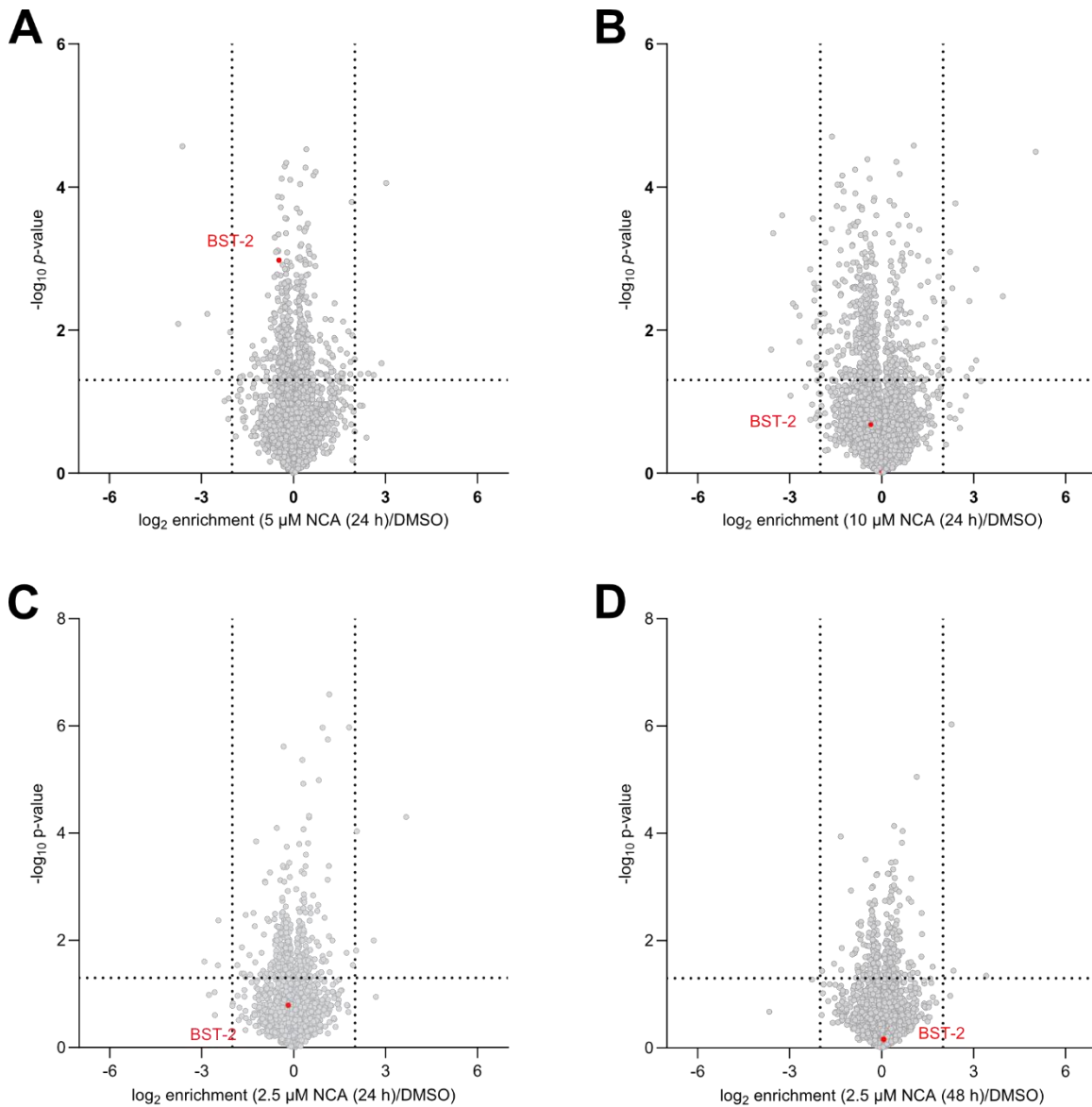


**Figure S11.** Cellular effects of NCA. (A) Volcano plot of whole proteome analysis of HeLa cells treated with 5  $\mu\text{M}$  NCA for 24 h. Proteins fulfilling the criteria  $p\text{-value} < 0.05$  were considered significant. (B) Volcano plot of whole proteome analysis of HeLa cells treated with 10  $\mu\text{M}$  NCA for 24 h. Proteins fulfilling the criteria  $p\text{-value} < 0.05$  were considered significant. (C) Volcano plot of whole proteome analysis of HeLa cells treated with 2.5  $\mu\text{M}$  NCA for 24 h. Proteins fulfilling the criteria  $p\text{-value} < 0.05$  were considered significant. (D) Volcano plot of whole proteome analysis of HeLa cells treated with 2.5  $\mu\text{M}$  NCA for 48 h. Proteins fulfilling the criteria  $p\text{-value} < 0.05$  were considered significant.

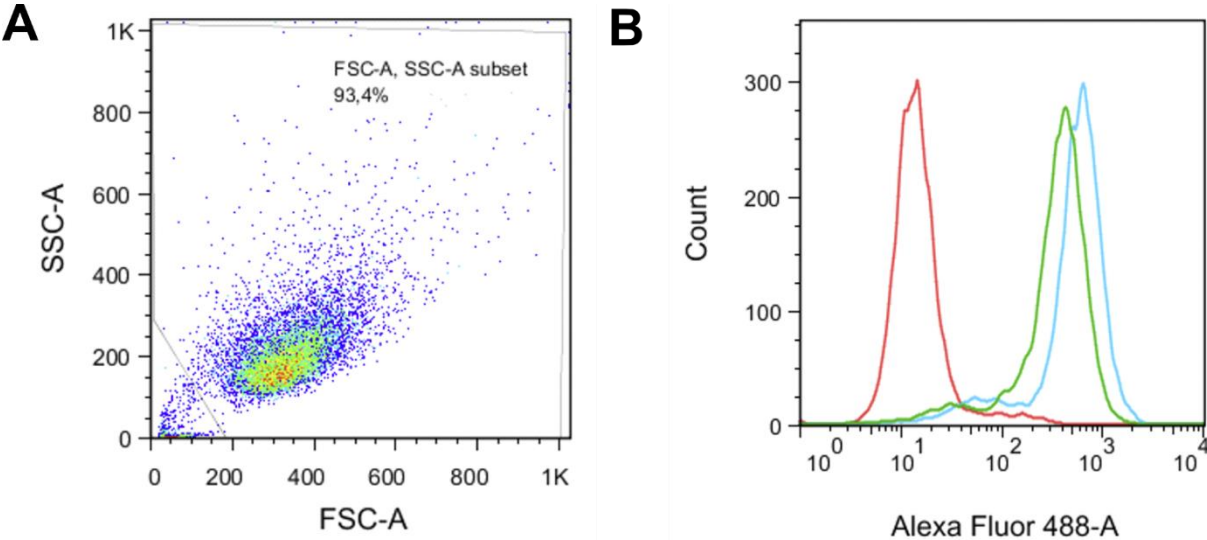


**Figure S12** Quantification of BST-2 surface levels by flow cytometry. (A) Analysis of HeLa cells by flow cytometry. The dot plot shows a homogenous population of cells. The debris in the lower left was gated (light gray frame) and dismissed for analysis. (B) Histogram of the fluorescence intensity of BST-2 on the cell surface (stained with Alexa Fluor 488 coupled antibody). Red: Isotype control, blue: untreated cells, green: cells treated with NCA (10  $\mu$ M, 24 h). (performed by Yudong Hu, Vollmar lab, LMU)

## 7.5.2 Methods

### **Cell culture and cell lines**

MDA-MB-231 cells for proteomic experiments were obtained from DSMZ and cultured in Dulbecco's Modified Eagle's Medium high glucose (DMEM) supplemented with heat-inactivated 10% (v/v) fetal bovine serum (FBS) and 2 mM L-glutamine. Cells were grown at 37 °C and 5% CO<sub>2</sub>. HeLa cells were obtained from DSMZ and grown in DMEM supplemented with 10% (v/v) FBS and 2 mM L-glutamine. Cells were cultured at 37 °C with 5% CO<sub>2</sub> in a humidified incubator and were routinely tested for mycoplasma contamination.

### ***In situ* labeling in human cells**

Cells for analytical labeling were seeded in 6-well plates, and cells for preparative labeling were seeded in 15 cm dishes. They were treated at 90% confluence with the probe (NC-1 or NC-4, stock solution in DMSO, 0.1% end concentration of DMSO in Medium) for 1 h at different concentrations (50 – 500 nM). For competition experiments, cells were preincubated with 25 µM of the natural product neocarzilin A (stock solution in DMSO, 0.1% end concentration of DMSO in Medium) for 1 h. The natural product solution was removed and replaced by 250 nM NC-4 (stock solution in DMSO, 0.1% end concentration of DMSO in Medium) for 1 h. The medium was removed, and the cells rinsed with cold PBS (1 mL for 6-well plates and 10 mL for 15 cm dishes). PBS was added to the cells, and they were scraped off and pelletized for 10 min at 600 rpm, 4 °C. The supernatant was aspirated. Cell lysis was performed using lysis buffer (1%(v/v) NP40 and 1% (w/v) sodium deoxycholate in PBS, 100 µL for pellets from 6-well plates and 1 mL for pellets from 15 cm dishes) at 4 °C for 15 min. Soluble and insoluble fractions have not been separated.

### **Analytical *in situ* labeling**

Whole cell lysate was applied for click chemistry. Click chemistry was performed. With TCEP (52 mM stock in ddH<sub>2</sub>O, final conc. 1.0 mM), TBTA ligand (1.667 mM stock in DMSO/tBuOH = 1/4, final conc. 0.1 mM), CuSO<sub>4</sub> (50 mM stock in ddH<sub>2</sub>O, final conc. 1.0 mM), rhodamine-azide (10 mM stock in DMSO; base click; Rh-N<sub>3</sub>, final conc. 0.2 mM). The reaction was incubated at room temperature for 1 h and stopped by addition of 100 µL 2 x SDS loading buffer (63 mM Tris-HCl, 2% (v/v) glycerol, 139 mM sodium dodecyl sulfate (SDS), 0.0025% (v/v) Bromophenol blue, 5% (v/v) 2-mercaptoethanol). For gel electrophoresis, 50 µL were applied per gel lane on an SDS-PAGE gel (15.0% acrylamide). A Fujifilm LAS 4000 luminescent image analyzer equipped with a Fujifilm LAS-300 camera, a Fujinon VRF43LMD3 lens, and a 575DF20 filter was used for the detection of fluorescence.

### ***In situ* preparative labeling label-free quantification**

For preparative labeling, cells were incubated with 25  $\mu$ M NCA or DMSO for 1 h and subsequently with 250 nM NC-4 or DMSO for 1 h. Whole cell lysate was used. Protein amount after lysis was determined by BCA assay (Roti Quant, Roth) and adjusted to a final concentration of 1  $\mu$ g in 1 mL. Click chemistry was performed with 0.20 mM Biotin-PEG3-N<sub>3</sub> (10 mM stock in DMSO, final conc. 0.2 mM, *Jena Bioscience*), TCEP (52 mM stock in ddH<sub>2</sub>O, final conc. 0.52 mM), TBTA ligand (1.67 mM stock in DMSO/*t*BuOH = 1/4, final conc. 0.05 mM) and CuSO<sub>4</sub> (50 mM stock in ddH<sub>2</sub>O, final conc. 0.5 mM). Click reaction was performed for 1 h at room temperature, and MS sample preparation was performed as described before.<sup>[149]</sup> Proteins were precipitated with 10 mL MS-grade acetone at -80 °C. The precipitate was centrifuged down and washed with 500  $\mu$ L MS-grade methanol twice. Enrichment was performed on 50  $\mu$ L Pierce™ avidin-agarose beads (Thermo Scientific) in 0.2% SDS in PBS for 1 h at room temperature. The beads were washed three times with 0.2% SDS in PBS and three times with PBS. The beads were resuspended in 200  $\mu$ L denaturation buffer (7 M urea, 2 M thiourea in 20 mM Hepes, pH 7.5). Reduction and alkylation of the samples were performed at room temperature with DTT (1 mM) for 45 min, IAA (5.5 mM) for 30 min, and DTT (4 mM) for 30 min. The samples were digested with 1  $\mu$ L Lys-C (0.5 mg/mL, Fujifilm) 2 h at room temperature, 600  $\mu$ L 50 mM TEAB buffer added, and digested with 1.5  $\mu$ L Trypsin (0.5 mg/mL, Promega) overnight at 37 °C. 8  $\mu$ L LC/MS-grade formic acid (FA) was added to stop the digest and the samples were desalted with Sep-Pak® C18 1 cc Vac cartridges (Waters Corp.). The columns were washed with MS-grade acetonitrile and 0.1% trifluoroacetic acid (TFA). Samples were loaded on the cartridges, washed with 0.1% TFA in MS-grade water, 0.5% FA in MS-grade water, and eluted with elution buffer (20% H<sub>2</sub>O, 0.5% FA in acetonitrile). Samples were lyophilized, stored at -80 °C, and reconstituted in 30  $\mu$ L 1% FA for MS/MS measurements.

### **Whole proteome analysis**

Cells for whole proteome analysis were seeded in 15 cm dishes. They were treated at 90% confluence with the natural product (NCA stock solution in DMSO, 0.1% end concentration of DMSO in Medium) for different time periods (24 h and 48 h) at various concentrations (2.5  $\mu$ M and 5  $\mu$ M). The medium was removed, and the cells rinsed with cold PBS (10 mL). PBS was added to the cells, and they were scraped off and pelletized for 10 min at 600 rpm, 4 °C. The supernatant was aspirated. Cell lysis was performed using lysis buffer (1%(v/v) NP40 and 1% (w/v) sodium deoxycholate in PBS, 1 mL) at 4 °C for 15 min. Soluble and insoluble fractions have not been separated. The samples were adjusted after BCA to 200  $\mu$ L, 0.5 mg/mL protein, and proteins were precipitated by adding MS-grade acetone (1 mL, -80 °C). The precipitate was centrifuged down and washed with 500  $\mu$ L MS-grade methanol twice. The proteins were resuspended in 200  $\mu$ L in denaturation buffer (7 M urea, 2 M thiourea in 20 mM Hepes, pH

7.5). Reduction and alkylation of the samples were performed with TCEP (5 mM) for 1 h at 37 °C and with IAA (10 mM) for 30 min and DTT (10 mM) for 30 min at room temperature. The samples were digested with 1 µL Lys-C (0.5 mg/mL, Fujifilm) for 4 h at room temperature, 600 µL 50 mM TEAB buffer added, and digested with 2 µL Trypsin (0.5 mg/mL, Promega) overnight at 37 °C. The digest was stopped by adding 10 µL LC/MS-grade formic acid (FA), and the samples were desalted with Sep-Pak® C18 1 cc Vac cartridges (Waters Corp.). The cartridges were washed with MS-grade acetonitrile and 0.1% trifluoroacetic acid (TFA) in MS-grade water. Samples were loaded on the cartridges, washed with 0.1% TFA, 0.5% FA in MS-grade water, and eluted with elution buffer (20% H<sub>2</sub>O, 0.5% FA in acetonitrile). Samples were lyophilized and stored at -80 °C.

### **MS/MS measurement Orbitrap Fusion**

Samples were dissolved in 1% FA in MS-grade water, sonicated for 15 min, and filtered through a 0.22 µm Ultrafree-MC® centrifugal filter (Merck, UFC30GVNB) equilibrated with 1% FA MS-grade water. Samples were analyzed by LC-MS/MS using an UltiMate 3000 nano HPLC system (Dionex) equipped with an Acclaim C18 PepMap100 (75 µm ID x 2 cm) trap and a 25 cm Aurora Series emitter column (25 cm x 75 µm ID, 1.6 µm FSC C18) (Ionopticks) (column oven set to 40 °C) coupled to an Orbitrap Fusion (Thermo Fisher) in EASY-spray setting. Samples were loaded on the trap column with a flow rate of 5 µL/min with 0.1% TFA in MS-grade water and washed for 10 min. The peptides were transferred onto the separation column. They were separated using a 132 min gradient (buffer A: 0.1% FA in MS-grade water, buffer B: 0.1% FA in Acetonitrile, gradient: to 5% buffer B in 7 min, to 22% buffer B in 105 min, to 35% buffer B in 10 min and 90% buffer B in 10 min. The column was washed with 90% buffer B for 10 min and reequilibrated with 5% buffer B for 10 min). Peptides were ionized using a nanospray source at 1.7-1.9 kV at a transfer capillary temperature of 275 °C. The instrument was used in top-speed data-dependent mode, and the cycle time between master scans was set to 3 seconds. MS full scans were recorded at a resolution of R = 120,000 and an automatic gain control (AGC) ion target value of  $2 \times 10^5$  in a scan range of 300 – 1500 m/z with a maximum injection time of 50 ms and an RF lens amplitude of 60%. Precursors with intensities higher than  $5 \times 10^3$  and charge states between 2 and 7 were selected for fragmentation in the higher-energy collisional dissociation (HCD) cell (30% collision energy). MS<sup>2</sup> scans were recorded in the ion trap operating in a rapid scan mode. The isolation window was set to 1.6 m/z. For enriched samples, the AGC target was set to  $1 \times 10^4$  with a maximum injection time of 100 ms, and for complex samples, the AGC target of  $1 \times 10^4$  with a maximum injection time of 35 ms was applied.

## Bioinformatics and statistics

Processing of MS raw data was done with the software MaxQuant version 1.6.2.10. For the identification of peptides, MS/MS spectra were searched against the UniProt database for Homo sapiens (taxon identifier: 9606, downloaded on 30.09.2020, canonical).<sup>[155]</sup> For MaxQuant, mostly default settings were used (trypsin/P as digest enzyme, max. 2 missed cleavages, oxidation (M) and protein N-term acetylation as variable modifications, carbamidomethylation (C) as fixed modification, min. peptide length 7). The main search was conducted with 4.5 ppm for precursor mass tolerance and 0.5 Da for fragment mass tolerance. Protein identification was performed with the following settings: PSM FDR 0.01, Protein FDR 0.01, min. Razor + unique peptides: 2, razor protein FDR enabled, second peptides enabled. The “match between run” option (0.7 min match and 20 min alignment time windows) was enabled. Label-free quantification (LFQ) was used for all samples. The built-in LFQ algorithm in MaxQuant software (MaxLFQ)<sup>[156]</sup> was used with a minimal ratio count of 1. The mass spectrometry proteomics data have been deposited to the ProteomeXchange Consortium<sup>[157]</sup> via the PRIDE9 partner repository with the dataset identifier PXD050453.

The statistical analysis of the resulting data was done with the Perseus software<sup>[158]</sup> (version 1.6.5.0). Normalized LFQ intensities from the proteinGroups.txt table were used for further analysis. First, the data was filtered by “filtering by categorical columns,” namely the columns “identified by site,” “reverse,” and “contaminants.” Log<sub>2</sub> transformation and categorical annotation of treated samples and control were performed. The data was filtered against 70% of valid values in at least one group. Missing values were imputed from a normal distribution (width 0.3, downshift 1.8, for the total matrix). Two-sample Student’s t-tests were performed, including permutation-based false discovery rate correction (FDR = 0.05). Volcano plots were generated by plotting the student’s t-test difference (treated/control) against the t-test p-value (treated/control). Proteins with a p-value of < 0.05 and an enrichment factor of > 4 ( $\log_2(x) = 2$ ) were considered as significantly enriched.

## 7.5.3 Supplementary Tables

**Table S1.** Proteins matching the criteria (p-value < 0.05, log2 fold-change > 2) of LFQ ABPP experiment with 250 nM NC-4 in MDA-MB-231 (1 h) (Volcano plot Figure S2B).

protein name	gene name	enrichment	p-value	sequence coverage [%]
Heme oxygenase 2	HMOX2	6.79	4.39	55.7
Vesicle amine transport protein 1 homolog	VAT1	6.13	5.47	41.7
Bone marrow stromal antigen 2	BST2	5.61	4.95	18.3
Reticulon-4	RTN4	4.41	2.44	14.9
Endonuclease domain-containing 1 protein	ENDOD1	3.84	2.31	21.2
Cytochrome b5 type B	CYB5B	3.72	3.55	45.2
Protein DBF4 homolog B	DBF4B	3.41	1.62	6.5
Zinc finger protein 185	ZNF185	2.49	1.91	34.4
Reticulon-1	RTN1	2.47	1.88	3.6
Transmembrane 9 superfamily member	TM9SF2	2.20	1.62	5.6
Cysteine dioxygenase type 1	CDO1	2.13	1.41	7.5
Prenylcysteine oxidase 1	PCYOX1	2.10	1.54	9.3

**Table S2.** Proteins matching the criteria (p-value < 0.05, log<sub>2</sub> fold-change > 2) of LFQ ABPP experiment with 250 nM NC-4 in HeLa (1h) (Volcano plot Figure 2B).

protein name	gene name	enrichment	p-value	sequence coverage [%]
Heme oxygenase 2	HMOX2	5.45	5.44	46.8
Bone marrow stromal antigen 2	BST2	5.23	3.32	18.3
Vesicle amine transport protein 1 homolog	VAT1	3.93	3.85	48.9
Prostaglandin E synthase	hCG_30600	3.42	1.46	5.6
Reticulon-1	RTN1	3.40	4.47	2.4
GTPase-activating protein and VPS9 domain-containing protein 1	GAPVD1	3.14	1.55	6.6
CD63 antigen	CD63	2.95	1.32	13.5
Cytochrome b5 type B	CYB5B	2.71	4.75	45.2
CD44 antigen	CD44	2.69	1.30	20.9
Amino acid transporter	SLC1A1	2.66	2.95	5.5
cDNA FLJ58568	C16orf58	2.54	3.34	9.5
PRA1 family protein	PRAF2	2.43	1.81	20.8
Coactosin-like protein	COTL1	2.36	1.59	21.9
Endonuclease domain-containing 1 protein	ENDOD1	2.27	2.55	14.2
Pirin (Iron-binding nuclear protein)	PIR	2.15	2.08	15.2
cDNA FLJ46477 fis	MCAM	2.11	1.99	15.1
UPF0729 protein C18orf32	C18orf32	2.02	3.12	13.2

**Table S3.** Proteins matching the criteria (p-value < 0.05, log2 fold-change < -2) of LFQ ABPP competition experiment with 25  $\mu$ M NCA (1 h) and 250 nM NC-4 (1 h) in HeLa (Volcano plot Figure S2C).

protein name	gene name	enrichment	p-value	sequence coverage [%]
Heme oxygenase 2	HMOX2	-5.62	5.40	46.8
NOC3-like protein	NOC3L	-4.29	2.15	5
Vesicle amine transport protein 1 homolog	VAT1	-3.30	2.71	48.9
Rho GTPase-activating protein 1	ARHGAP1	-3.11	1.56	27.6
Reticulon-1	RTN1	-2.92	3.38	2.4
Niemann-Pick C1 protein	NPC1	-2.89	2.02	5.6
V-type proton ATPase subunit	ATP6V0D1	-2.87	1.48	17.7
cDNA FLJ58568	C16orf58	-2.81	3.34	9.5
GTPase-activating protein and VPS9 domain-containing protein 1	GAPVD1	-2.74	1.58	6.6
Bone marrow stromal antigen 2	BST2	-2.69	3.75	18.3
Prostaglandin E synthase	hCG_30600	-2.66	1.60	5.6
cDNA FLJ77391	EHD4	-2.46	1.42	20.9
Solute carrier family 39 (Zinc transporter)	SLC39A10	-2.35	1.74	6.4
2-Hydroxyacylsphingosine 1-beta-galactosyltransferase	UGT8	-2.32	4.09	9.6
60S ribosomal protein L27	RPL27	-2.27	1.71	15.9
Carboxypeptidase	SCPEP1	-2.25	2.26	4.7
Acyl-CoA (8-3)-desaturase	FADS1	-2.22	1.30	13.5
Transmembrane protein 201	TMEM201	-2.19	2.86	3.8
Phosphoinositide phospholipase C	PLCD3	-2.18	1.70	8.9
Amino acid transporter	SLC1A1	-2.13	2.19	5.5
Isopentenyl-diphosphate Delta-isomerase 1	IDI1	-2.10	1.40	14.1
Prenylcysteine oxidase 1	PCYOX1	-2.10	1.94	20.6
Reticulon-4	RTN4	-2.09	2.14	15.9
Catechol O-methyltransferase	COMT	-2.06	1.55	15.8
Peptidyl-prolyl cis-trans isomerase	PPIL1	-2.05	1.68	29.5
Disco-interacting protein 2	DIP2B	-2.04	2.29	8.8
Carnitine O-palmitoyltransferase	CPT1A	-2.04	1.45	16.4

**Table S4.** Proteins matching the criteria (p-value < 0.05, log2 fold-change > 2) of LFQ ABPP experiment with 250 nM NC-4 in HeLa VAT-1 knockout cells (1h) (Volcano plot Figure 2E).

protein name	gene name	enrichment	p-value	sequence coverage [%]
Heme oxygenase 2	HMOX2	6.56	5.52	46.2
Bone marrow stromal antigen 2	BST2	6.27	5.24	18.3
CD63 antigen	CD63	4.40	3.29	13.5
Reticulon-3	RTN3	3.58	2.15	5.4
CD44 antigen	CD44	3.15	1.62	31.7
Cytochrome b5 type B	CYB5B	2.78	4.77	45.2
Serpin peptidase inhibitor cDNA FLJ56823	SERPINE2	2.72	1.33	8.7
Tubby-related protein 2	TULP2	2.36	2.19	9.4
Tubby-related protein 2	TULP2	2.23	1.60	12.6
Ankyrin repeat and KH domain- containing protein 1	ANKHD1	2.13	1.90	2.2
Dolichol-phosphate mannosyltransferase subunit 1	DPM1	2.10	1.47	8.5
Mitochondrial aldehyde dehydrogenase 2 variant	ALDH2	2.10	3.26	36.8
Reticulon-4	RTN4	2.06	2.49	14.3
MICOS complex subunit	APOOL	2.03	1.69	17.5

## 7.6 References

- [146] S. Nozoe, N. Ishii, G. Kusano, K. Kikuchi, T. Ohta, *Tetrahedron Letters* **1992**, *33*, 7547-7550.
- [147] M. Otsuka, K. Ichinose, I. Fujii, Y. Ebizuka, *Antimicrobial Agents and Chemotherapy* **2004**, *48*, 3468-3476.
- [148] a.) C. M. L. Gleissner, C. L. Pyka, W. Heydenreuter, T. F. Gronauer, C. Atzberger, V. S. Korotkov, W. Cheng, S. M. Hacker, A. M. Vollmar, S. Braig, S. A. Sieber, *ACS Central Science* **2019**, *5*, 1170-1178; b.) S.-Y. Kim, T. Mori, M. F. Chek, S. Furuya, K. Matsumoto, T. Yajima, T. Ogura, T. Hakoshima, *Scientific Reports* **2021**, *11*, 2120.
- [149] C. M. Gleissner, C. L. Pyka, W. Heydenreuter, T. F. Gronauer, C. Atzberger, V. S. Korotkov, W. Cheng, S. M. Hacker, A. M. Vollmar, S. Braig, S. A. Sieber, *ACS Cent Sci* **2019**, *5*, 1170-1178.
- [150] P. Mali, K. M. Esvelt, G. M. Church, *Nat Methods* **2013**, *10*, 957-963.
- [151] a.) X. B. Pan, J. C. Han, X. Cong, L. Wei, *Plos One* **2012**, *7*; b.) S. J. D. Neil, T. Zang, P. D. Bieniasz, *Nature* **2008**, *451*, 425-U421; c.) W. Liu, Y. Cao, Y. Guan, C. Zheng, *Biotechnol Lett* **2018**, *40*, 1015-1027; d.) D. Cai, J. Cao, Z. Li, X. Zheng, Y. Yao, W. Li, Z. Yuan, *BMC Cancer* **2009**, *9*, 102; e.) Y. Shigematsu, N. Oue, Y. Nishioka, N. Sakamoto, K. Sentani, Y. Sekino, S. Mukai, J. Teishima, A. Matsubara, W. Yasui, *Oncol Lett* **2017**, *14*, 999-1004; f.) K. H. Fang, H. K. Kao, L. M. Chi, Y. Liang, S. C. Liu, C. Hseuh, C. T. Liao, T. C. Yen, J. S. Yu, K. P. Chang, *Laryngoscope* **2014**, *124*, E354-E360.
- [152] G. Zhang, X. Li, Q. Chen, J. Li, Q. Ruan, Y. H. Chen, X. Yang, X. Wan, *Cancer Res* **2019**, *79*, 2220-2231.
- [153] a.) Y. Iwababu, H. Fujita, M. Kinomoto, K. Kaneko, Y. Ishizaka, Y. Tanaka, T. Sata, K. Tokunaga, *Journal of Biological Chemistry* **2009**, *284*, 35060-35072; b.) R. S. Mitchell, C. Katsura, M. A. Skasko, K. Fitzpatrick, D. Lau, A. Ruiz, E. B. Stephens, F. Margottin-Goguet, R. Benarous, J. C. Guatelli, *PLoS Pathog* **2009**, *5*, e1000450.
- [154] M. Z. Y. Choo, C. L. L. Chai, in *Annual Reports in Medicinal Chemistry, Vol. 61* (Ed.: K.-H. Altmann), Academic Press, **2023**, pp. 55-100.
- [155] a.) J. Cox, M. Mann, *Nat Biotechnol* **2008**, *26*, 1367-1372; b.) J. Cox, N. Neuhauser, A. Michalski, R. A. Scheltema, J. V. Olsen, M. Mann, *J Proteome Res* **2011**, *10*, 1794-1805.
- [156] J. Cox, M. Y. Hein, C. A. Lubber, I. Paron, N. Nagaraj, M. Mann, *Mol Cell Proteomics* **2014**, *13*, 2513-2526.
- [157] J. A. Vizcaino, E. W. Deutsch, R. Wang, A. Csordas, F. Reisinger, D. Rios, J. A. Dienes, Z. Sun, T. Farrah, N. Bandeira, P. A. Binz, I. Xenarios, M. Eisenacher, G. Mayer, L. Gatto, A. Campos, R. J. Chalkley, H. J. Kraus, J. P. Albar, S. Martinez-Bartolome, R. Apweiler, G. S. Omenn, L. Martens, A. R. Jones, H. Hermjakob, *Nature Biotechnology* **2014**, *32*, 223-226.
- [158] S. Tyanova, T. Temu, P. Sinitcyn, A. Carlson, M. Y. Hein, T. Geiger, M. Mann, J. Cox, *Nat Methods* **2016**, *13*, 731-740.

Neocarzilin inhibits cancer cell proliferation via BST-2 degradation resulting in lipid raft trapped EGFR.

## **Part III**

### Appendix

## 8 Abbreviations

ABPP	activity-based protein profiling
AfBPP	affinity-based protein profiling
AMR	antimicrobial resistance
CETSA	cellular thermal shift assay
cLogP	calculated 1-octanol–water partition coefficient
CRISPR	clustered regularly interspaced short palindromic repeats
DARTS	drug affinity responsive target stability
DIPG	diffuse intrinsic pontine glioma
FAAH	fatty acid amide hydrolase
EGFR	epidermal growth factor receptor
EPS	extracellular polymeric substance
Fsp <sup>3</sup>	fraction of sp <sup>3</sup> -hybridized carbon atoms
HGF	hepatocyte growth factor
LFQ	label-free quantification
MBIC	minimal biofilm inhibitory concentration
MIC	minimal inhibitory concentration
MS	mass-spectrometry
NCA	neocarzilin A
NCE	new chemical entity
PdNS	Pd nanosheets
PPI	protein-protein interaction
RISC	RNA-induced silencing complex
RNAi	RNA interference
SBDD	structure-based drug design
SIP	solvent-induced protein precipitation
SIPP	solvent-induced proteome profiling
siRNA	small interfering RNA
SPP	solvent proteome profiling
TMT	tandem mass tag
TPP	thermal protein profiling